QUANTIFYING AND REDUCING UNCERTAINTY IN METAL-BASED ADDITIVE MANUFACTURING LASER POWDER-BED FUSION PROCESSES

A Dissertation

by

GUSTAVO ANDRES TAPIA IMBAQUINGO

Submitted to the Office of Graduate and Professional Studies of
Texas A&M University
in partial fulfillment of the requirements for the degree of

DOCTOR OF PHILOSOPHY

Chair of Committee,	Alaa Elwany
Committee Members,	Raymundo Arroyave
	Satish Bukkapatnam
	Huiyan Sang
Head of Department,	Mark Lawley

May 2018

Major Subject: Industrial Engineering

ABSTRACT

Laser Powder-Bed Fusion processes capable of processing metallic materials are a set of relatively new and emerging Additive Manufacturing technologies that offer attractive potential and capabilities (e.g., design freedom, part consolidation and reduced material waste). Although they provide an exceptional advantage that cannot be matched by other traditional manufacturing processes, the path to widespread use of these new technologies still include some obstacles due to the limited understanding and intricate problems that the manufacturing process presents, such as low repeatability and low part quality compared to their conventional manufacturing counterparts.

This dissertation presents one of the first applications of different formal tools and frameworks from a combination of scientific fields including Uncertainty Quantification, Statistics, Probability and Data Science, into different problems within Additive Manufacturing Laser Powder-Bed Fusion processes. Specifically, modeling techniques such as Gaussian Processes and generalized Polynomial Chaos Expansions are employed to optimize porosity in printed parts, calibrate and validate different computer simulation models, and identify processing regions for satisfactory manufacturing. Proper analysis of these techniques is undertaken and its validation is successfully presented such that informed and knowledgeable perspectives about the manufacturing process are gained to better understand it. In turn, these new insights and understanding translate into improvement and advancement of Additive Manufacturing, and contribute towards its further growth and consolidation as a competitive and qualified technology within the manufacturing industry.

DEDICATION

To my parents, for everything they have done and still do for me.

ACKNOWLEDGMENTS

First and most importantly, I want to thank and express my sincere and infinite gratitude and appreciation to my Advisor Dr. Alaa Elwany for all his extraordinary mentorship, guidance, support, advice, encouragement, professionalism, and honesty (among many more qualities) that have been fundamental for the completion of this big step in my professional career as well as for my personal growth. Thanks for believing in me since the beginning.

Second, I want to thank my committee members: Dr. Raymundo Arroyave, Dr. Satish Bukkapatnam, and Dr. Huiyan Sang, as well as Dr. Ibrahim Karaman and Dr. Ji Ma, for their continued guidance, support, advice and suggestions that made possible reaching the objectives of this dissertation.

Similarly, I want to thank Dr. Wayne King, Dr. Manyalibo Matthews, Dr. Saad Khairallah, and the team at Lawrence Livermore National Laboratory for allowing me to work alongside one of the best and most important research teams in the field.

Thanks to all my excellent and intelligent colleagues, Mohamad Mahmoudi, Bing Zhang, Brian Franco, Kubra Karayagiz and Luke Johnson for always working extremely hard, while at the same time making work more enjoyable and motivating.

I want to also thank all my very good friends that I had the privilege to meet during this journey at Texas A&M. I would have not been able to achieve this without you all and the good moments that we had.

Finally, I want to thank my dad and mom, my two brothers, and my family and friends for their endless love, support and motivation to keep doing what I like.

CONTRIBUTORS AND FUNDING SOURCES

Contributors

This work was supervised by a dissertation committee consisting of committee chair, Professor Alaa Elwany of the Department of Industrial and Systems Engineering, and committee members, Professor Raymundo Arroyave of the Department of Materials Science and Engineering, Professor Satish Bukkapatnam of the Department of Industrial and Systems Engineering, and Professor Huiyan Sang of the Department of Statistics.

Section 4.3 of this dissertation was conducted in collaboration with Dr. Christapher Lang of NASA Langley Research Center.

Section 5.2 of this dissertation was conducted in collaboration with Dr. Wayne King, Dr. Manyalibo Matthews and Dr. Saad Khairallah at Lawrence Livermore National Laboratory.

Sections 5.3 and 5.4 of this dissertation were conducted in collaboration with Professor Ibrahim Karaman and Dr. Ji Ma of the Department of Materials Science and Engineering.

Section 5.4 of this dissertation was conducted in collaboration with Mohamad Mahmoudi of the Department of Industrial and Systems Engineering.

Portions of this dissertation were conducted with the advanced computing resources and consultation provided by Texas A&M High Performance Research Computing.

All other work conducted for the dissertation was completed by the student independently.

Funding Sources

Portions of this dissertation were supported by an Early Stage Innovations grant from NASA's Space Technology Research Grants Program, Grant No. NNX15AD71G.

Portions of this dissertation were supported by National Science Foundation through the NSF Research Traineeship (NRT) program under Grant No. NSF-DGE-1545403, "NRT-DESE: Data-Enabled Discovery and Design of Energy Materials (D3EM)".

Portions of this dissertation were supported by National Science Foundation through Grant

No. NSF-CMMI-1534534.

Portions of this dissertation were supported by National Science Foundation through Grant No. CNS-1343155.

Portions of this dissertation were performed under the auspices of the U.S. Department of Energy by Lawrence Livermore National Laboratory under contract DE-AC52-07NA27344.

Portions of this dissertation were supported through a Laboratory Directed Research and Development (LDRD) grant, Grant No. 15-ERD-037.

The contents of this dissertation are solely the responsibility of the authors and do not necessarily represent the official views of Texas A&M University, National Aeronautics and Space Administration (NASA), National Science Foundation (NSF), Lawrence Livermore National Laboratory (LLNL), or U.S. Department of Energy.

NOMENCLATURE

AM	Additive Manufacturing
BLUP	Best Linear Unbiased Predictor, otherwise known as Kriging
$\mathrm{cov}\left[\cdot,\cdot\right]$	Covariance operator
CV	Cross Validation
$D4$	Laser Beam Size
dof	Degrees of Freedom
ET	Eagar-Tsai model
$\mathbb{E}\left[\cdot\right]$	Expectation operator
FEM	Finite Element Method
FOV	Field of View
$\Gamma\left(\cdot\right)$	Gamma function
gPCE	Generalized Polynomial Chaos Expansions
GP	Gaussian Process
GSA	Global Sensitivity Analysis
h_d	Hatch Distance
ICME	Integrated Computational Materials Engineering
i.i.d.	Independent and Identically Distributed
$\mathcal{K}_\nu\left(\cdot\right)$	Modified Bessel function of second kind of order ν

LHS	Latin Hypercube Sampling
LLNL	Lawrence Livermore National Laboratory
LOO	Leave-One-Out Cross Validation
L-PBF	Laser Powder-Bed Fusion
MAPE	Mean Absolute Predictive Error
MC	Monte Carlo
MCMC	Markov Chain Monte Carlo
$\mathcal{M}$	Model, in a general sense
MSPE	Mean Squared Predictive Error
NiTi	Nickel-Titanium alloy
pdf	Probability Distribution Function
P	Laser Power
QoI	Quantity of Interest
SEM	Scanning Electron Microscopy
SMA	Shape-Memory alloy
t_d	Layer Thickness
UP	Uncertainty Propagation
UQ	Uncertainty Quantification
v	Scanning Speed
$\mathbf{x}$	Input vector to the process

Y, $\mathbf{Y}$	Output(s) or QoI(s) of the process

TABLE OF CONTENTS

Page

LIST OF FIGURES

FIGURE Page

LIST OF TABLES

TABLE Page

1. INTRODUCTION

1.1 Additive Manufacturing

Additive Manufacturing (AM) is a relative new field in the manufacturing industry that has increasingly gained attention (especially over the last decade) by researchers, industrial stakeholders, practitioners, public media and even national governments due to the complete paradigm change it brings to the manufacturing industry. The ISO/TC261-ASTM/F42 joint group defines AM as the

> "*process of joining materials to make objects from 3D model data, usually layer upon layer, as opposed to subtractive manufacturing technologies*" [1].

First applications for AM were limited to creation of visualization models and prototypes in order to accelerate the design and production cycle of components, hence the alias Rapid Prototyping or 3D Printing. Nowadays, there exists a number of AM processes implemented with different manufacturing principles and technologies, which have been identified and standardized into seven broad categories. Four of these categories are capable of producing metallic parts: Powder-Bed Fusion (PBF), Binder Jetting, Sheet Lamination and Directed Energy Deposition (DED) [1, 2].

Specifically, AM technologies capable of processing advanced metallic materials and alloys have been developed since the early 1990s, experienced a tremendous and exponential grow during the 2000s, and have now become important manufacturing processes for end parts in several industrial sectors such as toolmaking, dental, medical, automotive and aerospace [3].

There are many advantages that have driven attention and widespread adoption of AM processes over traditional manufacturing (such as casting, machining, forming, etc.), with the following list being a subset of some of the most important [4]:

- Production of arbitrarily complex geometries (e.g., interconnected cooling channels, lattices or honeycomb structures). Figure 1.1a shows a Titanium heat exchanger with internal cooling channels for enhanced fluid flow and heat transfer performance in aviation applications.

The complicated internal features that this part presents cannot be built through any other manufacturing process.

- Part consolidation, which translates to the ability of manufacturing one single complete part as opposed to producing many several smaller parts which are to be joined together (either by fastening, glue or welding). Figure 1.1b shows a GE LEAP jet engine fuel nozzle which originally consisted of 20 different components that needed to be assembled together. This same component is now being produced into a one single complete part through AM techniques and is being successfully used in commercial airliners [5].

- Reduction in part weight and material waste through design and topology optimization. Figure 1.1c shows different redesign phases (left to right) of a GE aircraft engine bracket developed by Frustum Inc. and 3D Systems Inc. that reduced 70% of the bracket weight initially manufactured via classic technologies while still meeting all functional and structural requirements [6, 7].

- Production of parts without needs for expensive part-specific tooling. Figure 1.1d shows a knee implant built through AM to fit the particular size and specification for a patient. If a second patient requires a similar implant, a change on the computer model for the part needs only to be performed, as opposed to having to create or purchase new sets of tools or casts to produce it with traditional manufacturing processes.

1.2 Laser Powder-Bed Fusion Processes

In this dissertation, the focus will be placed specifically in the *Laser Powder-Bed Fusion* (L-PBF) process, due to their broad range of applications, large selection of materials it can handle (e.g., steels, titanium-based alloys, aluminum-based alloys and nickel-based alloys, among several others), spatial resolution, dimensional accuracy and surface finish [10]. This technology is oftentimes referred as Selective Laser Melting (SLM), Selective Laser Sintering (SLS), Direct Metal Production (DMP), or Direct Metal Laser Sintering (DMLS). It is worth to note that a similar PBF

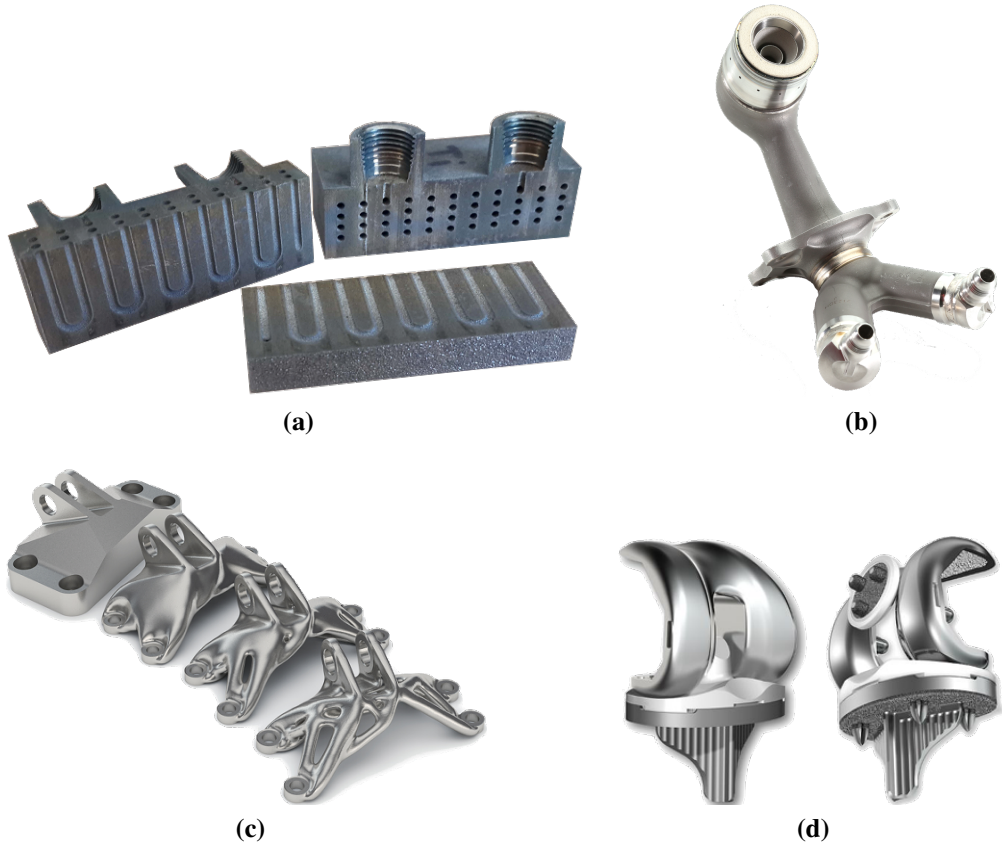

Figure 1.1: Advantages of Additive Manufacturing over traditional processes. **(a)** Complex geometries. **(b)** Part consolidation. Reprinted from [5]. **(c)** Reduced material waste. Reprinted from [8]. **(d)** No need for part-specific tooling. Reprinted from [9].

process also exists called Electron Beam PBF (EB-PBF) or Electron Beam Melting (EBM), with the main difference being the use of an electron beam as the source of energy as opposed to a laser beam.

L-PBF processes employ a high-energy laser beam to selectively fuse fine metallic powder particles in a layer-by-layer fashion [11]. The process starts by placing a thin layer of powder particles (usually ranging between $20\,\mu\mathrm{m}$ to $100\,\mu\mathrm{m}$) on top of a vertical piston denominated *fabrication piston*. Powder is laid using a recoating roller, scraper or blade that moves the particles from the powder delivery system to the fabrication piston. The high-energy laser is then fired through a scanning system generally consisting of a set of motorized mirrors which reflect the beam onto the

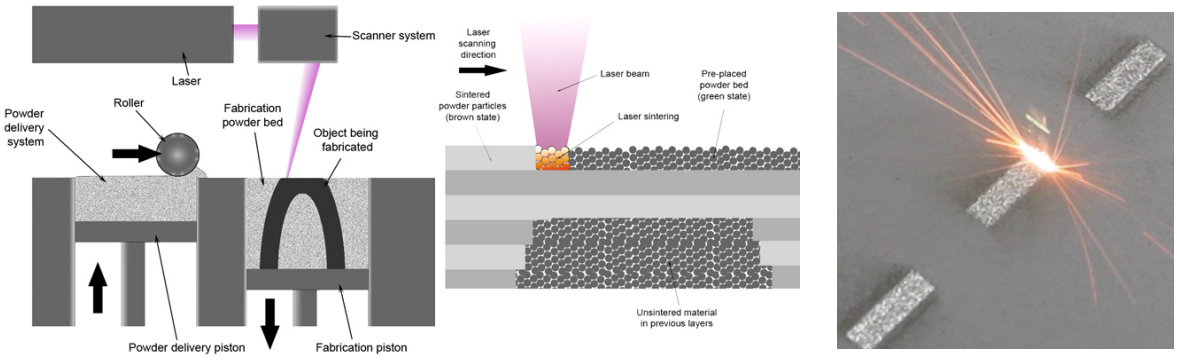

(a) **(b)**

Figure 1.2: Laser Powder-Bed Fusion process. **(a)** Schematic diagram of the L-PBF process. Reprinted from [12]. **(b)** Laser being scanned on steel powder in a L-PBF system. Reprinted from [13].

powder layer until the complete cross-section of the part has been scanned. Next, the fabrication piston is moved down a length equivalent to one-layer thickness, and these steps are repeated again and iterated until the part has been completely produced. A schematic diagram of a L-PBF system and its components is presented in Figure 1.2a, and a real photograph from a L-PBF system is shown in Figure 1.2b.

Even though the manufacturing mechanism in L-PBF is simple, it is also the root cause of many technical challenges that impact negatively its advancement and adoption as a mainstream industrial manufacturing process. In particular, the challenge lies in the several complex physical phenomena involved during the manufacturing process. These include rapid melting, evaporation, solidification, recoil, and re-heating upon successive passes of the laser beam within the same layer or across successive layers. The combination of all of these makes the end part susceptible to defects like porosity, residual stress, and micro-cracks due to the extremely high thermal gradients and cooling rates. In a quantitatively context, cooling rates for casting range between $10\ ^{\circ}\mathrm{C}/\mathrm{s}$ to $10^{2}\ ^{\circ}\mathrm{C}/\mathrm{s}$ [14], while in L-PBF they have been identified to magnitudes larger than to $10^{5}\ ^{\circ}\mathrm{C}/\mathrm{s}$ [15].

These mentioned defects distress the mechanical properties of the end parts making them unsuitable for several applications. Additionally, they become major barriers towards the improvement of the current state of L-PBF since they amplify issues like low part quality and limited re-

peatability, which along with the lack of material and process standardization, impede the L-PBF technology to meet the stringent requirements for industrial sectors such as aerospace, automotive or medical [3].

Many recently published research roadmaps agree that there exists the need for developing modeling and simulation tools to foster our understanding of the process and ultimately serve as predictive tools to improve and optimize the process while mitigating potential defects [16, 17]. An emerging field that branched out of computational materials science and aims towards solving the mentioned modeling problem is *Integrated Computational Materials Engineering* (ICME). This field is a new approach that aims to integrate computational materials models to enable the optimization of the materials, manufacturing processes, and component design long before components are fabricated [18]. Additionally, ICME has been able to evolve in the last two decades as a relevant field within materials science and engineering due to the great advances in modern high-performance computational resources (i.e., both hardware and software development).

Several research efforts in L-PBF have been directed towards the development of computer modeling and simulation tools following an ICME approach. These computer models involve the solution of many complex mathematical equations derived from the physics and theories of the process under investigation. Therefore, it is not uncommon that convergence to a solution would usually take from several hours to the range of days (or even weeks), even in the presence of state-of-the-art high-performance computational resources and facilities. Although these models are still invaluable for understanding the physics of the process, their direct use in process optimization is impractical and sometimes unfeasible [19]. Hence, the key challenge in using L-PBF computer simulation models is to overcome the computational burden associated with running the simulations.

An alternate approach to circumvent the barriers that hamper adoption of L-PBF is by experimental practices. In this sense, many research institutions and industrial companies invest in high-technology and modern equipment and facilities to carry out experiments, tests, and examinations in order to improve the understanding of the L-PBF process (e.g., by characterizing the

mechanical behavior or microstructure of end parts). This experimental option is also challenging given that fact that the manufacturing process involves up to 30 processing parameters, with each of them influencing (directly or indirectly) the quality and performance attained by the end parts [20, 21]. Nevertheless, the most relevant L-PBF processing parameters have been identified to be:

- Laser power (P): relates to the amount of energy delivered by the laser beam.
- Scanning speed (v): relates to the duration of time that the laser beam dwells over a specific region on the powder bed.
- Laser beam size ($D4$): relates to the area where the energy from the laser source is transferred to. Throughout this dissertation, it is assumed that the laser beam has a Gaussian profile and this value is taken as 4 times its standard deviation [22].
- Hatch distance (h_d): distance between two consecutive laser scans.
- Layer thickness (t_d): thickness of the powder bed.

The majority of existing experimental efforts rely on extensive trial-and-error or round-robin testing for selecting parameter combinations that optimize some quality or property in the printed parts. However, the big drawback with this approach is that it incurs in high costs associated with experiments and testing needed to achieve the desired results.

Several researchers have understood this issue and taken better approaches such as systematic and statistical Design of Experiments to experimentally study the L-PBF process resulting in an improvement in both the amount of experiments needed to collect and the insights learned. Nevertheless, there is still a gap in which both research approaches of the L-PBF process – computationally expensive simulations and costly experimental observations – can be efficiently used to improve the understanding and optimize the process. This gap can be filled by formal application of another emerging scientific field named *Uncertainty Quantification* (UQ).

1.3 Uncertainty Quantification

There are several definitions for the word *uncertainty*, which typically depends on the context where it is being described. A definition by Grebici et al. [23] in a general scientific context refers to "the lack of [or presence of ambiguous] knowledge that may introduce risks to the outcome and execution of a process" [23].

Since the origins of mankind, the desire to understand the uncertain has always been a central part of the human brain. It closely relates to inquisitive thinking such as exploration, investigation and learning, and has been a fundamental factor to the progress of humanity [24]. Over the past two centuries, mathematicians, statisticians and scientists (notably physicists and chemists) directly and indirectly formulated many concepts and theories that involved the analysis and quantification of uncertainty in the different processes under their study (one of the most popular cases being when in 1809 Carl Friedrich Gauss calculated the orbits of celestial bodies with what now is known as the Least Squares method [25]). All these concepts have been generalized into more disciplines and applications over time and, with the wake on computational technologies and the ever-increasing complexity in systems[1] of the modern world, have given birth to UQ.

The scientific field of UQ combines theory and knowledge from applied mathematics, classical statistics, probability, computer science and machine learning, in order to characterize and reduce uncertainties in applications for computational or real processes [26]. Applications of UQ span over a wide range across several science, engineering, and social disciplines such as climate and weather [27], nuclear engineering [28], computational fluid dynamics [29], medicine [30], and econometrics [31].

Within the engineering domain, there is a growing need of predictive modeling and tools that can help in the many fronts of engineering applications in industry, some of these being for instance, part design for specified lifetimes, reliability assessments or safety factors. However, as explained in the previous section, the classic approach requires reliance on validation experiments which are subject to high costs and long times, especially for complex engineering systems with

[1] The word *systems* here refers to any context, e.g., engineering, social, biological, etc.

tough operating conditions [32].

UQ is an attractive framework for the posed engineering problem mentioned above since its methodologies are based on statistical and probabilistic predictive models that can be applied on those instances when there is some to little available data. Therefore, UQ suits perfectly to L-PBF research problems, given that it provides the tools and methodologies which can be integrated to both fronts of L-PBF research (modeling and experimental) to characterize the sources and magnitudes of uncertainty that affect the different physical phenomena undergoing during manufacturing. For these reasons, UQ can be used as an alternative to reduce (or remove) the high burden associated with computationally expensive simulation models or costly experimental observations. Additionally, it is worth noting that computational materials science and ICME are fields in which the application of UQ is highly desired [33, 34].

Research and investigation of UQ techniques have been employed in traditional manufacturing applications throughout the years. Nonetheless, the literature of UQ research applied to AM, and specifically to L-PBF, is quite small and limited, although it has been slowly increasing over the years [35]. This dissertation presents several statistical UQ methodologies as well as their implementation into different L-PBF applications that aim to:

- Improve the capabilities and state of knowledge of the process.
- Refine quality and performance of L-PBF end parts.
- Enhance the understanding of the phenomena that happens during manufacturing.

This is achieved by means of both: experimental work by characterization of several physical processes and mechanisms within L-PBF, and computational work by utilization of different simulation models that recreate several physical phenomena that are present during the L-PBF manufacturing process. Specifically, this dissertation will bridge the gaps in the L-PBF literature and fulfill the objectives listed in the next sections.

1.4 Research Gaps

There is a consensus within the manufacturing community, that L-PBF processes are still not able to produce parts comparable to their counterparts manufactured through traditional processes, in terms of quality and performance. This is attributed to the lack of understanding of the many issues that take place during the L-PBF build process. Even though extensive investigation and research has been directed towards the development of the knowledge and understanding of the manufacturing process (specifically in the form of computational simulation models and a diversity of substantial laboratory experiments), two gaps currently exist in the L-PBF literature:

1. Only a countable number of works (including this dissertation) have applied formal UQ tools and practices in metal L-PBF processes and the majority of the works in the literature relied on brute force experimental methods.

2. No studies were conducted to take this a step further and leverage the outcomes and insight gained from these UQ methodologies towards understanding fundamental aspects of the process and improving it (e.g., identifying sources of uncertainty across different phases of the L-PBF process chain, and suggesting actions to mitigate them).

1.5 Dissertation Objectives

The main broad objective of this dissertation is to

apply formal tools of UQ to quantify and reduce uncertainties in the L-PBF process.

Both Sections 1.1 and 1.2 presented and established the context for how L-PBF AM processes are a relative new set of technologies with attractive features that can't be compared with traditional methods, as well as the problems that they face towards widespread adoption in different sectors of industry with stringent requirements (i.e., lower quality, repeatability and performance). Similarly, Section 1.3 introduced a general overview of UQ, along with the need for its adoption into L-PBF practices and the potential benefits that UQ methodologies can bring for AM.

Therefore, the application of formal UQ methodologies to the study of different physical processes that occur during the manufacturing of L-PBF parts is deemed of paramount importance. Specifically, the aim is to identify the different sources of uncertainty that affect L-PBF processes, characterize this uncertainty, and attempt to reduce it based on the insights and knowledge gained after proper interpretation of results from the applied methodologies.

1.6 Organization of the Dissertation

The dissertation is organized in the following structure: Chapter 2 highlights the state-of-the-art for both L-PBF technologies and UQ methodologies and applications. It surveys the relevant literature in the field, as well as related literature coming from other fields of research that contribute with knowledge and comprehension compatible to the different problems solved within this dissertation.

Next in Chapter 3, different UQ tools and methodologies are introduced for the reader to familiarize with the approaches and notations used throughout the dissertation. For each methodology, its mathematical and theoretical foundations are presented as well as its potential applicability into different problems.

Chapters 4 and 5 include the bulk content of the dissertation. These two chapters present the application of the introduced UQ methodologies to different aspects, problems, and processes within the L-PBF technology. The content of these chapters forms the bridge that fills in the gaps and accomplishes the objectives defined in Sections 1.4 and 1.5.

The dissertation is finalized in Chapter 6 where implications, concluding remarks and potential future extensions are outlined.

2. STATE OF THE ART*

As introduced in Chapter 1, the present dissertation embraces the application of different formal UQ methodologies into several problems within L-PBF processes. This chapter provides a brief overview of many approaches and problems that the research community has identified as important and has invested resources and time to solve.

We divide the chapter in two main sections, starting out with a summary of solutions for different problems in L-PBF technologies in Section 2.1. Here, several aspects and factors in L-PBF that contribute to the possible presence of defects and problems are considered, as well as the proposed solutions from the community. Next, Section 2.2 introduces the different types of uncertainty along with a categorization of UQ problems which will be constantly used throughout the dissertation.

2.1 State of the Art of Research in Laser Powder-Bed Fusion processes

Most of AM technologies initial development date back to the late 1980s, however it was not until the late 1990s and the starting of the 21st century when AM research skyrocketed. The main reasons for this surge in investigation and studies are the attractive, advanced and different features that AM provides as alternative to old-fashioned traditional manufacturing processes, as well as the expiration of several of the initial patents involving the technologies [4, 11]. L-PBF was no exception to this breakthrough with innumerable academic and industrial researchers taking on the quest to improve and refine the technology.

Many works focus towards improvement of L-PBF technologies at different stages of the process where the common objective is to control and reduce the defects within end parts. Additionally, most authors coincide on the high influence of some processing parameters to mechanical properties and performance of end parts. As mentioned in Section 1.2, laser power, scanning speed, laser beam size, hatch distance, and layer thickness have been flagged as the most influen-

*Parts of this section have been reprinted with permission from G. Tapia and A. Elwany, "A review on process monitoring and control in metal-based additive manufacturing," *Journal of Manufacturing Science and Engineering*, vol. 136, no. 6, p. 060801, 2014. Copyright © 2014 by ASME.

tial parameters in the process, and thus are the most researched processing parameters. This set of parameters are identified as *laser parameters* since they relate to the characteristics at which energy is transferred from the laser beam source onto the raw material. Nevertheless, there are several other parameters which still affect the end results of the process, but in general do not contribute as drastically as the laser parameters. These include [20, 21]:

- Scanning strategies or trajectories that the laser follows.
- Layering of powder, in terms of mechanical systems (e.g., use of blades, rollers, scrapers, etc.).
- Atmospheric control of the manufacturing chamber (e.g., O_2 level or choice of inert gas)
- Powder-bed temperature.
- Raw powder properties (e.g., particle size, morphology, atomization process, etc.).

A poor choice of these various processing parameters might result on the presence of several defects. Before introducing the common defects in L-PBF, a term worthwhile introducing is the *melt pool*. The melt pool is the region at the laser-powder interface at which metallic powder particles fuse to form a pool of molten metal then solidify after the laser beam moves to another location [19]. The depth of the melt pool has been of much interest in several prior studies since it gives an indication of how well successive layers bond to one another, as well as a way to prevent keyhole mode [36]. As a side note, keyhole melting is undesirable in L-PBF since it involves evaporation of the material and results in deeper melt pool depths and trails of voids.

2.1.1 Manufacturing Defects

As described in Section 1.2, the L-PBF process is a thermal manufacturing process which relies on the transport and delivery of heat from the laser source to the material in order to melt particles together and create a solid bond. Because of the complexities that this process involves, parts are highly prone to several defects that condition and constrain their performance. These defects will be categorized as four different types: porosity, balling, cracks, and lack of fusion.

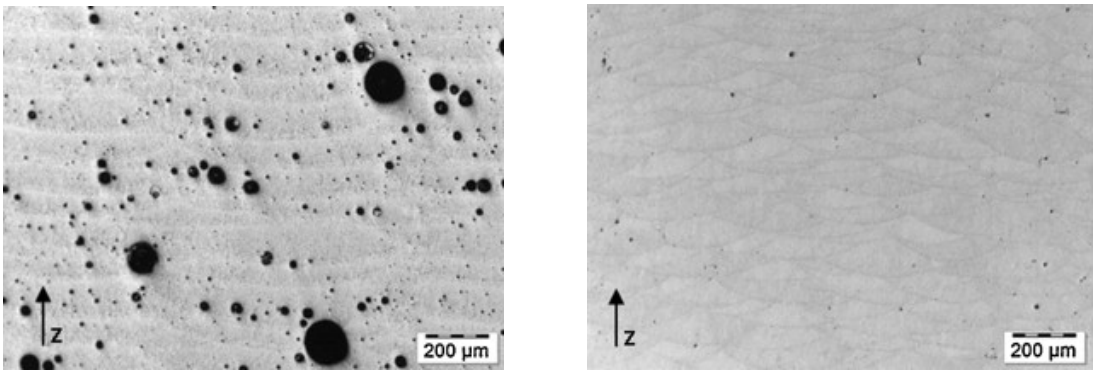

(a) **(b)**

Figure 2.1: Porosity within L-PBF printed samples based on variation of processing parameters. **(a)** High porosity sample. Reprinted with permission from [39]. **(b)** Low porosity sample. Reprinted with permission from [39].

2.1.1.1 Porosity

Porosity is one of the most common defects found in L-PBF and involves the formation of pores within the structure of the part. Several reasons can trigger the formation of pores, and this is the reason why it is a common problem in L-PBF [37]. Pores can be caused by the combination of localized melting, high cooling rates and gas entrapment. This occurs when there exists gas present within the powder bed which is not able to exit the melt pool before the material solidifies [38].

The introduction of gas in the melt pool can be attributed to the following factors:

- A low packing density of the material particles on the powder bed [38].
- During the processing of bulk material into powder by gas atomization since this process involves interaction of fine material particles inside an inert gas atmosphere [40].
- The highly localized temperatures happening inside the melt pool, which can induce evaporation of alloy constituents with relative lower melting point [41].

Pores can also be formed by a poor laser-powder interaction which sometimes can be traced back to inappropriate choices of laser parameters. There has been extensive research on optimization and identification of process parameters that would yield fully dense parts [41–44]. Figure 2.1

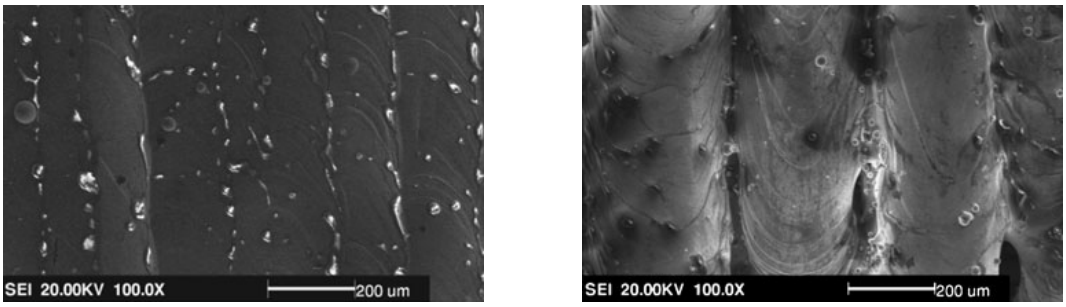

(a) **(b)**

Figure 2.2: Balling in L-PBF printed samples based on variation of processing parameters. **(a)** Balling at lower hatch distance. Reprinted with permission from [45]. **(b)** Balling at larger hatch distance. Reprinted with permission from [45].

present two micrographs of L-PBF samples presenting different grades of porosity printed with different sets of process parameters. This figure ratifies and highlights the importance of proper selection of process parameters on the overall presence of pores as well as on pore sizes.

2.1.1.2 Balling

Balling is another defect that is highly detrimental to L-PBF parts and has been commonly studied as well [45–48]. Balling is most likely to form right after the laser beam has passed a specific region of material particles and these particles are undergoing rapid solidification. Particularly, if the solidified material does not produce a flat layer but instead creates large spherical- or ellipsoidal- shaped particles on the surface, then all these irregularities on the surface are denominated balling defects [45, 47]. This defect relates to combination of high cooling rates, shrinkage, and surface tension acting together within the recently lasered material and deteriorates surface roughness. Additionally, balling can be harmful to the L-PBF system since it causes high friction between the surface of the printed layers and the mechanical layering system that can result on uneven powder layers, increase the need of post processing due to rough surfaces, or even stop the manufacturing system due to high friction.

Similarly to porosity, this defect also depends on proper selection of processing parameters as shown in Figure 2.2.

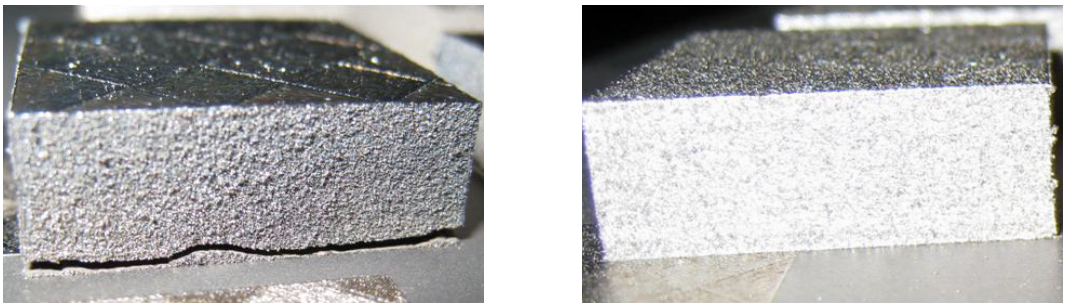

(a) **(b)**

Figure 2.3: Crack formation in L-PBF printed samples based on differences in pre-heating. **(a)** Crack presence due to no pre-heating. Reprinted with permission from [51]. **(b)** No external cracks present in the sample after pre-heating. Reprinted with permission from [51].

2.1.1.3 Cracks

Large residual thermal stresses are highly likely to develop in the solidified material given the elevated localized temperatures that take place in and around the melt pool. These residual thermal stresses in combination with large thermal spatial gradients provide a favorable situation for crack initiators, which will tend to keep growing until all residual stresses are relieved [49].

The most used approach that can be taken to reduce the probability of crack initiation and presence of high residual thermal gradients is to pre-heat both the substrate plates and the powder and to control the ambient temperature of the manufacturing system [38]. Figure 2.3 shows a printed part resulting after pre-heating. A second technique that can diminish the presence of cracks, while reducing the porosity of the parts, is called *Hot Isostatic Pressing* (HIP) [49]. This approach subjects the printed part to elevated temperatures and isostatic gas pressures in order to collapse internal pores and micro-cracks by elastic and plastic deformation and diffusion bonding [50].

2.1.1.4 Lack of Fusion

This defect in L-PBF processes refers to those instances when the laser beam does not provide enough energy for the powder particles to fully melt, and bond to neighboring particles and to previous layers. According to Zhang et al. [38], there exists two types of Lack-of-Fusion defects:

1. Poor bonding defects due to insufficient molten metal during a solidification process.

2. Defects with unmelted metal powders.

Once this defect starts to take place, it gradually propagates as new layers are printed and prevent layer-wise bonding since it is difficult to fully melt unmelted particles from previous layers [38, 52].

In general, all these defects are related to each other, and one can be the root cause for others during manufacturing. Therefore, many research efforts have focused on understanding, optimizing and reducing defect presence in L-PBF parts. Next, several approaches taken by the community like sensing and monitoring, computational modeling, and experimental efforts are presented.

2.1.2 Sensing and Monitoring

A vast majority of research on process monitoring and control in metal-based AM focuses on temperature monitoring because the temperature field is an excellent proxy for part quality, since it has a direct impact on the resulting microstructure, density, and mechanical properties of the part. Effective monitoring and control to ensure a homogenous temperature field significantly aids in improving part quality and reducing the probability of defect presence.

Sensor and monitoring technology for temperature measurement has greatly benefited thanks to the advancements in the semiconductor industry within the last 50 years. These types of sensors have facilitated and continue to facilitate collection of temperature data in L-PBF processes (as well as many more manufacturing and engineering applications). The typical devices used for monitoring by the L-PBF community are the following:

- *Pyrometry*: Defined as the non-contact measurement of temperature of a body based upon its emitted thermal radiation. Pyrometer sensors typically can come as photodiodes (devices used to detect radiation and convert it into an electrical signal) or digital cameras (large array of photodiodes, called pixels, each of which detects light and converts it into an image after appropriate signal processing). One of the key advantages in using pyrometry for temperature monitoring is the capability to measure and collect temperature data without the need

for physical contact with the thermal body. This provides much freedom in monitoring hard-to-access surfaces and features regardless of their location or orientation. The contact-free monitoring also serves to minimize potential damage and degradation of the sensor. Similarly, a second advantage is the capability of detecting radiation emitted by moving objects within the focus boundaries. Both of the mentioned features make pyrometry particularly attractive for applications involving fast moving lasers such as the L-PBF process.

- *Thermocouples*: It is a device that conducts contact measurement of temperature. Thermocouples belong to the class of thermoelectric thermometers [53] and consist of two dissimilar wires connected together at one end with a voltage measurement device connected across the free ends [54]. Thermocouples represent a considerably less inexpensive alternative to pyrometers for monitoring similar temperature ranges. These devices are self-powered and do not require an external power source. They are typically in the form of small-diameter wires (up to $80\,\mu\mathrm{m}$-diameter) making them relevant for limited space applications.

A number of researchers have employed these sensing technologies and built monitoring setups to control the L-PBF process. Berumen et al. [55] use a digital camera to monitor the powder coating step for each layer and develop algorithms to detect problems such as low or excessive powder feed and coater problems. Kleszczynski et al. [56] present a system for error detection using a high-resolution camera mounted outside the build chamber. With the aid of subsequent image processing, the system is able to detect errors in process stability (e.g., insufficient powder, poor supports, or coater damage) and part quality. Kruth et al. [57, 58] design and patent a feedback control system to stabilize the temperature distribution in the melt pool using both a digital camera and a photodiode coaxially to the laser beam. They perform experiments on parts with complex features such as overhangs and test different combinations of scanning patterns.

Experimental setups based on a coaxial camera were also reported in several studies. Lott et al. [59] mount a pyrometer camera with an additional illumination source to measure temperature coaxially with the laser beam. The main advantage of this setup is that the images captured by the camera followed the path of the laser. The authors then implement image-processing algorithms to

test the system and demonstrate its ability to monitor the melt pool. Chivel and Smurov [60, 61, 62] use a setup to monitor the maximum surface temperature, spatial temperature distribution in the processing area, and the size of the melt pool, then use this information to control the evolution of these temperatures. The setup consisted of a camera and a two-channel pyrometer, whereby the former measures temperature distribution at the lasering zone, and the latter measures the maximum surface temperature in the irradiation spot.

It is clear to see that several resources have been pointed towards the monitoring of the process by means of temperature sensors. Nevertheless, this has not been the only approach taken by researchers to improve the understanding of the L-PBF process, and computational modeling techniques will be presented next.

2.1.3 Computational Modeling

Computational modeling and simulation are core components in modern research techniques in any (if not all) fields of science. Computational modeling is a physical, mathematical, or otherwise logical representation of a system, entity, phenomenon, or process through computer programs and codes intended to enhance the ability to understand, predict, or control its behavior [63]. This area of research has become particularly important due to the great advancements on computational technology like high-performance hardware and software able to handle intricate complex tasks and calculations. The L-PBF community is no exception and has also taken initiative and adjusted their research paths to include computer models that describe the manufacturing process.

Specifically, numerical-based computer modeling and simulation methods are useful to better understand the thermal histories that the material undergoes during L-PBF manufacturing. Many groups have relied on *Finite Element Method* (FEM) since it is a versatile and accurate numerical approach for solving different engineering problems (e.g., heat transfer, solid mechanics, fluid dynamics), regardless of geometry or domain complexity [64]. The vast majority of the literature in FEM modeling for L-PBF processes have focused on investigating thermal history, thermal distributions and melt pool geometry on single-track experiments (see [65–68]) and on multi-track situations (see [69, 70]). These computer models are often referred as *continuum-scale* approaches

due to the fact that they assume a continuum block of matter with effective thermo-physical properties as the layer of powder particles.

A counter-approach is known as *powder-scale* L-PBF computer models which directly accounts for more realistic approximations and physics of the process such as geometry, size and distribution of the particles inside the powder bed. Additionally, these models normally account for events such as evaporation, Marangoni convection, fluid flow, volume shrinkage, spatter and particle ejection, etc. Nonetheless, this approach is generally more computationally expensive (even in the presence of state-of-the-art computing resources) that turn it infeasible to use for full-part simulations or processing parameter optimizations. Some cases that illustrate this approach are presented in [71–76] while a comprehensive review by King et al. [77] describes some of these modeling applications.

Regardless of the type of approach taken, L-PBF computer models are in general well received in the ICME community since they enable understanding of fundamentals within the manufacturing process. However, they are also costly in terms of computational resources with long run times (spanning from hours to weeks), and hence, it results prohibitive to carry on studies based solely on these models, especially when the problem is to optimize certain qualities of the process that would involve a large number of simulations. Moreover, since these computer models represent approximations to real physical processes, they need to be validated to real experimental data. This task is sometimes difficult to achieve in L-PBF due to the complexity it involves: micro-localized heating, high temperatures above boiling points, high cooling rates, high thermal gradients, etc. Therefore, application of statistical and probabilistic frameworks through UQ is desired.

As a final approach to the L-PBF research, some experimental techniques implemented within the community are presented.

2.1.4 Experimental Approaches

In this section, some of the experimental research approaches for L-PBF will be presented. These include those aiming toward optimization of the process by identification and selection of optimal process parameters and microstructure characterization of printed parts in order to identify

different defects and track down their causes.

In the study presented by Thijs et al. [78], the authors investigate the presence of martensitic phases in Ti-6Al-4V and relates the directions of grains to the process parameters. Additionally, they characterize the presence of pores due to gas entrapment and lack of fusion. A similar approach was followed by Mumtaz et al. [79] to characterize the pore defects within the microstructure of printed parts by experimental optimization of processing parameters. Li et al. [45] studies balling behavior in stainless steel and nickel alloys by analyzing Scanning Electron Microscopy (SEM) images of different samples, starting from raw powder morphologies, single-track experiments, cross hatches and full parts. They identify the layering phase and remelting of previous layers as mechanisms under which balling is likely to happen. Similar approaches have been investigated by [47, 80]. Investigations of residual stress, thermal deformation and cracking has also taken place (see [81–83]), where mechanical properties of printed samples are characterized based on different scanning strategies. A comprehensive work detailing generation and propagation mechanisms of defects in L-PBF by [84] is referred to the interested reader.

There also exist statistical methodologies implemented to L-PBF processes which have concentrated on Design of Experiments approaches through full- or fractional-factorial designs to identify processing parameters influential to specific properties or defects of the parts [85–87], and on an innovative approach to analyze variability of properties in printed parts by identifying key microstructural characteristics in Shape-Memory alloys (SMA) [88]. Another interesting approach is presented by Aboutaleb et al. [89] where determination of optimal manufacturing parameter settings is performed by leveraging and using data and knowledge from prior studies. Different research approaches towards better understanding of L-PBF processes have also been investigated which includes applications into functional design and control of properties in printed parts by localized variation of processing parameters during manufacturing with SMAs [90].

It is clear that a vast amount of research has been devoted towards L-PBF, demonstrated by the enormous advancement of the technology up to the point that is now regarded as an industrial manufacturing option. However, there is still many gaps, missing knowledge and drawbacks about

the process that need to be addressed in order to for the technology to be a challenging rival for classic manufacturing processes.

2.2 State of the Art of Research in Uncertainty Quantification

UQ is a field of increasing practical importance at the intersection of applied mathematics, statistics, computation and numerous application areas in science and engineering. It deals with the identification, characterization, quantification and reduction of uncertainties of a system (which can take form of a computational model or real physical process) [91]. A familiar categorization of uncertainty divides it into two categories [33]:

- *Aleatoric* uncertainty: This type of uncertainty arises from inherent randomness of the system under study and can be described by a probability distribution. Characterization of this distribution is helped by observation of data, but its variance (and hence its uncertainty) cannot be reduced.

- *Epistemic* uncertainty: This type of uncertainty derives from limited knowledge and information of the system and thus cannot be described by a probability distribution. However, additional observation of data can help reduce this uncertainty.

Through UQ methodologies, certainty about different *Quantities of Interest* (QoIs) of a system can be determined even under the presence of not fully known features (i.e., on the presence of limited data). This attribute, in addition to the advances in computational infrastructure, has paved the way for researchers to construct the foundations of UQ, and consequently, has increased awareness of UQ as a valuable tool applicable into several scenarios and problems.

Either type of uncertainty (aleatoric, epistemic, or a combination of both) within a system can appear under various settings, can be of different magnitudes, and can be traced back to different sources. The following major sources of uncertainty have been identified [33, 92]:

- *Parameter uncertainty* comes from model parameters that are inputs to a computer model but whose exact values are not known and cannot be directly measured.

- *Parametric uncertainty* comes from the inherent variability present in input variables to a system, which will then be propagated to the QoIs.

- *Model inadequacy*, or model discrepancy, comes from the lack of knowledge of the underlying phenomena of a system (e.g., underlying physics in a thermal problem), which translates to assumptions that take the model apart from the actual true system.

- *Algorithmic uncertainty*, or numerical uncertainty, comes from numerical errors and approximations that occur during the implementation and execution of a computer model.

- *Experimental uncertainty*, or observation error, comes from the variability of experimental measurements which is inevitable and can be characterized by replication of measurements over same experimental settings.

- *Interpolation and extrapolation uncertainty* comes from lack of data for the system under study, which in turn calls for interpolation or extrapolation calculations in order to predict corresponding QoIs.

In general, problems in UQ and its corresponding methodologies can be subdivided into two broad categories: *Forward* UQ or *Uncertainty Propagation* (UP) and *Inverse* UQ, also known as Inverse Problem or Backward UQ.

2.2.1 Forward Uncertainty Quantification

This category of UQ focuses on the characterization and control of uncertainty of system QoIs that results after propagation of the uncertainty introduced by the inputs within the system (i.e., parametric uncertainty). There exist several research efforts centered in UP approaches in different fields of science and engineering. For instance, Lee and Chen [93] presents a comparative study of different UP methods and employs them under different scenarios for reliability-based design optimization. Putko et al. [94] incorporate UP within a robust optimization procedure for high-fidelity computational fluid dynamics tools, while Mathelin et al. [95] use stochastic methods and Monte Carlo samples to propagate uncertainty throughout a turbulent compressible fluid flow

model. Other applications of UP include geophysical mass flows [96] and rainfall models [97].

Even though the field of UQ has been recently taken under serious consideration by practitioners, different tools had already been employed about 20 to 30 years ago but not formally referred as UQ. Some of these cases can be found in [98–100] where Monte Carlo methods for UP were used in applications such as oceanography, geochemistry, and risk assessment.

2.2.2 Inverse Uncertainty Quantification

In Inverse UQ, the focus is to obtain information about the system under study based on observed data. It is called Inverse Problem because it starts with the results (i.e., data) and then calculates or estimates the unknowns from the system. This category has drawn significant attention, especially from the engineering community because of the importance of modeling and data observations that many complex engineering systems rely on.

Many of the sources of uncertainty listed previously can be handled through different Inverse UQ methodologies. For instance, parameter uncertainty, model inadequacy and algorithmic uncertainty can be treated under a framework denominated *statistical calibration*, which involves parameter calibration and model bias correction [92, 101, 102]. This is one of the main topics that will be discussed in the next chapters.

Another important strategy used with Inverse UQ are the construction of *surrogate models*, also known as emulators, meta-models, or response surfaces. This methodology relates to the approximation of mathematical functions to data with the objective of providing fast data-driven modeling and prediction capabilities. This is a major application that helps those applications that include resource-intensive computer models when extensive simulation is prohibitive, those with physical processes where mathematical formulations are non-existent or have not been devised yet, and those where substantial costly experimentation is unpractical. Based on these assertions, L-PBF falls into this category and therefore, does require the formal application of Inverse UQ methodologies.

Similarly as with UP, Inverse UQ has also been used for many years, with strong theoretical foundations developed since the 1950s, although not formally referred as Inverse UQ. Applications

ranged from mining, agriculture to forestry [103], and now have extended into other fields and domains such as healthcare, social and environmental geography, oil and gas exploration, fisheries and animal migration, socioeconomics and econometrics, among many more [104]. Literature related to Inverse UQ also includes problems such as spatial modeling [105], computer model emulation [106], image analysis [107], and supervised classification and prediction [108].

In manufacturing, there is a plethora of literature with formal applications of statistics used for assessment of experimental observations (see for example [109–111]), however, formal practices of UQ in AM, and particularly in L-PBF processes, are still scarce and limited. Nevertheless, it seems highly likely that this will not be the case in the near future, especially with the large efforts that ICME academics and researchers with a focus on AM are investing on. This can be seen in new publications such as [33, 35, 112].

The focus of this dissertation is to present one among the first early efforts to conduct formal systematic UQ in different physical processes that occur within the L-PBF process. The next chapters introduce the UQ methodologies employed and the applications and results after formal utilization of these UQ methodologies.

3. METHODOLOGY

As previously mentioned, UQ is a relative new field that combines theory and knowledge from many scientific fields such as math, statistics, computer science and data analytics, and has become an important component for design, analysis and research of many engineering problems. The approach taken in this dissertation is to investigate and improve the understanding of the L-PBF AM process by making use of several UQ tools according to the problem and objective set to be achieved.

This chapter presents the theoretical foundations (i.e., mathematical methods and theories, statistical and probabilistic models, etc.) as well as experimental systems and procedures that will be used throughout the dissertation. These formulations are given in a general context such that the theory and models can be incorporated to any specific problem, as those presented in Chapters 4 and 5, and/or to any project the reader deems appropriate to employ them to. Therefore, the first section in the chapter is devoted to introduce notation and definitions that most or all of the models commonly share. The body of the chapter then presents all of the statistical models employed for both Forward and Inverse UQ, and in the last section, the main experimental setup is described given the fact that many of the applications presented in the dissertation have used this system up to some degree.

3.1 Common Notation and Definitions

Researchers and academics are often interested on developing formal tools and procedures to study different physical systems through observation of data. The nature of these investigations is to identify different input settings that the system is influenced by, run several experiments at several different combinations of these settings, and conduct inference over a specified QoI. Under this framework, the researcher wants to study the behavior of quantity or measure Y given some set of conditions or settings $\mathbf{x}$ respective to system or process[2] $\mathcal{M}$.

[2]Throughout the dissertation, the words *system*, *process*, or *model* will be used interchangeably to refer to $\mathcal{M}$.

Throughout this dissertation, any mathematical symbol or letter with a standard font denotes a scalar or a function depending the context, for instance:

$$x, Y, \mu, \sigma^2, \rho, k$$

while any mathematical symbol or letter with a bold font denotes a vector, matrix, or multi-dimensional quantity, for instance:

$$\mathbf{x}, \mathbf{Y}, \boldsymbol{\mu}, \boldsymbol{\Sigma}, \boldsymbol{\Psi}$$

The set of conditions or settings to the process will be called *model inputs* and are defined as

$$\mathbf{x} \in \mathcal{X} \subseteq \mathbb{R}^q$$

where $\mathbf{x}$ represents a q-dimensional vector of inputs with domain of definition denoted as $\mathcal{X}$.

Similarly, the set of measures or QoIs will be called *model outputs* or *responses* and are defined as

$$\mathbf{Y} \in \mathcal{Y} \subseteq \mathbb{R}^d$$

where $\mathbf{Y}$ represents a d-dimensional vector of outputs with domain of definition denoted as $\mathcal{Y}$.

Mathematically, process $\mathcal{M}$ can be executed or evaluated at inputs $\mathbf{x}$ to observe response quantities $\mathbf{Y}$ as follows

$$\mathbf{Y} = \mathcal{M}(\mathbf{x}) \tag{3.1}$$

or if the problem is univariate, then it is written as

$$Y = \mathcal{M}(\mathbf{x}) \tag{3.2}$$

Due to resources and time constraints, experiments or computer simulations cannot always be collected, thus the problem is to identify important combinations of input settings and collect the least amount of expensive data while learning the most knowledge possible from the process. The

collection of data at *n* cases will be denoted as the following input and output matrices:

$$\mathbb{X} = \begin{bmatrix} \mathbf{x}_1^\top \\ \mathbf{x}_2^\top \\ \vdots \\ \mathbf{x}_n^\top \end{bmatrix}_{n \times q}, \ \mathbb{Y} = \mathcal{M}(\mathbb{X}) = \begin{bmatrix} \mathbf{Y}_1 = \mathcal{M}(\mathbf{x}_1) \\ \mathbf{Y}_2 = \mathcal{M}(\mathbf{x}_2) \\ \vdots \\ \mathbf{Y}_n = \mathcal{M}(\mathbf{x}_n) \end{bmatrix}_{n \times d} \tag{3.3}$$

Furthermore, in order to avoid confusion or subjectivity, the methodologies presented in this chapter will be referred as *statistical models*, as a manner to distinguish them from the word *model* that will normally refer to $\mathcal{M}$ (an exception is the term *computer model* which depending on the context may or may not refer to $\mathcal{M}$. This will be explicitly defined whenever it is needed).

Additionally, since UQ involves many statistical and probabilistic concepts, Appendix A presents the parameterization of *probability distributions functions* (pdf) for different random variables used across the dissertation. This appendix also provides an introductory definition about Bayesian statistics given that both frequentist and Bayesian approaches are used for solving different L-PBF problems. Moreover, Appendix B presents the definitions and formulations of different *Markov Chain Monte Carlo* (MCMC) algorithms also frequently used in hand with Bayesian statistics in the dissertation.

3.2 Forward Uncertainty Quantification

In this section, we introduce two UP methodologies that deal with representation and assessment of the uncertainty of the response from a system when its inputs are random variables. In other words, the problem setting is that given a set of uncertain inputs to a process, we want to identify the stochastic behavior of the process' response as a result from the propagation of uncertainty. Additionally, we present a second methodology that is centered on the assessment and identification of influential inputs to the model.

3.2.1 Generalized Polynomial Chaos Expansions

3.2.1.1 Univariate Case

As already stated, this statistical model aims to understand and quantify how variability and uncertainty is propagated throughout a model when its inputs are stochastic in nature. Following the formulation by Blatman and Sudret [113], a probability space $(\Omega, \mathcal{F}, \mathcal{P})$ is defined with sample space Ω, σ- algebra $\mathcal{F}$ and probability measure $\mathcal{P}$.

The formulation is first presented in the univariate domain ($d = 1$) and then will be generalized into a multi-output problem. Therefore, the deterministic model from Equation (3.2) is employed, and in this case, input vector $\mathbf{x} = [x_1, \ldots, x_q]^\top$ is a random vector defined by its joint pdf, $p_{\mathtt{X}}(\mathbf{x})$, with marginal pdfs, $p_{\mathtt{X}_i}(x_i) \, \forall i \in \{1, \ldots, q\}$.

In Functional Chaos Expansions, random vector **x** is represented in a Hilbert space $\mathcal{L}_2(\Omega, \mathcal{F}, \mathcal{P})$ of square-integrable functions with respect to $p_{\mathtt{X}}(\mathbf{x})$, with the requirement that all input components have finite second moments:

$$\begin{aligned} \mathbb{E}\left[\mathtt{X}_i^2\right] &= \int_{\Omega} \mathtt{X}_i^2(\omega) \, d\mathcal{P}(\omega) \\ &= \int_{\mathcal{X}_i} x_i^2 p_{\mathtt{X}_i}(x_i) \, dx_i \\ &< +\infty \end{aligned}$$

and thus *inner product* is defined as

$$\langle x_i, x_j \rangle_{\mathcal{L}_2} \equiv \mathbb{E}\left[\mathtt{X}_i \cdot \mathtt{X}_j\right] = \int_{\mathcal{X}} x_i x_j p_{\mathtt{X}}(\mathbf{x}) \, d\mathbf{x} \tag{3.4}$$

Additionally, it is also required that model response *Y* has finite variance, $\mathbb{E}\left[\mathtt{Y}^2\right] < +\infty$, so that the model can be re-formulated in a functional chaos representation, or in other words, as a converging series of known multivariate basis functions $\psi(\mathbf{x})$,

$$Y = \mathcal{M}(\mathbf{x}) = \sum_{\boldsymbol{\alpha} \in \mathbb{N}^q} a_{\boldsymbol{\alpha}} \psi_{\boldsymbol{\alpha}}(\mathbf{x}) \tag{3.5}$$

where $a_{\boldsymbol{\alpha}} \in \mathbb{R}$ are unknown basis coefficients that are to be estimated and $\boldsymbol{\alpha}$ is a q-dimensional index set containing natural numbers $\mathbb{N}$ that will be introduced in the next paragraphs.

When the basis functions $\psi(\mathbf{x})$ from Equation (3.5) are polynomial functions, the expansion is referred as a *Polynomial Chaos Expansion* (PCE). Within PCE framework, polynomials ψ must satisfy Definitions 1 and 2.

Definition 1. For some $z \in \mathcal{Z} \subseteq \mathbb{R}$, a pair of different polynomials $P(z)$ and $Q(z)$ such that $P, Q : \mathcal{Z} \to \mathbb{R}$ are *orthogonal* to each other with respect to some weight function $w(z) > 0$ if and only if,

$$\langle P(z), Q(z) \rangle_{\mathcal{L}_2} = \int_{\mathcal{Z}} P(z) Q(z) w(z) \, dz = 0$$

Definition 2. A polynomial *P* is *orthonormal* with respect to some weight function $w(z) > 0$, if it satisfies Definition 1 and its $\mathcal{L}_2$-norm is equal to 1:

$$\|P(z)\|_{\mathcal{L}_2} = \sqrt{\langle P(z), P(z) \rangle_{\mathcal{L}_2}} = 1$$

The original problem was formulated only for the case with independent and identically distributed (i.i.d.) standard Gaussian vector $\mathbf{x}$ and polynomials ψ of the Hermite sequence (or family)[3] [114]. However, the approach has been studied further and subsequently extended to accommodate more probability distributions and polynomial families (i.e., Askey-scheme polynomials [115]), resulting in *generalized* Polynomial Chaos Expansions (gPCE). Some of these orthonormal polynomial families include [116]:

- Legendre polynomials used with Uniform distributions between -1 and 1
- Hermite polynomials used with Standard Normal distributions

[3] In the context of orthonormal polynomials, the terms *sequence* or *family* imply the same meaning.

- Laguerre polynomials used with Gamma distributions
- Jacobi polynomials used with Beta distributions

Each of these families of orthonormal polynomials share the following recurrence relation relating any three consecutive terms in the sequence (within the same family),

$$\pi_j(z) = (a_j z + b_j)\,\pi_{j-1}(z) + c_j \pi_{j-2}(z)$$

where $\pi_j(z)$ is a polynomial function of degree $j \in \mathbb{N}$ (with initial cases $\pi_{-1}(z) = 0, \pi_0(z) = 1$) and coefficients a_j, b_j, c_j are uniquely defined for each family and for each polynomial degree *j* [117].

In the context of the original model $\mathcal{M}$, we define $\pi_j^{(i)}(x_i)$ to be a polynomial function of degree *j*, $\pi_j^{(i)} : \mathcal{X}_i \to \mathbb{R}$. This polynomial satisfies Definitions 1 and 2 with respect to the marginal pdf of the *i*th input variable, $p_{\mathtt{X}_i}(x_i)$. Consequently, for any two polynomials with degrees *j* and *k* coming from the same family, it follows:

$$\begin{aligned}\left\langle \pi_j^{(i)}(x_i), \pi_k^{(i)}(x_i) \right\rangle_{\mathcal{L}_2} &= \mathbb{E}\left[\pi_j^{(i)}(\mathtt{X}_i) \cdot \pi_k^{(i)}(\mathtt{X}_i)\right] \\ &= \int_{\mathcal{X}_i} \pi_j^{(i)}(x_i)\,\pi_k^{(i)}(x_i)\,p_{\mathtt{X}_i}(x_i)\,dx_i \\ &= \delta_{j,k} \end{aligned} \tag{3.6}$$

where $\delta_{j,k}$ is the Kronecker delta that is equal to 1 when $j = k$ and 0 otherwise.

Multivariate polynomials $\psi(\mathbf{x})$ are calculated by tensorizing all *q* univariate polynomials from every component of **x**, thus

$$\psi_{\boldsymbol{\alpha}}(\mathbf{x}) = \prod_{i=1}^{q} \pi_{\alpha_i}^{(i)}(x_i) \tag{3.7}$$

where index set $\boldsymbol{\alpha} = \{\alpha_1, \ldots, \alpha_q\}$ is the set of indices that indicates the degree for every univariate polynomial π that belongs to ψ, and hence in gPCE context, ψ are called basis functions.

For simplicity, it will be assumed that input components x_i are statistically independent from

each other, $p_{\mathtt{X}}(\mathbf{x}) = \prod_{i=1}^{q} p_{\mathtt{X}_i}(x_i)$, and thus, it can easily be demonstrated that $\psi(\mathbf{x})$ are also orthonormal multivariate polynomials:

$$\begin{aligned}\langle \psi_{\boldsymbol{\beta}}(\mathbf{x}), \psi_{\boldsymbol{\kappa}}(\mathbf{x}) \rangle_{\mathcal{L}_2} &= \mathbb{E}\left[\psi_{\boldsymbol{\beta}}(\mathtt{X}) \cdot \psi_{\boldsymbol{\kappa}}(\mathtt{X})\right] \\ &= \int_{\mathcal{X}} \psi_{\boldsymbol{\beta}}(\mathbf{x}) \psi_{\boldsymbol{\kappa}}(\mathbf{x}) p_{\mathtt{X}}(\mathbf{x}) d\mathbf{x} \\ &= \delta_{\boldsymbol{\beta},\boldsymbol{\kappa}} \end{aligned} \tag{3.8}$$

The case when dealing with statistically correlated inputs x_i's has also been demonstrated, however additional mathematical development that is outside the scope of this dissertation needs to be undertaken [113].

The objective is then to estimate the coefficients $a_{\boldsymbol{\alpha}}$ in Equation (3.5), which will be referred as PC coefficients throughout the dissertation. Different approaches can be followed to achieve this, and in this case, a *non-intrusive regression* method is used to build the gPCE model. The interested reader is referred to the following works for more details regarding the theory and selection of other different methods (such as *projection* techniques) [113, 116, 118].

In order to estimate the PC coefficients through the regression methodology, we collect datasets $\mathbb{X}$ and $\mathbb{Y}$ as presented in Equation (3.3). Since the q columns of the matrix $\mathbb{X}$ typically have different physical units, the elements of this matrix are normalized to the unit hypercube $[0,1]^q$. Additionally, the series in Equation (3.5) is truncated to a default number t to enable computation. This truncation number t describes the maximum polynomial order allowed within the expansion,

$$Y \approx \sum_{|\boldsymbol{\alpha}| \leq t} a_{\boldsymbol{\alpha}} \psi_{\boldsymbol{\alpha}}(\mathbf{x}) \tag{3.9}$$

with $|\boldsymbol{\alpha}| = \sum_{i=1}^{q} \alpha_i$. This truncation method implies that there will be exactly $T = \binom{t+q}{t}$ different basis functions $\psi(\mathbf{x})$ in the summation term in Equation (3.9).

Finally, after accounting for the whole dataset and re-writing in matrix notation, the problem

turns into a linear-regression type:

$$\mathbf{\Psi}\left(\mathbb{X}\right)\mathbf{a}=\mathbb{Y}$$

where $\mathbf{a}=\left[a_{\mathbf{0}}\ldots,a_{\boldsymbol{\alpha}},\ldots\right]_{|\boldsymbol{\alpha}|\leq t}^{\top}$ is the *T*-dimensional vector of PC coefficients and $\mathbf{\Psi}\left(\mathbb{X}\right)$ is a $n\times T$ matrix of bases having the *i*th row equal to $\left[\psi_{\mathbf{0}}\left(\mathbf{x}_i\right)\ldots,\psi_{\boldsymbol{\alpha}}\left(\mathbf{x}_i\right),\ldots\right]_{|\boldsymbol{\alpha}|\leq t}$. Hence, estimation of PC coefficients can be done following any method for linear regression.

It is worth noting that the *null* index set (when $\boldsymbol{\alpha}=\mathbf{0}=\{0,\ldots,0\}$), corresponds to the basis with all univariate polynomials with degree zero, thus

$$\psi_{\mathbf{0}}\left(\mathbf{x}\right)=\prod_{i=1}^{q}\pi_0^{(i)}\left(x_i\right)=1 \tag{3.10}$$

for any orthonormal family. Its corresponding PC coefficient is denoted as $a_{\mathbf{0}}$.

Given the linear model in Equation (3.9), the PC coefficients can be estimated following any standard technique such as Least Squares, Ridge Regression, Lasso Regression, Least Angle Regression, among many. Nevertheless, not all of these methods will work for all cases. For instance, if the number of datapoints *n* is less than *T* (the total number of basis functions), then ill-posed matrices will be present in the linear regression problem and techniques such as Least Squares or Ridge Regression might fail.

A more recent approach is chosen: Elastic Nets regularization developed by Zou and Hastie [119]. This technique involves a combination of Least Squares, Lasso and Ridge regression [120]. Consequently, the method uses both $\mathcal{L}_1$- and $\mathcal{L}_2$-norm to account for:

- Sparsity in the model by variable selection without any limits on the number of selected variables (as opposed to Lasso).
- Strictly convex loss function with a unique minimum (with the inclusion of Ridge).
- Grouping of correlated variables (as opposed to Lasso that selects only one and ignore the rest).

The formulation for the Elastic Net regularization is as follows,

$$\hat{\mathbf{a}} = \arg\min_{\mathbf{a}\in\mathbb{R}^T} \left[\frac{1}{2n} \sum_{i=1}^{n} \left(Y_i - \mathbf{a}^\top \boldsymbol{\psi}\left(\mathbf{x}_i\right) \right)^2 + \lambda \left(\frac{1}{2}\left(1-\gamma\right) \left\| \mathbf{a}_{-\mathbf{0}} \right\|_{\mathcal{L}_2}^2 + \gamma \left\| \mathbf{a}_{-\mathbf{0}} \right\|_{\mathcal{L}_1} \right) \right] \tag{3.11}$$

where $\mathbf{a}_{-\mathbf{0}} = \mathbf{a} \setminus a_{\mathbf{0}}$ is the set of all PC coefficients other than that one corresponding to the null indexed basis; λ and γ are regularization hyperparameters that are to be set prior to minimization. Additionally, norms in this context can be calculated following the general $\mathcal{L}_p$-norm, $\left\| \mathbf{a}_{-\mathbf{0}} \right\|_{\mathcal{L}_p} = \left(\sum_{0<|\boldsymbol{\alpha}|\leq t} |a_{\boldsymbol{\alpha}}^p| \right)^{1/p}$.

In order to best fit the Elastic Nets Regularization model to the collected data, a formal cross validation procedure should be taken as presented in Appendix A.3. Either metric MSPE or MAPE from Equations (A.9) and (A.10) can be used to fine tune the hyperparameter values by assessment of the model performance.

After estimating coefficients $\mathbf{a}$ through Equation (3.11), the non-intrusive gPCE regression method can be thought of as a fast data-driven surrogate for model $\mathcal{M}$ based on the training data, through simply approximating it with Equation (3.9). The last remaining step now is to quantify uncertainty in the model response given uncertainty in model inputs.

It is important to note that this framework will not provide the pdf for the model output $p_{\mathtt{Y}}\left(Y\right)$ in closed form, but will provide useful information about its statistical moments.

The first moment, $\mathbb{E}\left[\mathtt{Y}\right]$, is calculated given the fact that $\psi_{\mathbf{0}}\left(\mathbf{x}\right) = 1$ from Equation (3.10), and the inner product property for multivariate orthonormal polynomials from Equation (3.8), thus

$$\begin{aligned}
\mathbb{E}\left[\mathtt{Y}\right] &= \mathbb{E}\left[\mathtt{Y} \cdot \psi_{\mathbf{0}}\left(\mathtt{X}\right)\right] \\
&= \left\langle Y, \psi_{\mathbf{0}}\left(\mathbf{x}\right) \right\rangle_{\mathcal{L}_2} \\
&= \int_{\mathcal{X}} \left(\sum_{|\boldsymbol{\alpha}|\leq t} \hat{a}_{\boldsymbol{\alpha}} \psi_{\boldsymbol{\alpha}}\left(\mathbf{x}\right) \right) \psi_{\mathbf{0}}\left(\mathbf{x}\right) p_{\mathtt{X}}\left(\mathbf{x}\right) d\mathbf{x}
\end{aligned}$$

$$= \sum_{|\boldsymbol{\alpha}| \leq t} \left[\hat{a}_{\boldsymbol{\alpha}} \int_{\mathcal{X}} \psi_{\boldsymbol{\alpha}} (\mathbf{x}) \, \psi_{\mathbf{0}} (\mathbf{x}) \, p_{\mathtt{X}} (\mathbf{x}) \, d\mathbf{x} \right]$$

$$= \hat{a}_{\mathbf{0}} \tag{3.12}$$

Similarly, for the second moment, it follows that

$$\begin{aligned}
\mathbb{E}\left[\mathtt{Y}^2\right] &= \mathbb{E}\left[\mathtt{Y} \cdot \mathtt{Y}\right] \\
&= \langle Y, Y \rangle_{\mathcal{L}_2} \\
&= \int_{\mathcal{X}} \left(\sum_{|\boldsymbol{\alpha}| \leq t} \hat{a}_{\boldsymbol{\alpha}} \psi_{\boldsymbol{\alpha}} (\mathbf{x}) \right) \left(\sum_{|\boldsymbol{\alpha}| \leq t} \hat{a}_{\boldsymbol{\alpha}} \psi_{\boldsymbol{\alpha}} (\mathbf{x}) \right) p_{\mathtt{X}} (\mathbf{x}) \, d\mathbf{x} \\
&= \sum_{|\boldsymbol{\alpha}| \leq t} \hat{a}_{\boldsymbol{\alpha}}^2
\end{aligned}$$

and the variance of the output distribution equals to

$$\begin{aligned}
\operatorname{var}\left[\mathtt{Y}\right] &= \mathbb{E}\left[\mathtt{Y}^2\right] - \mathbb{E}\left[\mathtt{Y}\right]^2 \\
&= \sum_{|\boldsymbol{\alpha}| \leq t} \hat{a}_{\boldsymbol{\alpha}}^2 - \hat{a}_{\mathbf{0}}^2 \\
&= \sum_{0 < |\boldsymbol{\alpha}| \leq t} \hat{a}_{\boldsymbol{\alpha}}^2
\end{aligned} \tag{3.13}$$

Further moments can be calculated following similar procedures [113].

3.2.1.2 Multivariate Case

For the multivariate case, all the assumptions and requirements explained in the univariate case still apply (e.g., finite second moments for inputs and outputs, inner products, orthogonality and orthonormality, etc.). In the multivariate case, Equation (3.1) is employed, and its functional chaos representation is:

$$Y_j = \mathcal{M}_j (\mathbf{x}) = \sum_{\boldsymbol{\alpha} \in \mathbb{N}^q} a_{\boldsymbol{\alpha},j} \psi_{\boldsymbol{\alpha}} (\mathbf{x}) \quad \forall j \in \{1, \ldots, d\} \tag{3.14}$$

where $a_{\boldsymbol{\alpha},j} \in \mathbb{R}$ are PC coefficients and $\psi_{\boldsymbol{\alpha}}(\mathbf{x})$ are known multivariate orthonormal polynomial functions of degrees indexed by $\boldsymbol{\alpha}$. Similarly as in the univariate case, for computational purposes, the series is truncated up to some value *t*. Additionally, given the result from Equation (3.10) and for simplicity in the formulation, the PC coefficient for the null index is taken out of the series, thus

$$Y_j \approx a_{\mathbf{0},j} + \sum_{0<|\boldsymbol{\alpha}|\leq t} a_{\boldsymbol{\alpha},j}\psi_{\boldsymbol{\alpha}}(\mathbf{x}) \quad \forall j \in \{1,\ldots,d\} \tag{3.15}$$

and in matrix notation:

$$\mathbf{Y} = [\mathbf{A_0}, \mathbf{A}]\,\boldsymbol{\psi}(\mathbf{x})$$

where

$$\mathbf{Y} = \begin{bmatrix} Y_1 \\ \vdots \\ Y_d \end{bmatrix}_{d\times 1}, \mathbf{A_0} = \begin{bmatrix} a_{\mathbf{0},1} \\ \vdots \\ a_{\mathbf{0},d} \end{bmatrix}_{d\times 1},$$

$$\mathbf{A} = \begin{bmatrix} \cdots & a_{\boldsymbol{\alpha},1} & \cdots \\ \vdots & \vdots & \vdots \\ \cdots & a_{\boldsymbol{\alpha},d} & \cdots \end{bmatrix}_{d\times(T-1)} \quad \forall 0 < |\boldsymbol{\alpha}| \leq t,$$

$$\boldsymbol{\psi}(\mathbf{x}) = \begin{bmatrix} \psi_{\mathbf{0}}(\mathbf{x}) \\ \vdots \\ \psi_{\boldsymbol{\alpha}}(\mathbf{x}) \\ \vdots \end{bmatrix}_{T\times 1} \quad \forall\, |\boldsymbol{\alpha}| \leq t$$

After collecting datasets of the form denoted in Equation (3.3), the problem results again into a linear regression problem

$$\mathbb{Y} = \boldsymbol{\Psi}(\mathbb{X})\,[\mathbf{A_0}, \mathbf{A}]^\top$$

and Elastic Nets Regularization is employed to estimate PC coefficients following the formulation

for multi-task learning problems [121],

$$\hat{\mathbf{A}}_{\mathbf{0}}, \hat{\mathbf{A}} = \arg \min_{\mathbf{A_0}, \mathbf{A} \in \mathbb{R}^{T,d}} \frac{1}{2n} \sum_{i=1}^{n} \left\| \mathbf{Y}_i - [\mathbf{A_0}, \mathbf{A}] \, \boldsymbol{\psi}(\mathbf{x}_i) \right\|_F^2 + \lambda \left[\frac{1}{2} (1-\gamma) \left\| \mathbf{A} \right\|_F^2 + \gamma \sum_{j=1}^{T-1} \left\| A_j \right\|_{\mathcal{L}_2} \right] \tag{3.16}$$

where notation $\|\cdot\|_F$ corresponds to the Frobenius norm, A_j is the *j*th column from matrix $\mathbf{A}$ and $\|\cdot\|_{\mathcal{L}_2}$ is the $\mathcal{L}_2$-norm corresponding to a group-lasso penalty[4] [122]. Hyperparameters are also fine-tuned by formal cross validation using either MSPE or MAPE from Equations (A.9) and (A.10) as metrics for model performance.

Lastly, once PC coefficients have been estimated, the output's distribution, $p_{\mathrm{Y}}(\mathbf{Y})$, can be inferred following same procedure as Equations (3.12) and (3.13), hence

$$\mathbb{E}[\mathrm{Y}_j] = \hat{a}_{\mathbf{0},j} \tag{3.17}$$

$$\mathrm{var}[\mathrm{Y}_j] = \sum_{0<|\boldsymbol{\alpha}|\leq t} \hat{a}^2_{\boldsymbol{\alpha},j} \tag{3.18}$$

for all $j \in \{1, \ldots, d\}$.

3.2.2 Global Sensitivity Analysis

In general, *Global Sensitivity Analysis* (GSA) deals with identifying which inputs (or combination of inputs) are influential to a process response, and what the corresponding magnitudes of these influences are, relative to one another. The focus is specifically on *variance-based* GSA methods (also known as *Sobol indices*) since they provide a powerful framework to decompose the variance of the model output and attribute it to different inputs or sets of inputs [123].

Continuing with the original problem setup from Section 3.2.1, model $\mathcal{M}$ is defined in the Hilbert space $\mathcal{L}_2(\Omega, \mathcal{F}, \mathcal{P})$, components of input vector $\mathbf{x}$ are statistically independent from each other and response of the model is univariate. Following formulations provided in Owen [123],

[4]Note that this regularization term is not squared.

the complete set of input indices is denoted as $\mathcal{Q} = \{1, \ldots, q\}$, and a subset of $\mathcal{Q}$ is defined as $u = \left\{j_1, j_2, \ldots, j_{|u|}\right\} \subseteq \mathcal{Q}$, with cardinality $|u|$and complement set denoted as $-u \equiv \mathcal{Q} \setminus u$. Hence, a subset of inputs can be written as $\mathbf{x}_u = \left\{x_{j_1}, \ldots, x_{j_{|u|}}\right\} \in \mathcal{X}_u \subseteq \mathcal{X}$.

Variance-based GSA derives from *Analysis of Variance* (ANOVA) decomposition, where the model under study is decomposed into several functions that depend only on different input subsets,

$$Y = \mathcal{M}(\mathbf{x}) = \sum_{u \subseteq \mathcal{Q}} \mathcal{M}_u(\mathbf{x}) \tag{3.19}$$

where

$$\mathcal{M}_u(\mathbf{x}) = \int_{\mathcal{X}_{-u}} \mathcal{M}(\mathbf{x})\, d\mathbf{x}_{-u} - \sum_{v \subset u} \mathcal{M}_v(\mathbf{x})$$

Under these settings, $\mathbf{x}_u$ is a set of factors and $\mathcal{M}_u$ is the corresponding effect in the model. If $|u| = 1$ then $\mathcal{M}_u$ is called main effect for input x_u. Otherwise, if $|u| > 1$, then $\mathcal{M}_u$ is known as the interaction among all x_j for all $j \in u$.

The complete ANOVA decomposition will have $2^q - 1$ different $\mathcal{M}_u$, and yields the following result:

$$\begin{aligned}\sigma^2 &= \operatorname{var}[\mathcal{M}(\mathbf{x})] \\ &= \sum_{u \subseteq \mathcal{Q}} \sigma_u^2\end{aligned}$$

where $\sigma_u^2 = \int_{\mathcal{X}_u} \mathcal{M}_u(\mathbf{x})^2\, d\mathbf{x}_u$ is the single effect (or partial variance) for $\mathbf{x}_u$. For a more detailed discussion, the reader is referred to [123].

Sobol indices are hence defined as

$$\overline{\tau}_u^2 = \sum_{v \cap u \neq \emptyset} \sigma_v^2 \tag{3.20}$$

$$\underline{\tau}_u^2 = \sum_{v \subseteq u} \sigma_v^2 \tag{3.21}$$

where $\overline{\tau}_u^2$ is called *total sensitivity index*, which counts every ANOVA component that includes

at least one element of set $\mathbf{x}_u$, and $\underline{\tau}_u^2$ is called *closed sensitivity index*, which is the sum of the variance components for set $\mathbf{x}_u$ and all of its subsets. If $\underline{\tau}_u^2$ is large, then set $\mathbf{x}_u$ is important, or if $\overline{\tau}_u^2$ is small, then set $\mathbf{x}_u$ is not important [123]. These indices satisfy $\underline{\tau}_u^2 + \overline{\tau}_{-u}^2 = \sigma^2$, and are usually presented as normalized quantities, $\overline{\tau}_u^2/\sigma^2$ and $\underline{\tau}_u^2/\sigma^2$.

An attractive feature in gPCE is that Sobol indices can be easily calculated as by-products of the procedure, after some adaptation [124]. The gPCE-based ANOVA decomposition (with truncation) is

$$Y \approx \sum_{u \subseteq \mathcal{Q}} \sum_{\boldsymbol{\alpha} \in \boldsymbol{\alpha}_u} a_{\boldsymbol{\alpha}} \psi_{\boldsymbol{\alpha}} (\mathbf{x})$$

where $\boldsymbol{\alpha}_u = \{\boldsymbol{\alpha} \colon \alpha_j > 0 \; \forall j \in u, \; \alpha_k = 0 \; \forall k \notin u, \text{ and } |\boldsymbol{\alpha}| \leq t\}$ which activates those bases that depend only on the inputs indexed by set *u*.

Therefore, given the orthonormality property of polynomials ψ, Sobol indices are calculated as follows:

- gPCE single effect index

$$\sigma_{\mathrm{PC},u}^2 = \sum_{\boldsymbol{\alpha} \in \boldsymbol{\alpha}_u} \hat{a}_{\boldsymbol{\alpha}}^2 \tag{3.22}$$

- gPCE-based closed sensitivity index

$$\underline{\tau}_{\mathrm{PC},u}^2 = \sum_{v \subseteq u} \sum_{\boldsymbol{\alpha} \in \boldsymbol{\alpha}_v} \hat{a}_{\boldsymbol{\alpha}}^2 \tag{3.23}$$

- gPCE-based total sensitivity index

$$\overline{\tau}_{\mathrm{PC},u}^2 = \sum_{\boldsymbol{\alpha} \in \boldsymbol{\alpha}_u} \hat{a}_{\boldsymbol{\alpha}}^2 \tag{3.24}$$

  with the difference that $\boldsymbol{\alpha}_u = \{\boldsymbol{\alpha} \colon \alpha_j > 0 \; \forall j \in u \text{ and } |\boldsymbol{\alpha}| \leq t\}$ in this case.

These sensitivity indices are computed at minimal additional cost, since they only depend on PC coefficients that were already estimated by Equation (3.11), which is the step that represents most of the computational cost. In fact, as the formulation suggests, these indices are calculated by

simply adding coefficients after proper indexing and selection (actions that involve only elementary mathematical and logical operations), thus not incurring additional computational burden.

The generalization of this formulation into the multivariate case is rather straightforward and is analogous as how Equations (3.12) and (3.13) translated into their multivariate counterparts in Equations (3.17) and (3.18).

3.3 Inverse Uncertainty Quantification

The objective of methodologies that fall under this umbrella is to create a mathematical representation of a system by means of observations and data. This representation is called Surrogate Model and is intended for analysis and examination of a system in a fast data-driven manner. This framework can be generalized for any physical process or expensive computational model for which assessment of their response behavior is needed and viable only by sampling few carefully selected experiments or simulations.

3.3.1 Gaussian Processes

3.3.1.1 Univariate Case

Gaussian Process (GP) models are a popular type of statistical model in the area of spatial statistics. A GP model is a non-parametric statistical model in which a stochastic process $f(\cdot)$ is assumed to have all of its finite-dimensional distributions as multivariate normal [103]. In other words, the joint pdf of the outputs from the stochastic process at any finite set of inputs $\{\mathbf{x}_1, \ldots, \mathbf{x}_n\}$ is modeled as an *n*-dimensional normal distribution:

$$p\left(f\left(\mathbf{x}_1\right), \ldots, f\left(\mathbf{x}_n\right)\right) \sim \mathrm{N}_n\left(\boldsymbol{\mu}, \mathbf{C}\right) \tag{3.25}$$

where the mean vector $\boldsymbol{\mu}$ and the covariance function $\mathbf{C}$ are defined by a mean function $\mu(\cdot)$ and covariance function $C(\cdot, \cdot)$, respectively, with the following properties:

$$\mu\left(\mathbf{x}_i\right) = \boldsymbol{\mu}_i = \mathbb{E}\left[f\left(\mathbf{x}_i\right)\right]$$

$$C\left(\mathbf{x}_i, \mathbf{x}_j\right) = \mathbf{C}_{i,j} = \operatorname{cov}\left[f\left(\mathbf{x}_i\right), f\left(\mathbf{x}_j\right)\right]$$

A GP model will be denoted as $f\left(\cdot\right) \sim \mathrm{GP}\left(\mu\left(\cdot\right), C\left(\cdot,\cdot\right)\right)$. A further and detailed explanation on this type of stochastic process is provided in references [103, 108].

The initial problem setting starts again from Equation (3.2), however in this case, model inputs $\mathbf{x}$ are thought of as *locations* on the q-dimensional space $\mathcal{X}$. The task is to find a stochastic function f such that $f\colon \mathcal{X} \to \mathcal{Y}$, which would correspond to a data-driven approximation for model $\mathcal{M}$.

The statistical model is defined as follows,

$$Y = f\left(\mathbf{x}\right) + \epsilon\left(\mathbf{x}\right) \tag{3.26}$$

where $f\left(\cdot\right) \sim \mathrm{GP}\left(\mu\left(\cdot\right), C\left(\cdot,\cdot\right)\right)$ that captures the correlations between different locations $\mathbf{x}$, and $\epsilon\left(\cdot\right)$ is an error term that captures inherent noise associated with the model. The existence of the error term depends on every situation and problem. If dealing with experimental measurements of a physical process, then it is normally included to account for measurement noise. On the other hand, if the model under study is a computer model with minimal to negligible error (be it numerical or any other kind), then oftentimes this term is disregarded [125].

The choices of mean and covariance functions $\mu\left(\cdot\right)$ and $C\left(\cdot,\cdot\right)$, respectively, are important since they characterize the probability distribution on the outputs of the stochastic process $f\left(\cdot\right)$ given in Equation (3.25). Guides for selection of these functions are outside of the scope of this study, and the interested reader should refer to works like [103, 108, 126].

The role of the mean function is to characterize the average or expected value of Y at location $\mathbf{x} \in \mathcal{X}$, while the role of the covariance function is to capture the spatial dependence between two different locations $\mathbf{x}_i, \mathbf{x}_j \in \mathcal{X}$. This implies that if datapoints $\mathbf{x}_i$ and $\mathbf{x}_j$ are spatially close to each other, then the output results Y_i and Y_j will be highly correlated. Conversely, if those two points are spatially distant from each other, then their responses will have minimal correlation.

In order to fit the GP model, data is collected as in Equation (3.3). Since the columns of matrix $\mathbb{X}$ typically have different physical units, the elements of this matrix are normalized to the unit

hypercube $[0,1]^q$. Within the definitions of mean function $\mu(\cdot)$, covariance function $C(\cdot,\cdot)$ and error term $\epsilon(\cdot)$, there may exist the need to define some hyperparameters that these functions rely on. The complete set of these hyperparameters will be denoted as $\boldsymbol{\Omega}$. Then, from the definition in Equation (3.26) and after collection of the dataset, it can be shown that the pdf of the model output vector, otherwise known as *likelihood function* (see Appendix A.2), is given by:

$$p(\mathbb{Y}|\mathbb{X},\boldsymbol{\Omega}) \sim \mathrm{N}_n(\boldsymbol{\mu},\boldsymbol{\Sigma}) \tag{3.27}$$

where $\boldsymbol{\mu}$ is a n-dimensional mean vector calculated by the mean function, $\boldsymbol{\Sigma}$ is the $n \times n$ covariance matrix calculated for each pair of input locations.

A special characteristic of GP models is that prediction is easily achieved based on properties of the multivariate normal distribution, which is usually referred as *Kriging* or *Best Linear Unbiased Predictor* (BLUP),

$$p(\mathbb{Y}_0|\mathbb{Y},\mathbb{X},\mathbb{X}_0,\boldsymbol{\Omega}) \sim \mathrm{N}_{n_0}(\boldsymbol{\mu}_0,\boldsymbol{\Sigma}_0) \tag{3.28}$$

where $\mathbb{X}_0$ is a new set of unobserved input locations of size n_0 where predictions are needed, and

$$\boldsymbol{\mu}_0 = \mu(\mathbb{X}_0) + C(\mathbb{X}_0,\mathbb{X})\,\boldsymbol{\Sigma}^{-1}(\mathbb{Y}-\boldsymbol{\mu}) \tag{3.29}$$

$$\boldsymbol{\Sigma}_0 = C(\mathbb{X}_0,\mathbb{X}_0) - C(\mathbb{X}_0,\mathbb{X})\,\boldsymbol{\Sigma}^{-1}C(\mathbb{X},\mathbb{X}_0) \tag{3.30}$$

It is important to note that all these definitions imply that hyperparameter set $\boldsymbol{\Omega}$ is known. Nevertheless, this is usually not the case, and therefore, throughout this dissertation, a Bayesian approach will be carried out in order to estimate the values of hyperparameters from the data. To achieve this, posterior distributions are formulated based on Appendix A.2 and estimated numerically via MCMC algorithms (see Appendix B). Consequently, Equations (3.29) and (3.30) can be then used with the resulting estimations of $\boldsymbol{\Omega}$, and a formal cross validation procedure is taken to assess and quantify the performance of the model through metrics MSPE or MAPE from Equations (A.9) and (A.10).

A characteristic benefit of this methodology is that it provides bands of prediction confidence through covariance matrix $\boldsymbol{\Sigma}_0$, which are helpful and valuable for modelers to analyze and assess the results and take informed decisions.

3.3.1.2 Multivariate Case

Generalizing the univariate formulation of a GP and following formulations by Gelfand et al. [103], the joint pdf from Equation (3.25) follows a *matrix-variate* normal distribution denoted as

$$p\left(f\left(\mathbf{x}_1\right), \ldots, f\left(\mathbf{x}_n\right)\right) \sim \mathrm{N}_{n,d}\left(\boldsymbol{\mu}, \mathbf{C}\right) \tag{3.31}$$

with mean matrix $\boldsymbol{\mu}$ and cross-covariance matrix $\mathbf{C}$. Furthermore, a multivariate GP will be denoted as $f\left(\cdot\right) \sim \mathrm{GP}_d\left(\mu\left(\cdot\right), C\left(\cdot,\cdot\right)\right)$ where $\mu\left(\cdot\right)$ is the mean function which is a matrix-valued mapping $\mu\colon \mathcal{X} \to \mathbb{R}^d$, while $C\left(\cdot,\cdot\right)$ is a positive definite cross-covariance function accounting for correlation for domains $\mathcal{X}$ and $\mathcal{Y}$, that maps $C\colon \mathcal{X} \times \mathcal{X} \to \mathbb{R}^{d,d}$ following next equation form

$$C\left(\cdot,\cdot\right) = \begin{bmatrix} c_{1,1}\left(\cdot,\cdot\right) & \cdots & c_{1,d}\left(\cdot,\cdot\right) \\ \vdots & \ddots & \vdots \\ c_{d,1}\left(\cdot,\cdot\right) & \cdots & c_{d,d}\left(\cdot,\cdot\right) \end{bmatrix} \tag{3.32}$$

for some functions $c_{i,j}\colon \mathcal{X} \times \mathcal{X} \to \mathbb{R}$ that account for correlations between output response *i* and *j*.

Under these settings, the initial step starts with model from Equation (3.1), and again the task is to find a stochastic function f such that $f\colon \mathcal{X} \to \mathcal{Y}$, which would correspond to a data-driven approximation for model $\mathcal{M}$, thus

$$\mathbf{Y} = f\left(\mathbf{x}\right) + \epsilon\left(\mathbf{x}\right) \tag{3.33}$$

where $f\left(\cdot\right) \sim \mathrm{GP}_d\left(\mu\left(\cdot\right), C\left(\cdot,\cdot\right)\right)$ that captures spatial relationships between both inputs and outputs.

After data collection, the likelihood function under this multivariate model is given by

$$p\left(\mathbb{Y}|\mathbb{X}, \boldsymbol{\Omega}\right) \sim \mathrm{N}_{n,d}\left(\boldsymbol{\mu}, \boldsymbol{\Sigma}\right) \tag{3.34}$$

where $\boldsymbol{\mu}$ is the $n \times d$ mean matrix calculated by the mean function, $\boldsymbol{\Sigma}$ is the $n \cdot d \times n \cdot d$ cross-covariance matrix resulting from the cross-covariance function.

A widely used specification is the *separable model* approach for the cross-covariance function, which redefines it as

$$C(\cdot, \cdot) = r(\cdot, \cdot) \boldsymbol{\Lambda} \tag{3.35}$$

where $r(\cdot, \cdot)$ is a positive definite correlation function accounting for correlation in the input space $\mathcal{X}$ and $\boldsymbol{\Lambda} \in \mathbb{R}_{+}^{d,d}$ is a positive definite matrix accounting for correlations between outputs [103]. Hence, the cross-covariance matrix is calculated as follows

$$\boldsymbol{\Sigma} = \mathbf{R} \otimes \boldsymbol{\Lambda} \tag{3.36}$$

where $\otimes$ is the Kronecker product, and $\mathbf{R}$ is the $n \times n$ matrix calculated through correlation function *r* at every pair of input locations.

In regards of predictive calculations, Gaussian properties are generalized for the predictive pdf shown in Equation (3.28), and similarly, Kriging values (or BLUP) are calculated following the same patterns as Equations (3.29) and (3.30) (after proper generalization to higher dimensions).

Additionally, since these definitions imply that hyperparameter set $\boldsymbol{\Omega}$ is known, a Bayesian approach will be taken again to estimate the values of hyperparameters numerically via the MCMC algorithms presented in Appendix B. Consequently, predictions can be calculated using the generalized versions of Equations (3.29) and (3.30) with the resulting estimations of $\boldsymbol{\Omega}$, and a formal cross validation procedure can be taken to assess and quantify the performance of the model through metrics MSPE or MAPE from Equations (A.9) and (A.10).

3.4 Experimental Setup

3.4.1 Laser Powder-Bed Fusion System

Throughout the dissertation, most experimental work (unless specifically noted) was carried out using a ProX 100 DMP L-PBF system developed by 3D Systems Inc. and is shown on Fig-

Figure 3.1: 3D Systems ProX 100 DMP L-PBF system. Reprinted with permission from [42].

ure 3.1. The system is equipped with a fiber laser beam having a Gaussian profile, wavelength of $1070\,\mathrm{nm}$, beam diameter of approximately $70\,\mu\mathrm{m}$ to $100\,\mu\mathrm{m}$, and a maximum laser beam power of $50\,\mathrm{W}$. All printed samples under this manufacturing system are built under a protective inert Argon atmosphere with less than $500\,\mathrm{ppm}$ O_2-level.

Samples printed with this machine are fully defined by a CAD model specifying dimensions, and a set of processing parameters that highly influence the mechanical properties for each sample. Specifically, processing parameters that need to be set to the machine are:

- Laser power (P): it has a maximum limit of $50\,\mathrm{W}$ and can only be set to integer values of W.
- Scanning speed (v): no maximum limit for this parameter but any value above $2500\,{}^{\mathrm{mm}}/_{\mathrm{s}}$ is not recommended by the OEM since it can affect the accuracy of printed parts. This parameter can only be set to integer values of ${}^{\mathrm{mm}}/_{\mathrm{s}}$.
- Hatch distance: no maximum limit for this parameter, and it can be varied to achieve different degrees of porosity. This parameter can only be set to integer values of $\mu\mathrm{m}$, and if not

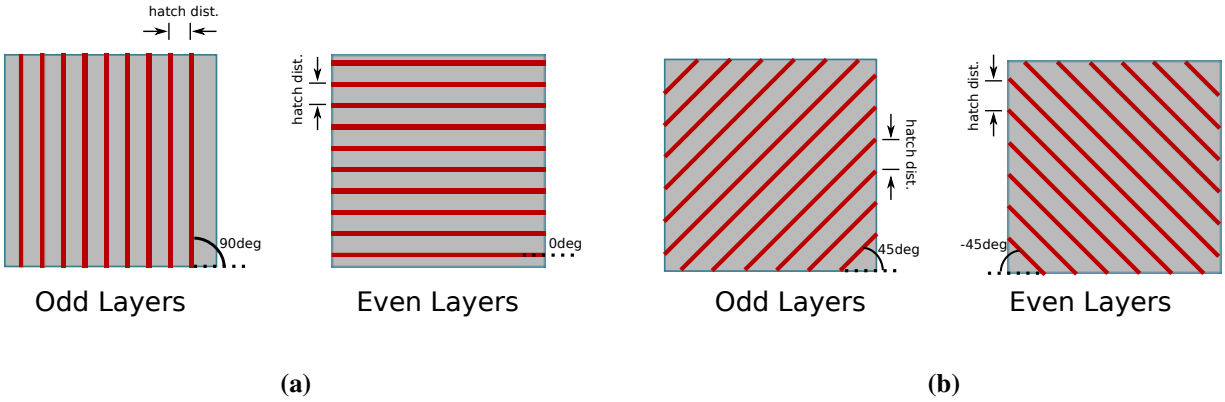

Figure 3.2: Graphical description of scanning strategy settings specified by the rastering angle relative to the build-plane coordinate axis. **(a)** Angle of $90°$ and $0°$. **(b)** Angle of $45°$ and $-45°$.

specified, the default value is $100\,\mu\mathrm{m}$. Furthermore, its value do not influence any outcome when dealing with single-track experiments.

- Layer thickness: no maximum limit for this parameter but can only be set to integer values of $\mu\mathrm{m}$. If not specified, the default value is $30\,\mu\mathrm{m}$.

- Scanning strategy: the scanning pattern can be selected as the rastering angle (relative to the build-plane coordinate axis) which the laser follows parallel while scanning the part. This angle can be differently set for both even and odd layers. Figure 3.2 shows a graphical description of this parameter.

It has to be noted that although laser beam size ($D4$) is an important and influential L-PBF processing parameter, hardware restrictions in the machine do not allow for variation of this parameter.

3.4.2 Thermal Monitoring System

The L-PBF system was custom integrated with a thermal imaging sensor to conduct in-situ monitoring of melt pool temperature during fabrication (see Figures 3.3a and 3.3b). The sensor is a two-wavelength imaging pyrometer, model ThermaVIZ and developed by Stratonics Inc.

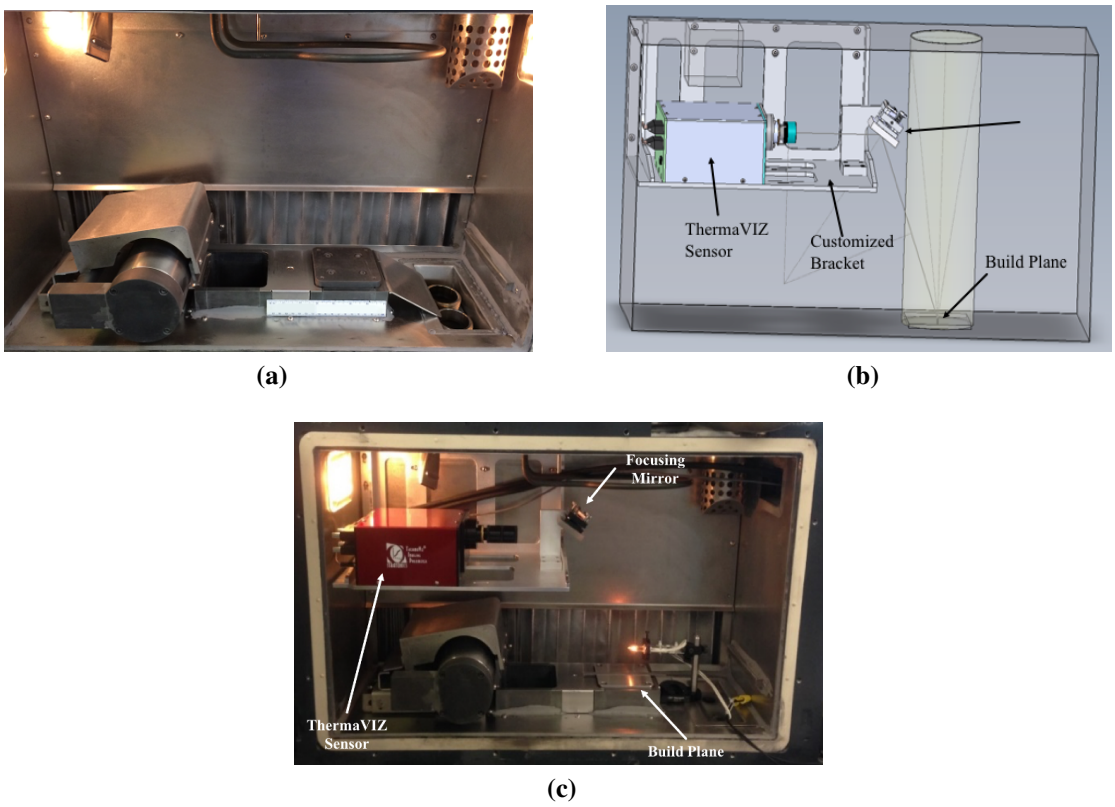

(a) **(b)**

(c)

Figure 3.3: Inside view of the build chamber and pyrometer integration. **(a)** Initial state of the build chamber. Reprinted with permission from [42] **(b)** Final drawing for pyrometer integration. **(c)** Pyrometer integrated into the build chamber for thermal measurements during L-PBF manufacturing.

Figure 3.3c presents the final integration within the manufacturing chamber, which consists of two high resolution CMOS imaging detectors, both having a *field of view* (FOV) resolution of $1300\,\text{pixel} \times 1000\,\text{pixel}$ mapped to a $30 \times 27\,\text{mm}^2$ area, which yields a resolution of $24\,{}^{\mu\text{m}}/_{\text{pixel}}$.

Technical calibration of the pyrometer was performed in-situ after installation using a tungsten filament (halogen tungsten-lamp) for a range of temperatures between $1500\,^{\circ}\text{C}$ to $2500\,^{\circ}\text{C}$. For appropriate collection of thermal data, fabrication of parts has to be placed within the boundaries of the FOV, with the pyrometer capable of taking thermal images of the melt pools at approximately $250\,\text{Hz}$.

Additionally, a setting named *exposure* is a major parameter for the correct measurement of temperature by the pyrometer. This term comes from photography and it relates to the amount of

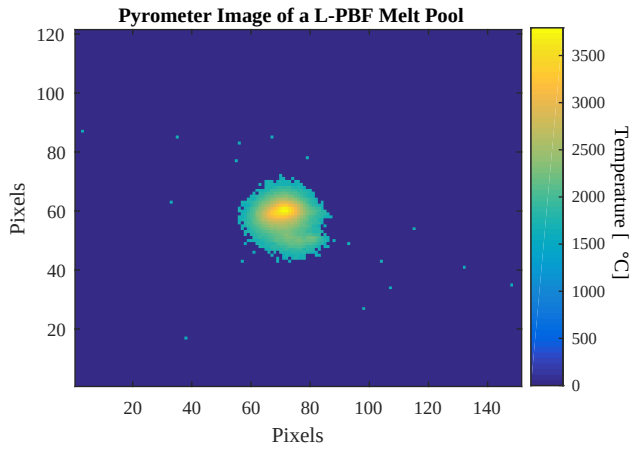

Figure 3.4: Thermal image obtained by the pyrometer.

light per unit area reaching the electronic image sensor after a certain amount of time determined by the shutter speed, lens aperture and scene luminance [127]. Appropriate adjustment for exposure is needed in order to avoid incorrect measurements due to saturation of signal (i.e., light) received by the sensor.

A sample thermal image is presented in Figure 3.4 where both coordinate axes are shown pixel units, while the color scale represents temperature. The data from this plot can be used for analysis of temperature behavior that may include metrics like peak temperatures, temperature history, cooling rates and spatial temperature gradients. It is worth to note that the temperature map will show value of zero for temperature below $1500\,^{\circ}\mathrm{C}$ that fall outside the calibration range of the pyrometer.

In the following chapters, different applications of the described methodologies will be presented along with results and validations demonstrating the value and benefit that UQ provides for the L-PBF manufacturing field.

4. FORWARD UNCERTAINTY QUANTIFICATION

In this chapter, three different approaches for UP will be applied to L-PBF problems. Section 4.1 presents the use of a gPCE model in order to validate an analytic reduced-order thermal model developed for L-PBF. Next in Section 4.2, GSA based on the gPCE model is shown in order to identify the most influential inputs to the thermal model. Lastly, Section 4.3 provides a formal assessment for validation metrics of L-PBF thermal models through multivariate gPCE modeling.

4.1 Formal Validation of an Analytic Thermal Model

Throughout this dissertation, the focus has been repeatedly pointed towards the paramount need of computer modeling in the L-PBF process. In this problem, the model developed by Eagar and Tsai [128] is employed to characterize its response uncertainty given variability on its inputs with the purpose of experimentally validating it via a UP gPCE methodology presented in Section 3.2.1. This model considers a traveling heat source with a Gaussian profile on a flat metallic plate and calculates temperature distributions across the plate. For simplification, the model is referred as the *Eagar-Tsai* (or ET) model hereafter.

This model has been the baseline model of choice in several important prior studies in the L-PBF domain since it simulates the basic operation that takes place during the process (i.e., heat source scanning on a plate. Note that no powder is accounted for nor simulated). It also provides insight on the resulting thermal history which can be then used to extend further studies on the full process with powder particles being accounted for. For instance, King et al. [129] uses the ET model to understand how melt pool characteristics behave based on a fractional factorial design of the inputs. Kamath [125] and King et al. [77] present a data-driven framework that employs the ET model to construct a predictive surrogate model. They use several sampling techniques such as Random and Best Candidate Sampling, along with Decision Trees surrogate models, to show how these data-driven approaches can be used in lieu of the actual ET model. Lastly, Kamath et al. [130] used the ET model simulations with simple single-track experiments to guide parameter selection

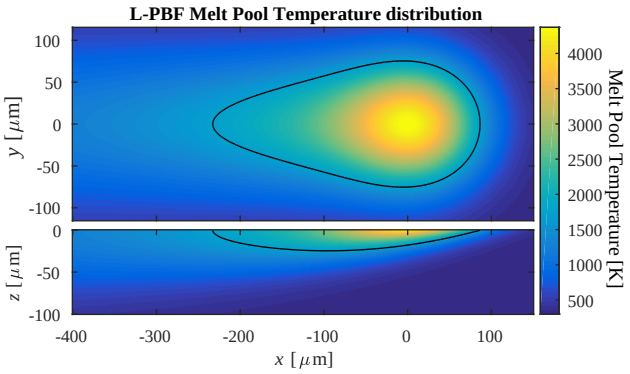

Figure 4.1: Eagar-Tsai model simulation. Plane *xy* shown at level $z = 0$, and plane *xz* shown at level $y = 0$.

for building high-density L-PBF parts. Examples of other research studies that utilized ET model in domains other than AM include [131, 132].

The model takes two main groups of inputs:

- Heat Source parameters: net heat input per unit time *P*, travel speed *v*, and parameter *D* describing the heat source profile.
- Material parameters: thermal conductivity *k*, specific heat capacity c_p, density ρ, and absorptivity *A*.

Since our interest is on L-PBF processes, the analogous heat source parameters are: laser power *P*, scanning speed *v*, and gaussian-distributed laser beam size *D*4. An example of a solution provided by the ET model is presented in Figure 4.1, in which a simulation was run with the following laser parameters $P = 200\,\mathrm{W}$, $v = 2.5\,{}^{\mathrm{m}}/_{\mathrm{s}}$, $D4 = 100\,\mu\mathrm{m}$, and 430F Stainless Steel as the material system for the substrate plate.

The ET model is important and relevant to the L-PBF process since it is a starting point in understanding the interaction between a moving heat source (the laser beam) onto a metal substrate plate, and the corresponding thermal phenomena behavior. In other words, it is considered and used in many previous research efforts as a first approximation of the basic operating principle of L-PBF, despite the fact that it does not include melting of powder particles.

The problem is posed as the following situation: in building a part using L-PBF, the machine operator sets nominal values for the processing parameters (for example, set the laser power *P* to $200\,\mathrm{W}$). In many existing commercial L-PBF systems, the actual realized values of the processing parameters might deviate from the nominal values set by the user. This has often been identified as one possible candidate to explain some of the reasons for the low repeatability of L-PBF parts (and metal AM parts in general). Currently, it is generally assumed that the actual values of the processing parameters would exhibit some degree of variability around their nominal set values. Therefore, we need to quantify the variability in the properties of the fabricated part influenced by the variability in the actual values of the processing parameters.

Therefore, formal UP is demonstrated on the ET model for 430F Stainless Steel, since the ET model will then be validated via experimental measurements produced with the 3D Systems ProX 100 DMP L-PBF system (Section 3.4) on a bare metallic substrate plate made of 430F Stainless Steel. Process parameters are set to nominal values based on the recommendations of the L-PBF system manufacturer in addition to the author's domain knowledge from previous processing of different stainless steel alloys (in particular 17-4 PH and 316L stainless steel alloys). Based on this information, the following probability distributions are assumed for the input parameters of the model:

- Laser power: nominal at $49\,\mathrm{W}$, assumed to follow a normal distribution with: $P\,[\mathrm{W}] \sim \mathrm{N}\,(49, 0.5^2)$.
- Scanning speed: nominal at $0.15\,{}^{\mathrm{m}}/_{\mathrm{s}}$, assumed to follow a uniform distribution with: $v\,[{}^{\mathrm{m}}/_{\mathrm{s}}] \sim \mathrm{U}\,(0.10, 0.20)$.
- Laser beam size: nominal at $70\,\mu\mathrm{m}$ to $100\,\mu\mathrm{m}$, assumed to follow a uniform distribution with: $D4\,[\mu\mathrm{m}] \sim \mathrm{U}\,(70, 100)$.

The material properties for 430F Stainless Steel based on [133] are the following: $k = 26.3\,{}^{\mathrm{W}}/_{\mathrm{m}\cdot\mathrm{K}}$, $c_p = 0.46\,{}^{\mathrm{J}}/_{\mathrm{g}\cdot\mathrm{K}}$, $\rho = 7.8\,{}^{\mathrm{g}}/_{\mathrm{cm}^3}$, $A = 0.3$, and a melting point of $T_m = 1460\,\mathrm{K}$.

The QoI for this model will be melt pool width, since it can be easily inferred from the temperature distributions calculated by the ET model (see Figure 4.1), and additionally it is straightforward to experimentally measure through optical microscopy for single-track experiments.

In order to propagate the uncertainty through the ET model, a gPCE framework was employed with a *sparse* and *adaptive sampling* methodology. This is an iterative methodology, where each iteration involves sampling of a new batch of datapoints to fit the gPCE model until some target performance metric is met. Specifically, a number of datapoints is sampled from their corresponding distributions in each iteration, a non-intrusive regression-based gPCE model is fit with the aggregated data, and formal cross validation is used to assess model performance. Finally, based on a set value for cross validation error target (set by the user), either a new iteration is run if the target was not met, or the procedure is successfully finished if the target has been met.

The methodology was first introduced by Blatman and Sudret [113], however in the present work Elastic Nets Regularization is utilized for sparsity since it involves a variable selection step as part of the procedure that identifies some of the bases from Equation (3.9) as insignificant and set their corresponding PC coefficients at zero. Further, the adaptive sampling technique only adds new information to the model when it has not met the cross validation target, in contrast to classical samples procedures where a single dataset is employed with fixed number of design points set a priori.

The whole procedure is presented in Algorithm 4.1 and is set as follows:

- Each iteration adds 10 new datapoints to the dataset sampled from a scrambled Sobol's quasi-random uniform sequence generator [134], and then convert it to the corresponding probability distributions.
- Model performance is measured using 10-fold Cross Validation (CV) with MAPE as metric.
- Error target is set to $0.25\,\mu\mathrm{m}$ since we are using melt pool width as model metric, or until convergence has been achieved.
- Polynomial truncation is set at $t = 4$ for Equation (3.9).

Algorithm 4.1 Pseudocode for the sparse adaptive gPCE methodology.

Start with empty dataset $\mathbb{X} \leftarrow \emptyset, \mathbb{Y} \leftarrow \emptyset$
target $\leftarrow$ CV error target
$\text{error} \leftarrow \infty$ ▷Initialize error to infinity
while $\text{error} > \text{target}$ **do**
  Draw new samples from $\mathbb{X}_{\text{new}} \sim p_{\mathbf{X}}(\mathbf{x})$
  $\mathbb{Y}_{\text{new}} = \text{ET}(\mathbb{X}_{\text{new}})$ ▷Evaluate only $\mathbb{X}_{\text{new}}$ on the ET model
  Append data $\mathbb{X} \leftarrow \mathbb{X} \cup \mathbb{X}_{\text{new}}$ and $\mathbb{Y} \leftarrow \mathbb{Y} \cup \mathbb{Y}_{\text{new}}$
  Estimate coefficients $\mathbf{a}$ with Equation (3.11)
  $\text{error} \leftarrow \text{CV}(\mathbb{X}, \mathbb{Y}, \hat{\mathbf{a}})$ ▷Perform 10-fold CV with MAPE to gPCE model
end while
return $\hat{\mathbf{a}}$
Perform UP gPCE estimations based on $\hat{\mathbf{a}}$

The complete sparse adaptive methodology was executed and successfully finished after achieving the cross validation target error in the 7th iteration. The path of CV error is shown in Figure 4.2a, which implies that only 70 total simulations of the ET model (with execution time of less than 1 hour) were required until the algorithm converged.

An extra validation step was further implemented, in which 25 new datapoints were sampled and evaluated with the ET model. This set of 25 new datapoints represented a test dataset, and was then compared to the predictions obtained using the gPCE model as shown in Figure 4.2b. An error of $\text{MAPE} = 0.2997\,\mu\text{m}$ was achieved, corroborating the good performance of the model over datapoints not previously used for training.

After first validations of the gPCE model through CV, a second validation approach is carried out employing the propagated output distribution results from Equations (3.12) and (3.13) and comparing them to a brute force Monte Carlo sampling benchmark. The implementation of this benchmark involved sampling of 15,000 datapoints from the input distributions and their respective evaluation using the ET model. The complete histogram of the MC dataset is shown in Figure 4.3.

Statistical moments based on gPCE and MC are presented in Table 4.1. It can be seen that the gPCE model first moment (mean) and second moment (represented by the standard deviation) are within $0.01\,\%$ from the moments computed using brute force MC. However, the latter required

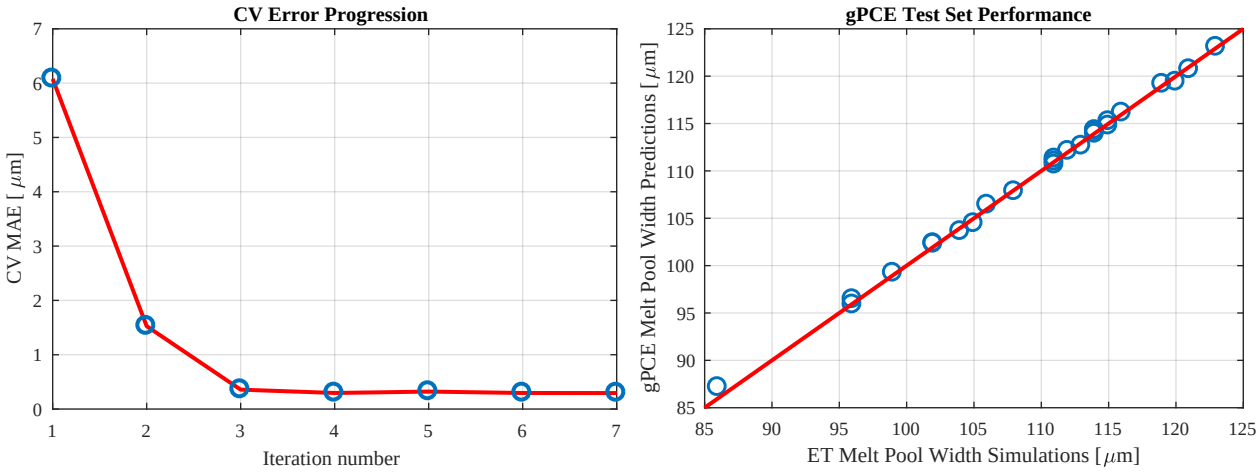

Figure 4.2: Performance of the sparse gPCE adaptive sampling algorithm on the ET model. **(a)** CV error history after 7 iterations showing convergence. **(b)** Performance of the gPCE model over the test set.

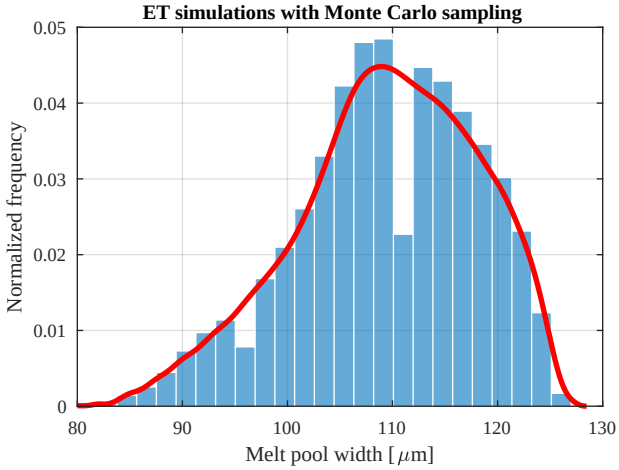

Figure 4.3: Monte Carlo benchmark samples for the ET model. Histogram (blue bins) with a kernel density estimate (red line) after 15,000 ET simulations.

Table 4.1: Statistical moments for the distributions of melt pool width based on gPCE and MC.

Method	Mean [µm]	Std. Dev. [µm]	Number of datapoints
gPCE	109.3937	8.4744	70
MC	109.4061	8.5766	15,000

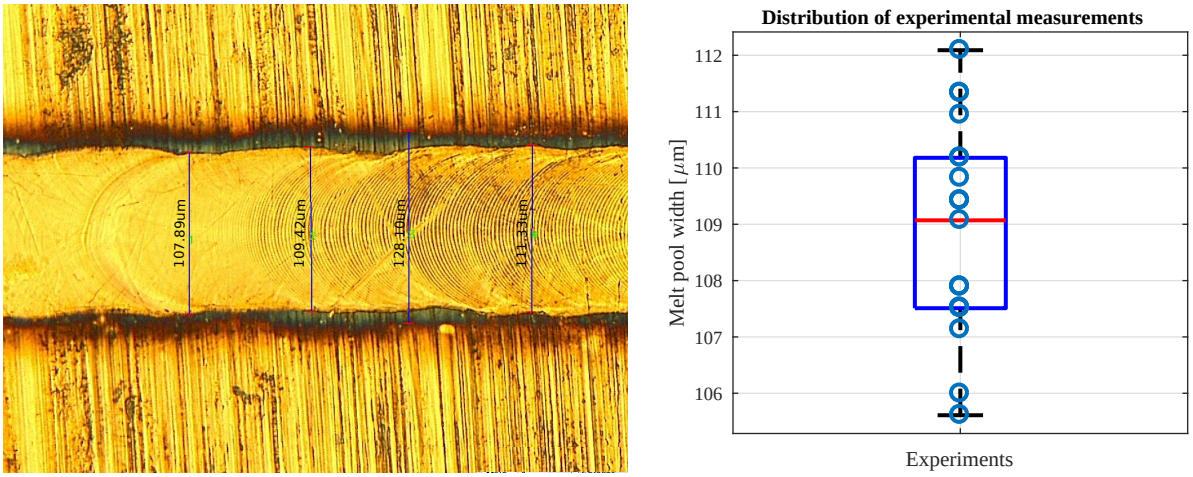

(a) **(b)**

Figure 4.4: Experimental measurements of single tracks for validation of ET model. **(a)** Optical microscopy image of a single track. **(b)** Distribution of the experimental dataset.

more data samples than gPCE, with a factor of approximately 200. In other words, the gPCE framework yielded similar results to MC, but with a small fraction of computational time. The computational saving offered by gPCE will be even much more when an expensive computational model is involved.

Once the gPCE model has been successfully validated, it is used to experimentally validate the ET model with observations. In order to do this, several single tracks were printed on a solid 430F stainless steel substrate at laser settings $P = 49\,\mathrm{W}$ and $v = 0.15\,{}^{\mathrm{m}}/_{\mathrm{s}}$, and characterized under an optical microscope by measuring their widths. An image of one of the samples is presented in Figure 4.4a, while a representation of the experimental data distribution through a box plot is illustrated in Figure 4.4b.

Formal validation is conducted by a hypothesis testing method similar to the one previously used in [135, 136]: for a given confidence interval $100 \times (1-\alpha)\,\%$ at a specific statistical significance level α, the physical experiments are compared to the simulation model predictions. If experimental measurements fall within the distribution of the results obtained from the simulation model, the null hypothesis that the simulation model is not consistent with experimental results is rejected at level of significance α.

Figure 4.5 displays the results for this experimental validation. The blue histogram represents the 15,000 ET simulations sampled from MC after Box-Cox transformation and standardization (i.e., mean 0 and variance 1), and the red curve is a kernel density estimate of the histogram data. Next, the gPCE results (first and second statistical moments) are approximated to a Normal distribution, which after standardization becomes the standard Normal pdf represented by the yellow curve. It can be seen that the red and yellow curves closely approximate to each other, reiterating the validity of the gPCE framework.

Additionally on Figure 4.5, the dashed vertical black lines represent the confidence interval at significance level $\alpha = 5\%$, while the purple circles represent the experimental observations under optical microscopy of the melt pool width after respective transformation and standardization (the position of the experimental observations on the vertical axis is solely for visual comparison within the histogram). It is clear that experiments are within the distribution of simulation results, and therefore we reject the null hypothesis that the ET model is not consistent with experimental results at $5\,\%$ level of significance.

In the next section, a continuation of this problem will be presented where GSA for the ET model is calculated based on the gPCE results.

4.2 Sensitivity Analysis of an Analytic Thermal Model

This section presents an assessment of how the uncertainty in the output of the ET model can be apportioned to the different model inputs by employing the methodology and derivations from Section 3.2.2 along with the gPCE results from the previous section.

Therefore, using the gPCE model for the ET model built in Section 4.1 along with Equa-

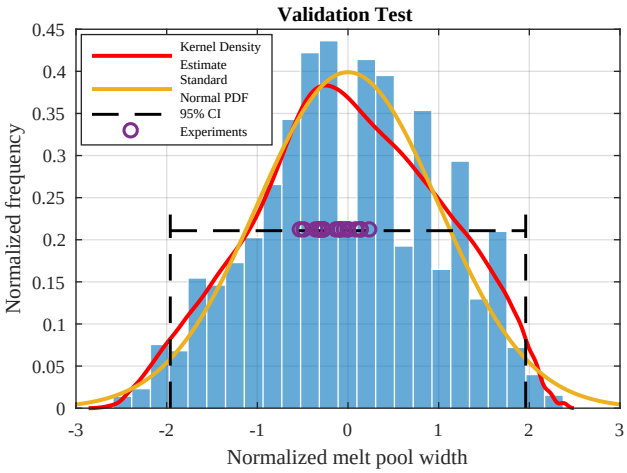

Figure 4.5: Experimental validation of the ET model via UP gPCE.

tions (3.22) and (3.24), both gPCE-based normalized single effect Sobol indices and the total sensitivity indices are computed and shown in both panes of Figure 4.6. As expected, both types of indices yield very similar values given the fact that in the Elastic Nets Regularization step, many bases were deemed as non-important and their corresponding PC coefficients were set to zero. The remaining "active" bases were attributed with more influence over the model, and therefore contributing with more variance over the output.

Additionally, the results indicate that the scanning speed is the most influential input in our particular analysis, followed by laser beam size. An interesting, and somewhat unexpected, observation is that laser power is not recognized as very influential, with its significance being on par with the interaction between the laser speed and laser beam size. A possible explanation is that the laser power used in the study is comparatively low due to the maximum power limitation of the commercial L-PBF system, which restricted the parameter to be set at low variability (represented by a low value of the standard deviation: $P\,[\mathrm{W}] \sim \mathrm{N}\,(49, 0.5^2)$). Nevertheless, this result may confirm that some narrow variability of a few watts in laser power can be tolerated, while the same is not true in the case of scanning speed or laser beam size.

The last section of this chapter will present a formal assessment for different L-PBF metrics used to validate thermal models in a multivariate UP gPCE framework.

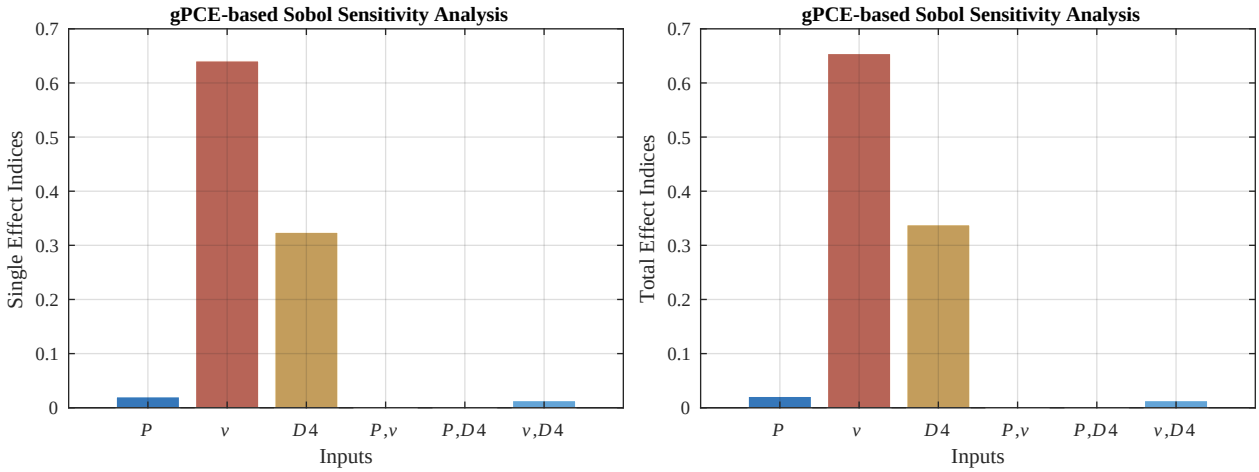

Figure 4.6: GSA of the ET model calculated through gPCE-based Sobol indices. **(a)** Normalized single effect and two-way interaction indices. **(b)** Normalized total sensitivity Sobol indices.

4.3 Assessment of Fundamental Metrics for Validation of Thermal Models

As presented in Section 2.1.3, there has been an increase in research and studies for computer and simulation thermal modeling on L-PBF given the fact that the physics and principles are mostly thermal in nature. Nevertheless, many of these models are being validated only through melt pool characteristics, with no experimental understanding of other influential metrics within the process such as cooling rates, spatial gradients, or peak temperatures. Although melt pool characteristics are of paramount importance for the understanding of the L-PBF process, this section shows that melt pool characteristics should not be solely used to validate and verify these thermal models, and instead more metrics are to be used for a more complete and scientific validation.

In order to carry out this analysis, a multivariate UP approach through gPCE will be employed by following the formulations presented in Section 3.2.1, as well as the adaptive iterative methodology from Section 4.1. The thermal model under consideration is continuum-scale FEM model developed at NASA Langley Research Center using its proprietary code base named SIERRA, hence this model will be referred as the *SIERRA model* hereafter.

The multivariate gPCE methodology is employed into the SIERRA model to assess the vari-

ability of several metrics and descriptors to the L-PBF process. To start off with the methodology, a preliminary study was undertaken for selection of the input variables. Candidates for the study are all material properties since these quantities present the most uncertainty to modelers due to the difficulties for physically measuring them, existence of different measuring techniques and procedures, or simply different values reported to the community.

The preliminary study consisted in selecting a number of material properties (and one laser parameter) and run the SIERRA model at different configurations varying each one of them at a time based on some choices of probability distributions. Table 4.2 presents a summary of the preliminary study, where an important field in this table is column *Type*, which denotes whether a candidate parameter is constant or temperature-dependent within the implementation of the simulation model. In the case for constant parameters, their probability distributions were defined around their nominal values (see for example *Absorptivity*), however, for temperature-dependent parameters, uncertainty was introduced as a function of temperature following the next formula,

$$\text{property}\,(T) = a\,(T) + \delta \cdot b\,(T)$$

where $a\,(T)$ is the temperature-dependent value of the property, δ is the parameter introducing uncertainty in the form of probability distribution $p_{\boldsymbol{\delta}}\,(\delta)$, and $b\,(T)$ is a function in charge of coupling the uncertainty of δ as a function of temperature to the property value. Under this structure, the selected configuration for *a* and *b* yield the next equation:

$$\text{property}\,(T) = \text{nominal}\,(T)\,(1 + 0.1\delta) \tag{4.1}$$

where $a\,(T) = \text{nominal}\,(T)$ or the nominal value of the property as a function of temperature, and $b\,(T) = 0.1 \times \text{nominal}\,(T)$ or 10% of the nominal value. Since some material properties increase two- or three-fold as temperature increases, this choice for $b\,(T)$ paired with $\delta \sim \text{N}\,(0, 1)$ makes Equation (4.1) to properly account to these changes in value and magnitude and adapt the uncertainty input by δ. Nevertheless, this is an ad-hoc method to introduce functional uncertainty

Table 4.2: Preliminary study for selection of relevant material properties to the SIERRA model.

Type	Parameter	Nominal	PDF
Constant	Emmisivity [%]	0.7	$\mathrm{U}\,(0.5, 0.9)$
	Latent heat of fusion [$^{\mathrm{J}}/_{\mathrm{kg}}$]	0.286	$\mathrm{N}\,(0.286, 0.01)$
	Absorptivity [%]	0.7	$\mathrm{U}\,(0.5, 0.9)$
	Laser beam width [$\mu\mathrm{m}$]	70	$\mathrm{U}\,(67.5, 72.5)$
	Melt range temperature [$^{\circ}\mathrm{C}$]	46	$\mathrm{U}\,(30, 80)$
Temperature-dependent	Thermal conductivity of the substrate - δ	-	$\mathrm{N}\,(0, 1)$
	Thermal conductivity of the powder - δ	-	$\mathrm{N}\,(0, 1)$
	Density of the substrate - δ	-	$\mathrm{N}\,(0, 1)$
	Density of the powder - δ	-	$\mathrm{N}\,(0, 1)$

into the model with the benefit of only having to define one single random variable per property, as opposed to change the variance of δ as a function of temperature (i.e., $\delta \sim \mathrm{N}\,(0, \sigma^2\,(T))$), that would imply definition of infinite different random variables.

After proper analysis of the simulations given the distributions from Table 4.2, the final selection from the preliminary study was:

- Inputs to the gPCE model
  - Absorptivity (*A*) with pdf $p\,(A) \sim \mathrm{U}\,(0.5, 0.9)$.
  - Delta for thermal conductivity of the substrate ($\delta_{k_{\mathrm{sub}}}$) with pdf $\delta_{k_{\mathrm{sub}}} \sim \mathrm{N}\,(0, 1)$.
  - Delta for thermal conductivity of the powder ($\delta_{k_{\mathrm{pow}}}$) with pdf $\delta_{k_{\mathrm{pow}}} \sim \mathrm{N}\,(0, 1)$.
  - Combined[5] delta for density of both substrate and powder (δ_{ρ}) with pdf $\delta_{\rho} \sim \mathrm{N}\,(0, 1)$.
- Outputs to the gPCE model
  - Melt pool width (*w*).
  - Melt pool depth (*d*).

[5]In this case, each property will follow its own function given by Equation (4.1), but the same δ_{ρ} will be used.

  - Peak temperature at the powder-substrate interface (T_p).
  - Maximum cooling rate at the powder-substrate interface (C).
  - Maximum spatial gradient (G).

Next, we initiate the gPCE framework by running the adaptive methodology. The following criteria was implemented for simulations on the SIERRA model:

- Simulation variables
  - Material system is Ti-6Al-4V for both substrate and powder.
  - Layer thickness is $30\,\mu\mathrm{m}$.
- Laser parameters
  - Laser power is set constant at $50\,\mathrm{W}$.
  - Scanning speed is set constant at $80\,{}^{\mathrm{mm}}\!/_{\mathrm{s}}$.
- Adaptive gPCE parameters
  - Each iteration adds 10 new datapoints to the dataset sampled from a scrambled Sobol's quasi-random uniform sequence generator [134].
  - Polynomial truncation degree is $t = 4$.
  - Cross validation metric is MAPE_k from Equation (A.11).
  - Error targets varies depending the subset of outputs selected, or the methodology finishes if convergence is achieved.

Three different gPCE models were trained based on different subsets of outputs:

1. $\mathrm{gPCE}_1 = \{G, C, d\}$
2. $\mathrm{gPCE}_2 = \{d, w\}$
3. $\mathrm{gPCE}_3 = \{T_p, C, d\}$

The objective for selecting these subsets is to assess how the selected QoIs behave and correlate with one another at different settings within the gPCE model. Specifically, model $gPCE_1$ includes melt pool dimensions (represented by depth), and derivatives of the simulated temperature field on space (i.e., spatial gradient *G*) and time (i.e., cooling rate *C*). On the other hand, $gPCE_2$ focuses on modeling UP based on melt pool dimensions solely, and is used as a benchmark for comparison with situations when more outputs besides melt pool dimensions are accounted to validate thermal models. The last case, $gPCE_3$, is similar to the first one with the only difference that spatial gradient is replaced by peak temperature.

The adaptive iterative methodology explained in Section 4.1 was applied to all three subsets of response outputs, with the results being shown on the three panes of Figure 4.7. These plots represent the path for CV error throughout the iterations for each gPCE model by showing the progression of the CV MAPE error calculated from Equation (A.11) for each QoI. It has to be reminded that as a new iteration was executed, more data was included into the model, hence the monotonic decreasing shape of the curves. Since each output response has its own scale and magnitudes, the results from Figure 4.7 are presented in percentage ratios with respect to the initial CV error at the first iteration.

It can be seen that for model $gPCE_1$in Figure 4.7a, the errors start to converge at iteration 5, however the magnitude of error for metric *C* is still relatively high. In terms of numerical values, melt pool depth errors converge to a value around $0.24\,\mu\mathrm{m}$, which is an extremely low error and thus acceptable given the size and magnitude of the melt pools within the real process (which, depending on laser beam sizes, are usually around or larger than $100\,\mu\mathrm{m}$). Therefore, in terms of CV error, the gPCE model would be validated given these results if the sole focus was directed on melt pool depth. Nevertheless, it can also be seen that error for cooling rate *C* converges to a value of $9200\,\mathrm{K/s}$ which is a significant large value that would restrict successful validation of the thermal model. Spatial gradient *G* converges to a relative low value of $27.8\,\mathrm{K/mm}$ but this result might be subjective in terms of the application of the thermal model. In other words, for phase field microstructure modeling applications, uncertainty of $27.8\,\mathrm{K}\cdot\mathrm{mm}$ in temperature across a

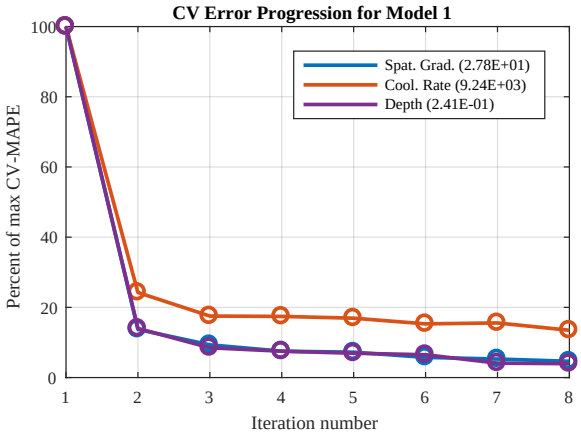

(a)

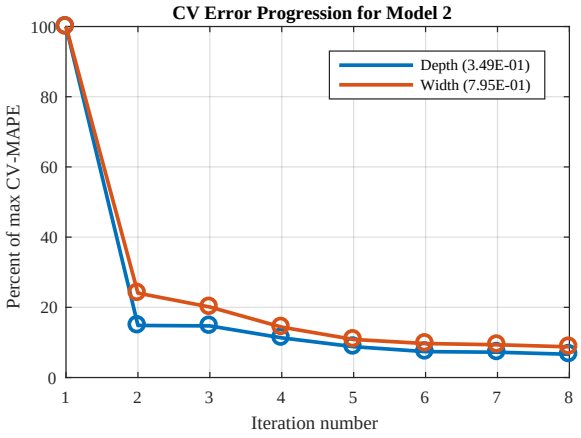

(b)

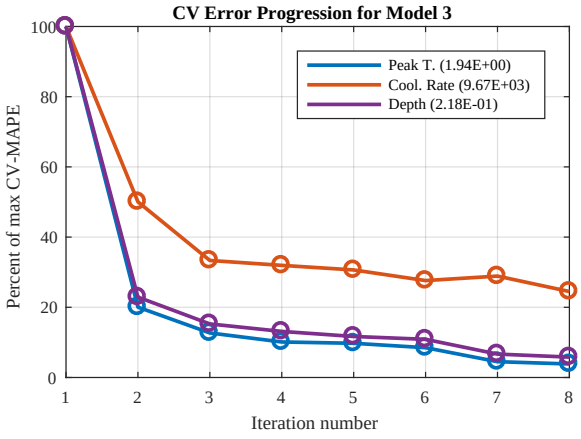

(c)

Figure 4.7: Results of the adaptive sparse multivariate gPCE methodology for three different combination of L-PBF metrics. The number in parenthesis represents the value of the CV error at the last iteration of the progression, with physical units being the ones presented on Page 59. **(a)** Maximum spatial gradient, cooling rate and melt pool depth. **(b)** Melt pool depth and width. **(c)** Peak temperature, cooling rate and melt pool depth.

small length of material would not acceptable since even a change in the magnitude of $1\,\mathrm{K}\cdot\mathrm{mm}$ is influential in planar and dendritic microstructure grow.

Regarding the second model gPCE_2, it can be seen in Figure 4.7b that both outputs behave almost similar, and numerically they converge to the values of $0.35\,\mu\mathrm{m}$ and $0.80\,\mu\mathrm{m}$ respectively for melt pool depth and width. The results of this model proves good understanding by the statistical model on these QoIs, and would most likely imply successful validation of the SIERRA model. The results for this second model ratify several conclusions observed on different works that validated L-PBF simulation models by only focusing on melt pool characteristics (see for instance [137–139]).

Lastly, results from model gPCE_3 in Figure 4.7c present very similar behavior among peak temperature T_p and melt pool depth that can be attributed to the fact that melt pool dimensions are estimated based on a comparison of temperatures with respect to the melting point for the material, and thus it is a metric derived from a direct measure of temperature (as opposed to cooling rates which are derivatives of the simulated temperature with respect of time). Numerically, peak temperature converges to $1.9\,\mathrm{K}$ in CV error which is very low value in the context of temperature for L-PBF, and thus relates to good performance of the model over this QoI. A similar behavior as with model 1 is seen by the remaining metrics: high error of $9600\,\mathrm{K/s}$ for cooling rate and an insignificant error of $0.20\,\mu\mathrm{m}$ for melt pool depth. Again, this confirms that melt pool dimensions should not be solely considered when validating or assessing thermal model results, but instead should be used along with other types of responses to account for all the physics and phenomena happening during the manufacturing process.

A second approach used to confirm the hypothesis that additional metrics other than melt pool dimensions must be employed when validating a L-PBF thermal model is to analyze the results for output probability distributions realized by propagating the uncertainty throughout the SIERRA model. In this case, Equations (3.17) and (3.18) are calculated for each of the three gPCE models discussed, and the statistical moments for each metric considered is presented in Table 4.3.

The results of UP for model 1 show that even though the predicted variability of melt pool

Table 4.3: Statistical moments for each model output calculated through multivariate gPCE.

Model	Metric	$\mathbb{E}[\mathtt{Y}_k]$	$\sqrt{\mathrm{var}[\mathtt{Y}_k]}$
gPCE_1	G [$^{\mathrm{K}}/_{\mathrm{mm}}$]	6.167×10^3	9.816×10^2
	C [$^{\mathrm{K}}/_{\mathrm{s}}$]	4.477×10^5	1.191×10^5
	d [µm]	105.874	13.339
gPCE_2	d [µm]	105.787	13.194
	w [µm]	232.027	25.454
gPCE_3	T_p [K]	3.891×10^3	275.736
	C [$^{\mathrm{K}}/_{\mathrm{s}}$]	4.475×10^5	1.191×10^5
	d [µm]	105.903	13.365

depth is particularly small (denoted by the standard deviation and calculated to be about $13\,\mu\mathrm{m}$), the respective results for spatial gradient and cooling rates are still high. This means that melt pool depth is not very sensitive to fluctuations introduced by the material properties (as opposed to thermal gradients and cooling rates), and therefore do not provide a complete notion of the thermal process within L-PBF.

A similar conclusion as in the previous paragraphs is obtained for model gPCE_2, where by exclusively accounting for melt pool dimensions, variability of these is almost negligible and thus wrongful interpretations of the model might happen. Results for model gPCE_3 yield the same conclusion in terms of melt pool depth (i.e., low variability) and cooling rate (i.e., significant variability), however peak temperature results are subjective to the application being employed for. One case where variability of $275\,\mathrm{K}$ may be acceptable is for experimental cases when a pyrometer sensor is used to measure melt pool temperatures. Variability for these devices, such as the one presented in Section 2.1.4, range from $100\,\mathrm{K}$ to $300\,\mathrm{K}$ given the different factors and difficulties that affect measurements through non-contact pyrometry.

Although melt pool characteristics are important components within L-PBF research that unquestionably need to be studied, characterized and understood, the multivariate UP framework has shown that these attributes tend not to vary drastically throughout the manufacturing process.

Therefore, research focused solely on them may provide some misinformed decisions and conclusions which do not resemble to the actual L-PBF process. Consequently, a beneficial and necessary step towards expanding L-PBF in industries with stringent quality requirements is to better understand and account for other different thermal metrics of the process during analysis and studies in order to be capable of drawing improved informed conclusions, that eventually will help to lead the path towards a necessary increase in repeatability of end parts which is one of the main drawbacks for L-PBF.

This chapter has presented several applications of Forward UQ into L-PBF problem. Different physics within the manufacturing process have been studied through the use of UP statistical models in order to characterize and quantify their uncertainty. In the next chapter, several different applications will be presented where Inverse UQ is employed to help analyze and solve those problems.

5. INVERSE UNCERTAINTY QUANTIFICATION*

In this chapter, different problems will be presented where the focus is to describe the behavior of a system within L-PBF through a fast and data-driven mathematical representation defined by a set of inputs and outputs, in order to rapidly and confidently gain knowledge of the system (a physical process or a computational model), and then take actions or draw respective conclusions.

The chapter will follow the next structure: Section 5.1 deals with the characterization and optimization of porosity in L-PBF printed parts based on fine tuning of the processing parameters. Next in Section 5.2, a data-driven approach will be taken to identify windows of L-PBF processing parameters that yield different conditions on the melt pool. This is done by creating surrogate models for experimentally collected data and for a high-fidelity L-PBF computer model.

The last two sections of the chapter will present a framework to statistically calibrate different computer models. Section 5.3 will describe a statistical calibration of a precipitation model used for SMAs compatible and widely used in L-PBF manufacturing. Next, Section 5.4 extends the methodology into a generalized multivariate statistical calibration and applies this framework to calibrate a L-PBF FEM thermal model.

5.1 Prediction of Porosity in End Parts

As explained in Section 2.1.1, one of the most common defects identified in L-PBF processes is porosity. Presence of pores in end-parts compromises mechanical properties and performance of the part, since heavy concentration of them may reduce tensile strength, ductility and fatigue properties. There have been identified multiple mechanisms that contribute to the creation of pores

*Parts of this section have been reprinted with permission from G. Tapia, A. Elwany, and H. Sang, "Prediction of porosity in metal-based additive manufacturing using spatial gaussian process models," *Additive Manufacturing*, vol. 12, pp. 282–290, 2016. Copyright © 2016 by Elsevier B.V., and with permission from G. Tapia, S. Khairallah, M. Matthews, W. E. King, and A. Elwany, "Gaussian process-based surrogate modeling framework for process planning in laser powder-bed fusion additive manufacturing of 316L stainless steel," *The International Journal of Advanced Manufacturing Technology*, vol. 94, no. 9, pp. 3591–3603, 2018. Copyright © 2017 by Springer-Verlag London Ltd., and with permission from G. Tapia, L. Johnson, B. Franco, K. Karayagiz, J. Ma, R. Arroyave, I. Karaman, and A. Elwany, "Bayesian calibration and uncertainty quantification for a physics-based precipitation model of nickel–titanium shape-memory alloys," *Journal of Manufacturing Science and Engineering*, vol. 139, no. 7, p. 071002, 2017. Copyright © 2017 by ASME.

Table 5.1: Chemical composition of 17-4 PH stainless steel powder produced by 3D Systems Inc. Reprinted with permission from [42]

Element	Fe	Cr	Ni	HC Cu
Concentration [%]	70-80	10-25	1.0-10	1.0-10

within L-PBF parts structure like shrinkage, gas entrapment, recoil vapor pressure, adhesion of partially molten particles to surfaces between layers, inadequate powder layering, and balling [11, 84].

It has been shown that selection of different L-PBF processing parameters has an impact in part porosity [21] (specially laser power, scanning speed, hatch distance and layer thickness), consequently, it is of paramount importance that porosity is eliminated, or at least minimized, from L-PBF end parts through proper tuning of these parameters.

In order to accomplish this task, GP techniques are employed due to the complexity and intricacies of the physics of pore formation that refrain us from using a physics-based approach. Therefore, the starting step to use the GP methodology presented in Section 3.3.1 is to collect the dataset that the statistical model will be trained on. Experimental work was carried out using the 3D Systems ProX 100 DMP L-PBF system introduced in Section 3.4, and cubic samples of size $10 \times 10 \times 10\,\mathrm{mm}^3$ were printed with 17-4 PH stainless steel produced also 3D Systems Inc. Some of these samples are shown in Figure 5.1a, and additionally, the chemical composition of this material is presented in Table 5.1.

This problem was specifically focused on the effects of laser power (P) and scanning speed (v) on the porosity of the parts, therefore $q = 2$. The domain of interest $\mathcal{X}$ was devised with the following configuration:

- Laser power: $P = 40\,\mathrm{W}$ to $50\,\mathrm{W}$.
- Laser scanning speed: $v = 0.275\,\mathrm{m/s}$ to $0.4\,\mathrm{m/s}$.

These ranges where selected based on several points: the limitations of the L-PBF system to

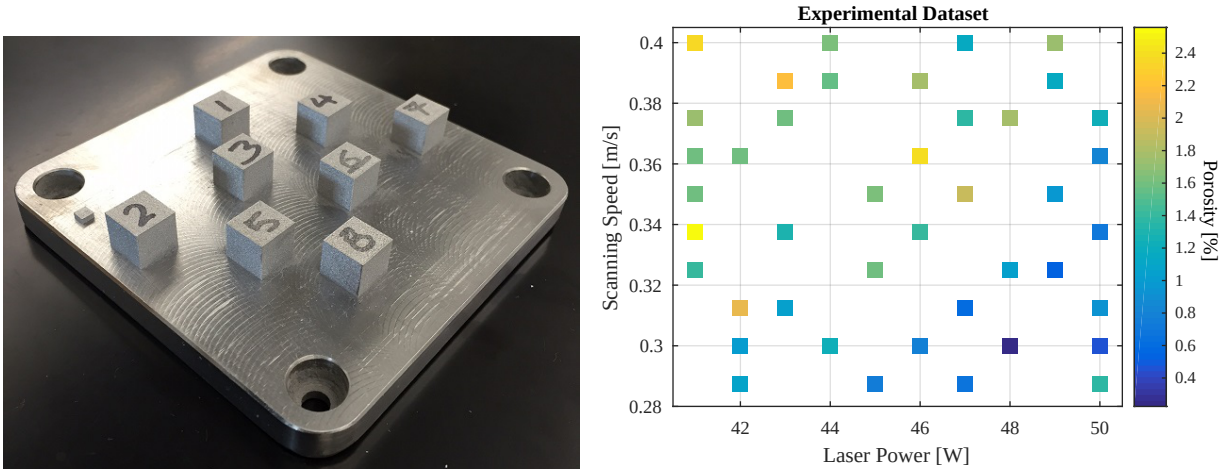

(a) **(b)**

Figure 5.1: Printed samples made of 17-4 PH stainless steel for porosity optimization. **(a)** As-built coupons. Reprinted with permission from [42]. **(b)** Spatial behavior of the observations across the *P*-*v* space. Reprinted with permission from [42].

a maximum power of $50\,\mathrm{W}$, inclusion of OEM default values into the study region, and to ensure bonding between layers of samples by avoiding extremely low powers or very fast speeds. Thus, 42 test samples were initially printed at different combinations of power and speed, which are visually represented in Figure 5.1b. The first 30 points were chosen following a *Latin Hypercube Sampling* (LHS) design, while the last 12 were manually chosen to fill in the blank spaces within the *P*-*v* space.

After the samples were produced, the porosity (as well as the density) of each test part was measured using the Archimedes' principle according to ASTM B962 standard [141]. It is important to note that this method is sensitive to some factors such as precision of the balance, buoyancy of air, the relation between density and temperature of the liquid, surface tension of the liquid and presence of bubbles. To account for these factors in the study, a balance with $\pm 0.0001\,\mathrm{g}$ tolerance was used. Samples were put under vacuum to ensure no air bubbles are present when taking measurements and a correction factor was used for the volume of the float.

Following the formulation from Section 3.3.1, the mean function is defined as a second order

linear regression with interactions and an intercept,

$$\mu(\mathbf{x}) = \beta_0 + \beta_1 x_1 + \beta_2 x_2 + \beta_3 x_1 x_2 + \beta_4 x_1^2 + \beta_5 x_2^2$$

where x_1 denotes the power *P* covariate, x_2 is the speed *v* covariate, and $\boldsymbol{\beta} = \{\beta_0, \ldots, \beta_5\}$ are regression coefficients. Nevertheless, after preliminary testing, it was decided the mean function should only account for first order terms since other parameters were almost canceled on initial testing. Hence, the mean function was taken as

$$\mu(\mathbf{x}) = \beta_0 + \beta_1 x_1 + \beta_2 x_2 \tag{5.1}$$

A challenge was encountered for the covariance function, since most of these functions have been developed in the literature on geostatistics and for applications in geographical spaces [103]. In this study, one of the most popular covariance functions in the literature named *Matern* covariance function is used with a re-parameterization on the similarity metric between two points on the input space (as opposed to traditional Euclidean distance used for geostatistics). Therefore, the following formulation was used

$$C(\mathbf{x}_i, \mathbf{x}_j) = \sigma^2 \frac{Q^\nu \mathcal{K}_\nu(Q)}{\Gamma(\nu) 2^{\nu-1}} \tag{5.2}$$

where σ^2 represents the variance of the process, ν is the smoothness parameter of the function, $\mathcal{K}_\nu(\cdot)$ is the modified Bessel function of second kind of order ν, $\Gamma(\cdot)$ is the gamma function, and *Q* represent mentioned reparameterized similarity metric between points $\mathbf{x}_i, \mathbf{x}_j$, which follows next equation:

$$Q = \sqrt{\sum_{k=1}^{q} \left(\frac{x_{i,k} - x_{j,k}}{\lambda_k} \right)^2} \tag{5.3}$$

where $x_{i,k}$ represents the *k*th component of input $\mathbf{x}_i$, and λ_k are length-scale parameters modeling the strength of spatial dimension-wise correlation in the input space.

Lastly, an error term is accounted within the framework given the stochasticity of experimental measurements of porosity. This error term is defined to be i.i.d. Normal distributed with zero mean and variance τ^2,

$$\epsilon\left(\mathbf{x}\right) \sim \mathrm{N}\left(0, \tau^2\right) \tag{5.4}$$

With these choices, the GP model from Equation (3.26) is completely defined with hyperparameter set $\boldsymbol{\Omega} = \{\boldsymbol{\beta}, \sigma^2, \lambda_1, \lambda_2, \tau^2\}$ where $\boldsymbol{\beta} = \{\beta_0, \beta_1, \beta_2\}$. Note that the smoothness parameter for the Matern function is set constant at $\nu = \frac{1}{2}$. Thus, after collection of datasets $\mathbb{X}, \mathbb{Y}$ as defined in Equation (3.3), the likelihood function is equal to

$$p\left(\mathbb{Y}|\mathbb{X}, \boldsymbol{\Omega}\right) \sim \mathrm{N}_n\left(\boldsymbol{\mu}, \boldsymbol{\Sigma}\right) \tag{5.5}$$

with

$$\begin{aligned}
\boldsymbol{\mu} &= \mu\left(\mathbb{X}\right) \\
\boldsymbol{\Sigma} &= C\left(\mathbb{X}, \mathbb{X}\right) + \tau^2 \mathbf{I}_n
\end{aligned}$$

where $\mathbf{I}_n$ denotes an identity matrix of size $n \times n$.

Consequently, the model is fitted by MCMC – specifically employing Metropolis-Hastings and Gibbs sampler – with the following prior selections:

$$\begin{aligned}
p\left(\lambda_1\right) &\sim \mathrm{U}\left(0, 10\right) \\
p\left(\lambda_2\right) &\sim \mathrm{U}\left(0, 125\right) \\
p\left(\boldsymbol{\beta}\right) &\sim \mathrm{N}_3\left(\mathbf{0}, 10^4 \mathbf{I}_3\right) \\
p\left(\sigma^2\right) &\sim \mathrm{IG}\left(2, 1\right) \\
p\left(\tau^2\right) &\sim \mathrm{IG}\left(2, 0.2\right)
\end{aligned}$$

where $\mathbf{I}_3$ is the identity matrix of size 3×3. The reader should refer to Appendix A.1 for notation

and parameterizations of the different pdfs used.

These prior distributions are non-informative since there exists no prior knowledge about the hyperparameters. The inverse gamma distributions with shape parameter set equal to 2 corresponds to an infinite variance distribution. Furthermore, they are conjugate priors for the Gaussian model from Equation (3.27), and thus, it lets the data speak for itself. In a similar fashion, non-informative priors are assigned to $\boldsymbol{\beta}$, with a large-variance multivariate distribution, and flat uniform distributions to λ_i parameters between values based on the selected range for each process parameter (laser power and scan speed).

The MCMC algorithm was executed for 50,000 iterations with a burn-in period equal to 25% of them. Once the estimation process finished, predictions were calculated over the input domain following Equations (3.29) and (3.30). Figure 5.2a shows the prediction calculated by the GP model for the domain of study, while Figure 5.2b presents the predictive standard error for the GP predictions. This predictive standard error is calculated by taking the square root of Equation (3.30). The white dots represent the original observed data points, and demonstrate consistency of the predictive methodology since the error is expected to be small in locations that are closer to the observed data and larger at unobserved locations.

Nevertheless, since there are some locations within Figure 5.2b that still present relatively high predictive standard error, the model is improved by adding new observations at several locations within the input space. These new observations were appended to the original data set, therefore the new dataset size was increased to 82 data points. The final number of observations was based on the number of regions with high predictive standard error, empty regions with almost no observations, the range of the experiment space and the capabilities of the manufacturing system. These are presented in Figure 5.3.

The complete framework was reapplied to the new increased dataset, and results are presented in Figures 5.4a and 5.4b. It is worth to note that both figures are shown at the same color scale, such that it is easier to assess that new observations significantly reduced the predictive standard error. It can also be seen that the prediction results are physical and consistent with the familiar

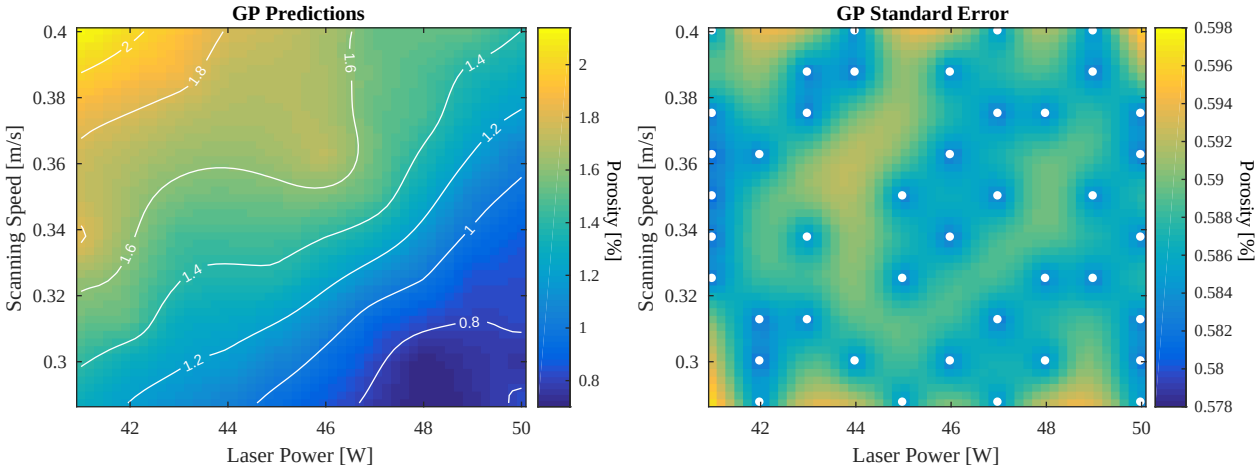

(a) (b)

Figure 5.2: GP model trained with porosity data from L-PBF parts. **(a)** Predictions of porosity at the domain of study. Reprinted with permission from [42]. **(b)** Predictive standard error for GP predictions. White dots denote the position of the training points. Reprinted with permission from [42].

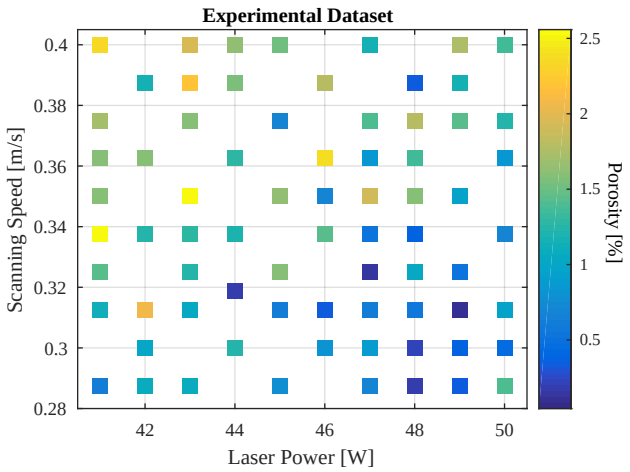

Figure 5.3: Increased experimental dataset of porosity measurements. Reprinted with permission from [42].

expression for *energy density* in L-PBF [37, 78] given by

$$E = \frac{P}{v \times h_d \times t_d} \tag{5.6}$$

since less porosity is expected when more energy is deposited into the material as laser power increases and scanning speed decreases. This is corroborated by the results shown in the bottom right region of the colormap from Figure 5.4a. On the other hand, as laser power decreases and scanning speed increases, less energy will be transferred into the powder material, and hence porosity is more prone to be present within parts. Similarly, this is confirmed in the plot on the top left side.

Performance of the GP model is visually presented in Figure 5.4c and numerically measured through LOO CV and MAPE, with the resulting value equal to $\mathrm{MAPE} = 0.3892$ in porosity percentage. The calculated MAPE is a relatively low value for the generalizing error in the model, being about 20% of the range of the original observations. This means that the model does capture the process from the dataset and is able to explain and generalize it to untrained datapoints.

This GP methodology has shown a data-driven predictive approach for very intricate phenomena within L-PBF processes. This type of modeling is very useful as it increases the understanding of the process, and it is beneficial towards the end goal of stringent quality and performance control within several industries (such as aerospace, automotive, healthcare). In the next section, a further study is presented where GP models along with high-fidelity computationally-expensive physics-based simulation models are employed to provide means for optimizing the L-PBF process through identification of windows of optimal processing parameters.

5.2 Processing Windows based on Melt Pool Characteristics

It has been repeatedly mentioned throughout the dissertation that L-PBF processes involve several physical phenomena during the manufacturing process, which make it prone to many defects and flaws in parts. Due to these complexities, the majority of recent road-mapping efforts have strongly emphasized the need for developing modeling and simulation tools to foster our understanding of the process and ultimately serve as predictive frameworks to optimize the process and

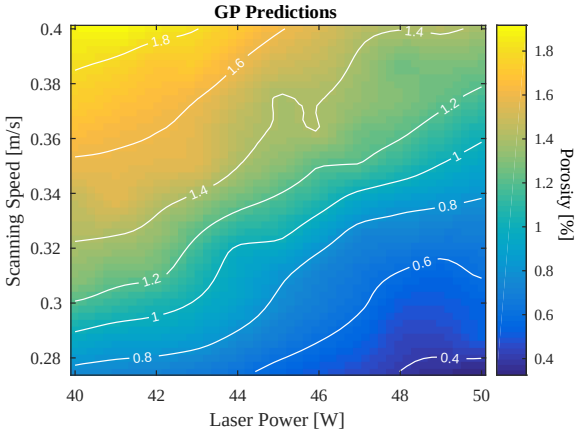

(a)

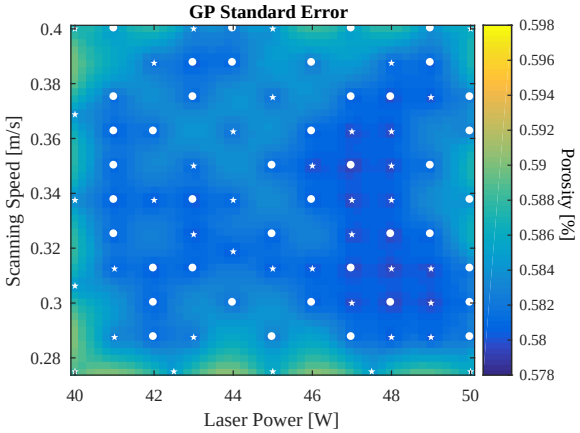

(b)

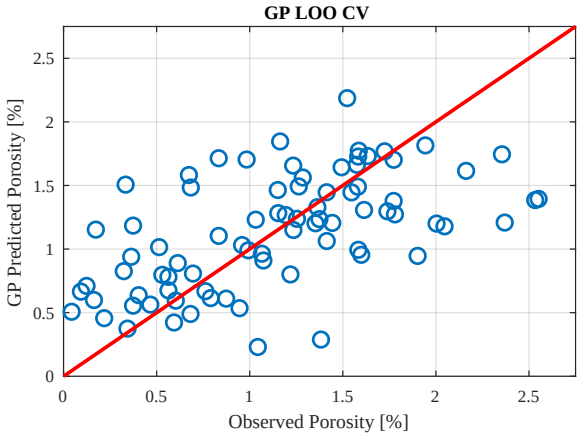

(c)

Figure 5.4: Improved GP model trained with porosity data from L-PBF parts. **(a)** Predictions of porosity at the domain of study. Reprinted with permission from [42]. **(b)** Predictive standard error for GP predictions. White dots denote the position of the initial training points, while white stars denote the new training points. Reprinted with permission from [42]. **(c)** Comparison of observed versus predicted values of porosity via LOO CV. Reprinted with permission from [42].

mitigate defects [16, 17, 142]. As explained in Section 2.1.3, many research groups have devoted resources and focused on modeling and predictive simulation for L-PBF processes. Although these models are still invaluable for understanding the physics of the process, their direct use in process optimization is impractical and sometimes unfeasible in terms of the burden associated with running simulations.

In L-PBF, the melt pool is an important region for analysis and evaluation of the process, since it provides an idea of how well powder particles are bonding together within the same layer and to previous layers. Identification and analysis of melt pool characteristics help to generalize the expected quality and performance of the part when it is completely printed. In this section, the task is to identify windows of desired L-PBF processing such that defects in the part are avoided. Specifically, the objective is to identify and prevent processing regions that yield keyhole mode melting, since this mode is undesirable in L-PBF because it involves evaporation of the material and results in deeper melt pool depths and trails of voids.

Optimal selection of processing parameters like laser power (P), scanning speed (v), and beam size ($D4$) is needed to avoid keyhole mode regimes, which in turn prevents pore defects in fabricated parts. Therefore, in order to be able to select the values for processing parameters, a GP framework will be used as surrogate model to gain knowledge and understanding of the L-PBF process by applying it to both a high-fidelity L-PBF simulation model and experimental data.

5.2.1 Surrogate Modeling of a High-Fidelity Simulation Model

Surrogate modeling is an effective tool for providing a computationally efficient and accurate approximation of computer simulation models with high computational burden. Thus, in order to solve this challenge for L-PBF computer models, a GP-based surrogate model will be constructed for a high-fidelity simulation model developed by Khairallah et al. [72] at Lawrence Livermore National Laboratory that studies the physics of complex melt flow in L-PBF processes. This computer model will be called the *LLNL model* hereafter.

The first step towards building a GP-based surrogate model was to collect a dataset. In this case, $n = 26$ simulations were executed on the LLNL model, each one at a different values for

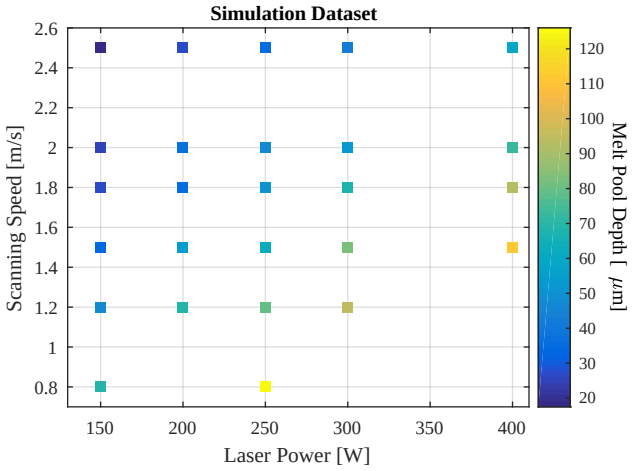

Figure 5.5: Melt pool depth data collected from simulations of a high-fidelity L-PBF model. Reprinted with permission from [19].

laser power *P* and scanning speed *v*, constant laser beam size $D4 = 52\,\mu\text{m}$ and layer thickness of $50\,\mu\text{m}$, and with stainless steel 316L as material system. The selected metric of study is melt pool depth and the complete simulation dataset is graphically depicted in Figure 5.5.

A response surface is fitted to this dataset following the same formulations and principles from Section 3.3.1, however an improved approach on the parameterizations of the covariance function is taken based on previous literature results by Higdon et al. [102, 143]. The inputs to the model are laser power *P* and scanning speed *v* (hence, $q = 2$) while the output of the model corresponds to the simulated melt pool depth (hence, univariate case).

First of all, the elements of input matrix $\mathbb{X}$ are normalized to the unit hypercube $[0, 1]^q$ such that all covariates are in the same orders of magnitude. This is beneficial when inputs of a model possess different physical units at different magnitudes. Specifically, this is the case in this problem since one of the covariates is laser power which ranges between $150\,\text{W}$ to $400\,\text{W}$, while scanning speed ranges from $0.8\,\text{m/s}$ to $2.5\,\text{m/s}$, and these encompass and define the input domain $\mathcal{X}$.

The elements of response vector $\mathbb{Y}$ are standardized to have a vector with mean 0 and variance 1. This step provides mathematical convenience related to subsequent estimation of hyperparameters [102]. In particular, with this step the statistical model is simplified by the specification of a

constant mean function:

$$\mu\left(\mathbf{x}\right) = 0 \tag{5.7}$$

The covariance function selected for this problem is a re-parametrization of the power exponential covariance function given by

$$C\left(\mathbf{x}_i, \mathbf{x}_j\right) = \frac{1}{\lambda} \prod_{k=1}^{q} \delta_k^{4\left(x_{i,k} - x_{j,k}\right)^2} \tag{5.8}$$

where λ is the *precision* (or inverse of the variance) of the process, $\boldsymbol{\delta} = \{\delta_1, \ldots, \delta_q\}$ is a set of parameters that control the strength or relevance of each input, and $x_{i,k}$ represents the *k*th component of input $\mathbf{x}_i$.

In this case, a measurement error term is not accounted for within the statistical model since the data comes from a deterministic computer model, and hence $\epsilon\left(\mathbf{x}\right)$ is not included in Equation (3.26). Consequently, the GP model from Equation (3.26) is completely defined with hyperparameter set $\boldsymbol{\Omega} = \{\lambda, \boldsymbol{\delta}\}$. Thus, after collection of datasets $\mathbb{X}, \mathbb{Y}$ as defined in Equation (3.3), the likelihood function is equal to

$$p\left(\mathbb{Y}|\mathbb{X}, \boldsymbol{\Omega}\right) \sim \mathrm{N}_n\left(\boldsymbol{\mu}, \mathbf{C}\right) \tag{5.9}$$

where $\boldsymbol{\mu} = \mu\left(\mathbb{X}\right)$ and $\mathbf{C} = C\left(\mathbb{X}, \mathbb{X}\right)$.

Since a Bayesian approach is taken, the following prior selections are defined:

$$p\left(\lambda\right) \sim \mathrm{Gamma}\left(5, 5\right)$$

$$p\left(\delta_i\right) \sim \mathrm{Beta}\left(1, 0.1\right)$$

and these choices present some features that improve the estimation process. First, the gamma family of distributions is conjugate to the normal family in the likelihood function in Equation (3.27) which provides computational advantages [103]. Second, the variance of the process is expected to be close to 1 due to standardization of vector $\mathbb{Y}$, hence the prior $p\left(\lambda\right) \sim \mathrm{Gamma}\left(5, 5\right)$ probability distribution gives more probability weight to values close to $\lambda = 1$.

Furthermore, the covariance function in Equation (5.8) provides further information beyond spatial dependence. In particular, if the *i*th covariate has no influence on output *Y*, then parameter δ_i should be estimated to be equal to 1. Thus, under this parameterization, an extra step is added that identifies inputs that really influence the process and those that do not (i.e., active versus inactive inputs). For these reasons, a $\mathrm{Beta}\,(1, 0.1)$ is set for the prior distributions of δ_i such that there is substantial prior mass near 1 [102].

The posterior distribution of the model parameters are estimated using the Metropolis-Hastings MCMC algorithm (see Appendix B) with 25,000 iterations, burn-in period of 40%, and thinning every 5th iteration. Specifically, an *adaptive* Metropolis-Hastings algorithm is used by improving its capability of tuning up the parameters of the proposal distribution in order to improve mixing, exploration of the parameters space, and convergence of the chain. After obtaining the posterior distribution, predictions were made over the whole range of the L-PBF processing parameters space $\mathcal{X}$, and the standard predictive error was also calculated. Both results are depicted in Figures 5.6a and 5.6b.

As a final step to ensure the model is able to understand and generalize over unseen datapoints, a 10-fold CV was calculated and is visually shown in Figure 5.6c. The results show good performance of the model both visually and numerically with $\mathrm{MAPE}_{\mathrm{sim}} = 6.91\,\mu\mathrm{m}$, hence this surrogate model can be subsequently employed to make quick predictions, within a degree of confidence, for process optimization purposes. This is an important step forward since it would take only microseconds to make predictions using the GP model as opposed to up to several hours (or days) using the high-fidelity LLNL model even using high performance computing facilities.

Now that this framework has been proved successful when applied to computational simulations, it is still of paramount importance to analyze its performance on experimental data, and thus, this will be presented in the next subsection.

5.2.2 Surrogate Modeling of Experimental Data

This subsection presents an approach employing experimental data coming in from previous studies as well as additional experiments collected, in order to construct a GP-based surrogate

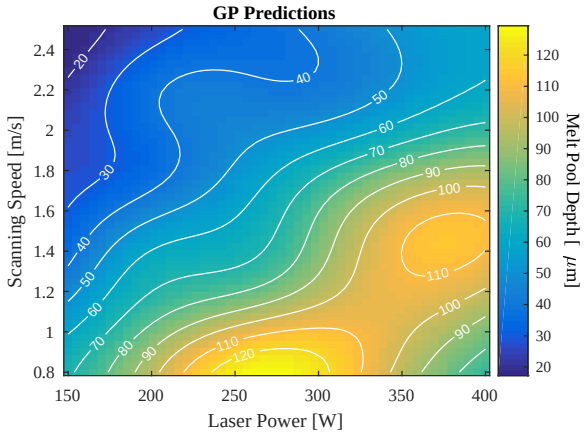

(a)

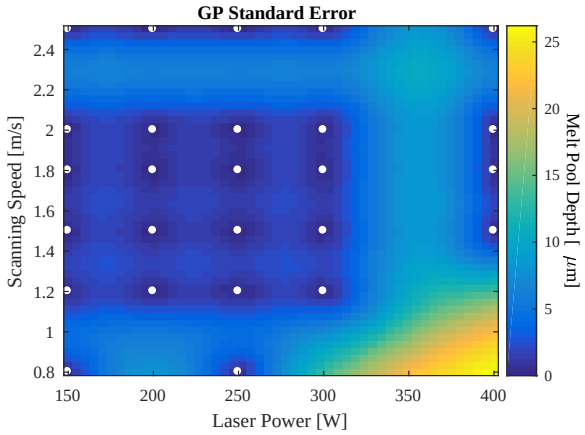

(b)

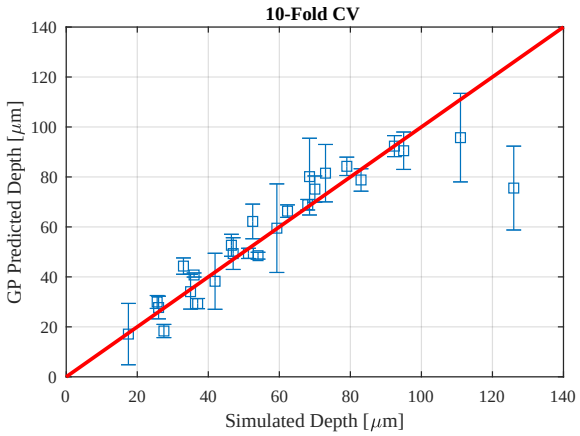

(c)

Figure 5.6: GP model trained with melt pool depth simulations from the LLNL model. **(a)** Predictions of melt pool depths at the domain of study. **(b)** Predictive standard error for GP predictions. White points denote the position of the training points. **(c)** Comparison of simulated versus predicted values of melt pool depth via 10-fold CV. Reprinted with permission from [19].

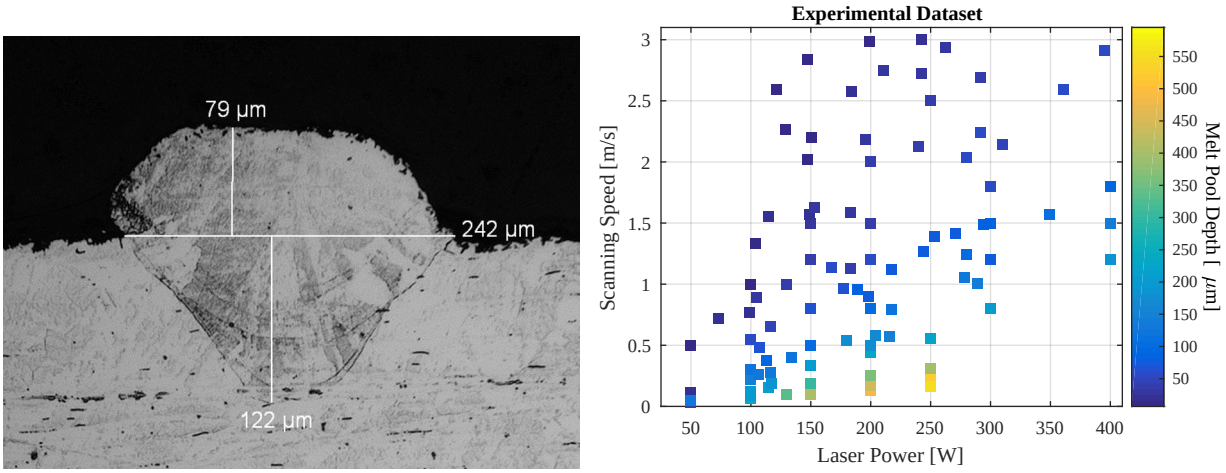

(a) **(b)**

Figure 5.7: Experimental measurements of L-PBF melt pool depth. **(a)** Optical micrograph and characterization of a single track experiment. Reprinted with permission from [19]. **(b)** Spatial behavior of the melt pool depth observations across the *P*-*v* space. Reprinted with permission from [19].

model for quantifying uncertainty and building knowledge from the L-PBF process. The experiments come from single-track runs of stainless steel 316L built under different process parameter settings with a commercial Concept Laser M2 system.

For experimental characterization of melt pool, each of the single tracks is sectioned, polished, etched, and examined under an optical microscope to measure melt pool depths and widths, as shown in the sample micrograph in Figure 5.7a.

Melt pool depth data was also gathered from previous studies by King et al. [36], Kamath [125], which brought the total count of experimental measurements to $n = 139$ measurements over a wide range of values for laser power P and scanning speed v, at constant laser beam size $D4 = 52\,\mu\text{m}$ and layer thickness of $50\,\mu\text{m}$. These measurements are described in Table 5.2 and displayed in the 2D colormap on Figure 5.7b, where each colored datapoint represents an experiment produced at a specific combination of laser power and scanning speed.

Since some of these experiments were replicated at the same combination of parameter values, a pre-processing step on the data is carried out to homogenize and sort out differences and outliers

Table 5.2: Summary of the different experimental dataset for L-PBF melt pool depths.

Source	n	n_{unique}	$P_{\min}$	$P_{\max}$	$v_{\min}$	$v_{\max}$	$D4$	t_d
[36]	52	52	73	395	0.15	3.0	52	50
[125]	14	14	150	400	0.50	1.8	54	50
Measured	73	31	50	250	0.03	2.5	52	50

n: the number of data points in the dataset; n_{unique}: the number of unique combinations of laser power and speed in the set; *P:* laser power in W; *v:* scanning speed in $^{\text{m}}/_{\text{s}}$; $D4$: size in μm of the laser beam with a Gaussian profile specified at 4 times its standard deviation; t_d: the layer thickness in μm.

that occur when combining datasets from different sources. Thus, each data point in the aggregated dataset was analyzed individually to remove obvious outliers. A point is flagged as outlier if the melt pool depth does not decrease with increasing scanning speed for a given constant laser power and beam size (denoted as *Filter 1*). Furthermore, within the same replication points are flagged if they lie outside a symmetric 10% range centered around the mean melt pool depth of that replication (denoted as *Filter 2*). It is important to point out that since the collective data for this study is compiled from different studies, it was not feasible to revisit and examine the physical samples in order to identify the root cause of these anomalies. Hence, these ad hoc filters were devised based on domain knowledge of the process and expert judgment.

More specifically, Filters 1 and 2 imply that melt pool depth should decrease as scanning speed is increased at a fixed power setting, given the fact that less energy is being input into the powder. It remains true however that upon the availability of the physical samples, the reason for these anomalies and outliers should be carefully studied and identified. The results after implementing these two filters are visually depicted in Figure 5.8a.

A subsequent pre-processing step is to consider experimental data points with close values of L-PBF processing parameters, which translates to those points that are within a circle with a pre-specified threshold radius in the *P*-*v* parameter space. It is expected that these points have very similar melt pool depths, or otherwise this flags an anomaly. To implement this filter, the *P*-*v* axes are scaled down to the unit hypercube, and those points that are located within a 0.01-radius

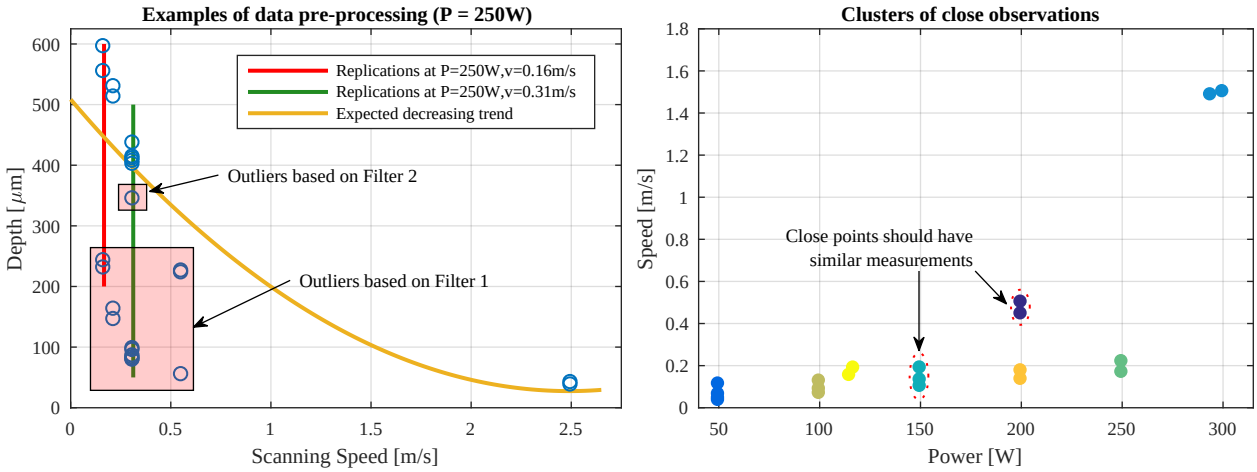

Figure 5.8: Pre-processing step for the aggregated experimental dataset of melt pool depth measurements. **(a)** Graphical description of Filter 1 and Filter 2 at constant laser power $P = 250\,\mathrm{W}$. Reprinted with permission from [19]. **(b)** Clustering of points for close combinations of processing parameters based on k-means algorithm. Different colors correspond to separate clusters. Reprinted with permission from [19].

circle from one another are flagged. This area corresponds approximately to $7\,\mathrm{W}$ and $0.06\,\mathrm{m/s}$. The flagged data points are then clustered using a *k-means* unsupervised learning algorithm (see Figure 5.8b), and finally after determining these clusters, if the standard deviation of the points within a cluster is relatively low compared to its mean, then no change is needed. Otherwise: (1) if the cluster contains only two data points, the whole cluster is discarded, or (2) if the cluster contains more than two data points, we iteratively identify and remove outliers following the same procedure previously explained for the replication case until low standard deviation is obtained or the whole cluster is discarded.

After the pre-processing step has been executed, the final number of datapoints in the dataset came down to $n = 96$. Next, a GP model is fitted following the formulations from Section 3.3.1 with a similar approach to the previous subsection. Specifically, inputs variables are laser power and scanning speed and response QoI is melt pool depth (hence, $q = 2$ and univariate GP).

Similarly as the previous case, elements of input matrix $\mathbb{X}$ are normalized to the unit hypercube $[0, 1]^q$ such that all covariates are in the same orders of magnitude, while elements of response

vector $\mathbb{Y}$ are standardized to zero mean and variance 1. With this step, we again specify a constant zero mean function and power exponential covariance function given by Equations (5.7) and (5.8) respectively.

Nevertheless, as opposed to the previous case, a measurement error term $\epsilon(\mathbf{x})$ is now included since the data will present some inherent measurement noise. This term is defined to be i.i.d. for every experimental datapoint, with the following distribution

$$\epsilon(\mathbf{x}) \sim \mathrm{N}\left(0, \frac{1}{\tau}\right) \tag{5.10}$$

where τ is precision of the distribution. Consequently, the GP model from Equation (3.26) is completely defined with hyperparameter set $\mathbf{\Omega} = \{\lambda, \boldsymbol{\delta}, \tau\}$.

Thus, again after proper collection of datasets $\mathbb{X}, \mathbb{Y}$ as defined in Equation (3.3), the likelihood function for this case is equal to

$$p(\mathbb{Y}|\mathbb{X}, \mathbf{\Omega}) \sim \mathrm{N}_n(\boldsymbol{\mu}, \mathbf{\Sigma}) \tag{5.11}$$

where

$$\begin{aligned}\boldsymbol{\mu} &= \mu(\mathbb{X}) \\ \mathbf{\Sigma} &= C(\mathbb{X}, \mathbb{X}) + \frac{1}{\tau}\mathbf{I}_n\end{aligned}$$

and the following the following prior selections are defined towards Bayesian estimation:

$$\begin{aligned}p(\lambda) &\sim \mathrm{Gamma}(5, 5) \\ p(\delta_i) &\sim \mathrm{Beta}(1, 0.1) \\ p(\tau) &\sim \mathrm{Gamma}(1, 0.0001)\end{aligned}$$

These choices of prior distributions are exactly the same as for the computer model surro-

gate model approach, with the addition of the prior distribution for precision τ, which is a non-informative choice of distribution giving more probability weight to large values, equivalent to modeling low noise. An adaptive Metropolis-Hastings MCMC algorithm was again executed with 25,000 iterations, burn-in period of 40%, and thinning every 5th iteration, and predictions were made over the whole range of the L-PBF processing parameters space, as well as the standard predictive error. Both results are depicted in Figures 5.9a and 5.9b.

To ensure the model is able to understand and generalize over unseen experimental data, 10-fold CV was calculated and is visually shown in Figure 5.9c. The results show good performance of the model both visually and numerically, $\mathrm{MAPE}_{\mathrm{exp}} = 10.91\,\mu\mathrm{m}$, and thus this surrogate model can be subsequently employed to make quick predictions, within a degree of confidence, for process optimization purposes based on real experimental data. This is an important step forward since it reduces the requirements for large testing by trial-and-error techniques which simultaneously produces savings in costs and time resources.

As a last step, the GP-based surrogate model trained with the LLNL model is combined with the experimental observations to assess its performance on real L-PBF experiments. In other words, the surrogate model constructed in the previous subsection is now validated against the pre-processed experimental observations from this section, to quantify the agreement between its predictions and the real process. This step is important since the surrogate model is to be used in lieu of the high-fidelity simulation model.

Figure 5.10 shows the results of this assessment where the abscissa is the experimental measurement and the ordinate is the GP surrogate model prediction at the corresponding combination of L-PBF processing parameters. It should be noted that predictions were only calculated for experimental datapoints that lie within the bounds of domain of the simulations, in order to avoid extrapolation error as a misleading indicator of inadequate performance. Numerically, the computed $\mathrm{MAPE}_{\mathrm{sim,exp}} = 9.35\,\mu\mathrm{m}$ confirming that the simulations surrogate model is able to adequately capture and generalize the L-PBF process, with the need of only a few high-fidelity simulations.

Since all these surrogate models have successfully demonstrated good performance, they are

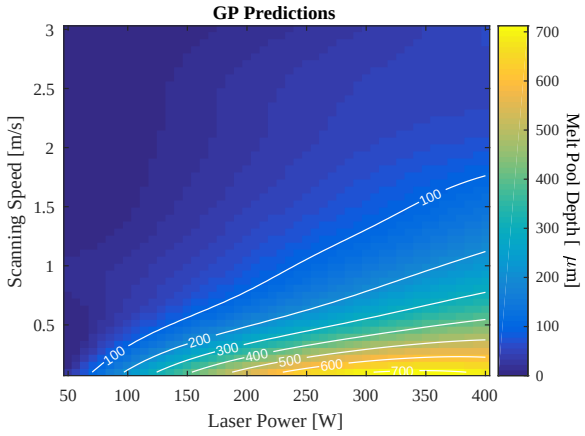

(a)

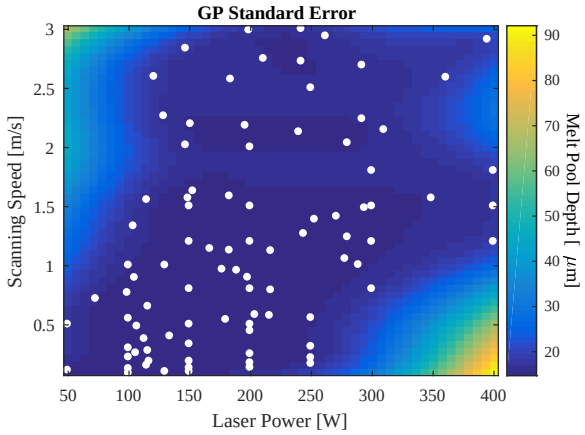

(b)

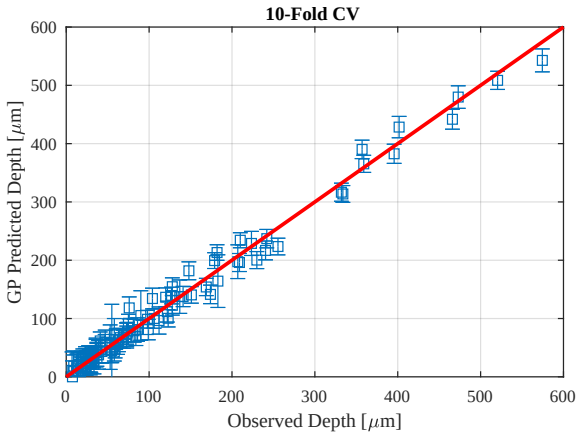

(c)

Figure 5.9: GP model trained with melt pool depth data from single track experiments. **(a)** Predictions of melt pool depths at the domain of study. **(b)** Predictive standard error for GP predictions. White points denote the position of the training points. **(c)** Comparison of observed versus predicted values of melt pool depth via 10-fold CV. Reprinted with permission from [19].

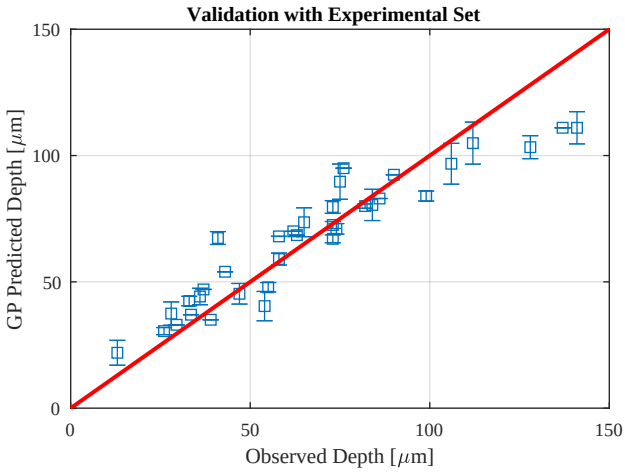

Figure 5.10: Validation of the GP surrogate model framework. Reprinted with permission from [19].

employed on the task of identifying optimal windows (or regions) for processing parameters within which keyhole laser melting or thermal conduction modes occur.

5.2.3 Identification of Processing Windows

Since one of the main objectives of the dissertation is to reduce the uncertainty in the L-PBF process, the tools constructed presented in this section are employed to identify windows of processing parameters where desired melting modes occur. Based on the works by King et al. [36, 77], the depth of the molten pool is controlled by conduction of heat into the underlying solid material and vapor recoil pressure that creates a small depression. However, under high energy deposition, the mechanism of melting changes from conduction to keyhole laser melting, and in this mode, the depth of the molten pool is controlled by evaporation of the metal and higher vapor recoil pressures. Keyhole mode laser melting results in melt pool depths that can be much deeper than observed in conduction mode, and thus, it is desired to avoid deep keyhole mode during L-PBF fabrication in order to build parts with good quality.

There are two different criteria to identify keyhole mode in L-PBF [36]:

- When normalized enthalpy is greater than or equal to 30, $\frac{\Delta H}{h_s} \geq 30$.
- When melt pool depth is equal or larger than half of the melt pool width, $d \geq \frac{w}{2}$ or $\frac{2d}{w} \geq 1$.

For the first bullet, the expression follows from a physics-based analysis derived from the following equation

$$\frac{\Delta H}{h_s} = \frac{AP}{\rho h_{s_m} \sqrt{\pi T_D v \left(\frac{D4}{4}\right)^3}} \tag{5.12}$$

where *A* is absorptivity of the laser into the material, ρ is the density, h_{s_m} is the enthalpy at melting per unit of mass, T_D is thermal diffusivity, and processing parameters: *P* is laser power, *v* is scanning speed, and *D*4 is laser beam size. Since the material system chosen for this specific application is 316L stainless steel, the following properties are used based on [36]: $A = 0.4$, $\rho = 7.98\,{}^{\mathrm{kg}}/_{\mathrm{m}^3}$, $h_{s_m} = 1.2 \times 10^6\,{}^{\mathrm{J}}/_{\mathrm{kg}}$, and $T_D = 5.38 \times 10^{-6}\,{}^{\mathrm{m}^2}/_{\mathrm{s}}$. The laser beam size value was kept consistent at $D4 = 52\,\mu\mathrm{m}$.

In the second bullet, a GP-based surrogate model based on $\frac{2d}{w}$ as a QoI can be constructed and its predictions used to identify the combinations of laser power and scanning speed within conduction or keyhole modes occur. This is done with the same experimental dataset presented in the previous subsection, since in addition to melt pool depth, the experimental dataset also consisted of melt pool width measurements (see Figure 5.7a).

Figures 5.11a and 5.11b provide processing windows of L-PBF manufacturing parameters that will produce melt pools within a desired thermal mode based on both criteria. By comparing the dashed line and the contour line at level 1 in Figure 5.11b, it is clear that conduction-mode regions in both plots ($\frac{2d}{w} < 1$ and $\frac{\Delta H}{h_s} < 30$) are very similar for laser powers up to $225\,\mathrm{W}$. Therefore, Figure 5.11b is defined as a data-sheet for appropriate L-PBF processing of 316L stainless steel for combinations of laser power and scanning speed, at laser beam size $D4 \approx 52\,\mu\mathrm{m}$ and layer thickness $50\,\mu\mathrm{m}$.

In the next two sections, another application will be described where formal UQ is used to perform statistical calibration of different computer models used in L-PBF via GP models in univariate and multivariate contexts.

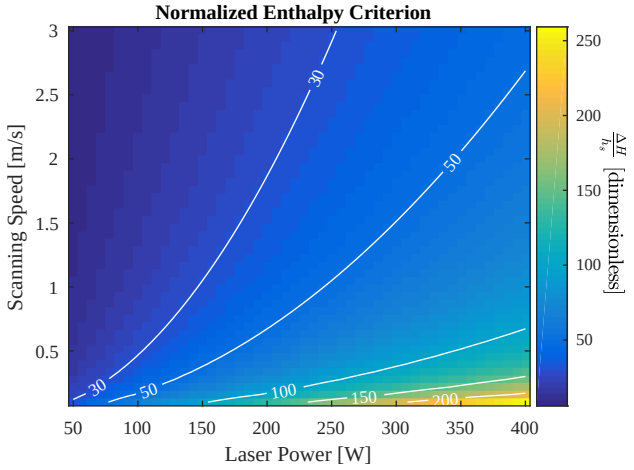

(a)

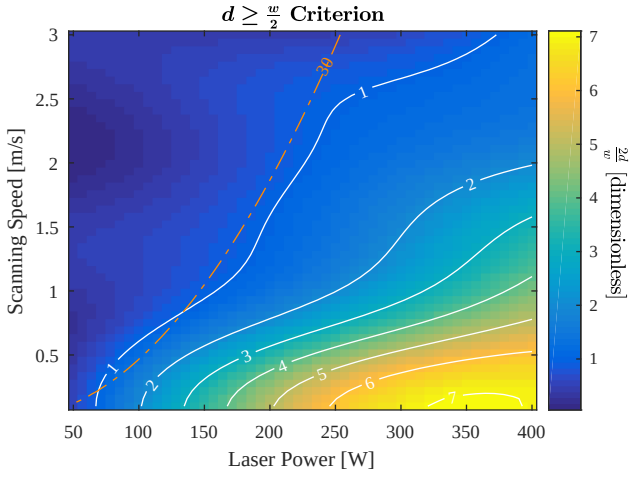

(b)

Figure 5.11: L-PBF process windows specifying conduction and keyhole mode behavior. **(a)** Normalized enthalpy $\frac{\Delta H}{h_s} \geq 30$ criterion. Reprinted with permission from [19]. **(b)** Melt pool dimensions $d \geq \frac{w}{2}$ criterion. The superimposed dashed line corresponds to $\frac{\Delta H}{h_s} = 30$ in order to compare both criteria. Reprinted with permission from [19].

5.3 Statistical Calibration of a Computational Precipitation Model

The widely accepted caveat on using computer simulation models is that they may present assumptions, misconceptions or errors that would not clearly recreate the real system they are representing. These modeling problems include incomplete understanding of the model parameters, incomplete knowledge of the physics and of the intrinsic stochastic behavior of the system being simulated. Consequently, it is crucial to characterize and quantify the uncertainties associated with these models toward leveraging their benefits and streamlining their applicability.

To propose a solution to this problem, GP models are employed to build a statistical calibration framework that will provide estimates of unknown model parameters based on computer simulations as well as experimental observations. This problem has been widely referred before as *calibration of computer models* starting with the seminal work by Kennedy and O'Hagan [92].

Before the framework is presented, some definitions and notations are needed in order to avoid subjectivities among distinct models. Any computational simulation models (for instance, a materials science simulation model) will be referred as a *computer model*, while the statistical framework by which a computer model is calibrated will be named the *statistical model*.

Under this context, the calibration problem distinguishes between two groups of inputs [140, 144]:

- *Control inputs* (or design variables), denoted by the vector $\mathbf{x}$, are variables that are set to known values by the user. Examples of these inputs include temperature, pressure, force, or any other quantities that are known and controlled by the user.

- *Calibration parameters*, denoted by the vector $\boldsymbol{\theta}$, represent physical parameters that can be specified as inputs to the computer model, and whose values are unknown or not measurable. Examples include properties of materials (such as conductivity or interfacial energy, among many) which are not easily determined for materials models.

The common definition from Section 3.1 is maintained for control inputs $\mathbf{x} \in \mathcal{X} \subseteq \mathbb{R}^q$, while calibration parameters are defined as $\boldsymbol{\theta} \in \mathcal{T} \subseteq \mathbb{R}^t$, where $\mathcal{T}$ is a t-dimensional region within

which it is believed that the true but unknown value for calibration parameters $\boldsymbol{\theta}^{\star}$ lies. Then, the goal of the calibration problem is to estimate these parameters such that the computer model simulations agree with the experimental observation of the real process being simulated. This is mathematically formulated in the next equation,

$$Z(\mathbf{x}) = Y(\mathbf{x}, \boldsymbol{\theta}^{\star}) + \delta(\mathbf{x}) + \epsilon(\mathbf{x}) \tag{5.13}$$

where $Z(\mathbf{x}) \in \mathcal{Z} \subseteq \mathbb{R}$ is an experimental observation at a given control input $\mathbf{x}$, $Y(\mathbf{x}, \boldsymbol{\theta}) \in \mathcal{Y} \subseteq \mathbb{R}$ is a computer model simulation resulting from evaluation at control inputs $\mathbf{x}$ and calibration parameters $\boldsymbol{\theta}$, $\delta(\cdot)$ is a discrepancy or model inadequacy function whose role is to account for the missing physics in the computer model, and $\epsilon(\cdot)$ is the observation or measurement error.

Under this formulation, a collection of several simulations from the computer model is needed in order to have enough information to solve the calibration problem. However, this becomes unfeasible when the computer model is computationally expensive with simulations requiring vast amount of computational resources and time. When this is the case, a surrogate model approach will be thus used as presented in several previous sections in this dissertation.

Therefore, two different types of calibration approaches will be presented: a *direct model* calibration where the computer model is not computationally expensive and it can be directly used to conduct the calibration, and a *surrogate model* calibration where a surrogate model is put in place of the computationally expensive computer model. The framework is applied in order to calibrate a *precipitation* model for shape-memory alloys (specifically Nickel-Titanium, also known as nitinol, and referred as NiTi).

Precipitation modeling is used to predict the nucleation and growth of a secondary phase within the matrix of a primary phase in the microstructure of a material. These small precipitates (secondary-phase particles dispersed throughout the material) are compositionally and/or structurally different than the surrounding matrix phase, allowing their process-dependent morphologies to be tracked as they evolve in the presence of various environmental conditions. The sizes

and shapes of these particles can drastically alter the properties of the overall material [145, 146]. In the context of this research, interest is pointed towards nickel composition of the matrix which is calculated at any step in the process through stoichiometric considerations and mass-balance equations involving nickel in the precipitates and the initial nickel content of the material before thermal processing. In turn, the composition of nickel in the matrix, the volume fraction of the precipitates and their size distribution control the final shape-memory behavior in NiTi alloys [147].

Three terms (interfacial energy, diffusion correction prefactor and diffusion correction exponential factor) significantly influence the kinetic behavior of the overall model. The interfacial energy term influences the behavior of the nucleation portion of the model and the diffusion correction factors equally influence all three stages of precipitate evolution listed above by modifying the substitutional diffusivity of the matrix phase. Values for interfacial energy are not completely unknown, but they are not known with as much accuracy as they should be, especially when considering how sensitive the entire model is to this term. Therefore, they are considered to calibrate the model through the present methodology.

Both types of inputs for this model are listed as follows:

- Control inputs $\mathbf{x}$:
  - Initial nickel content in the alloy [at. %].
  - Aging (heat treatment) temperature [$^{\circ}\mathrm{C}$].
  - Aging (heat treatment) time [s].
- Calibration parameters $\boldsymbol{\theta}$:
  - Interfacial energy [$^{\mathrm{J}}/_{\mathrm{m}^2}$].
  - Diffusion correction prefactor [dimensionless].
  - Diffusion correction activation [$^{\mathrm{J}}/_{\mathrm{mol}}$].
- Output of the computer model $Y(\mathbf{x}, \boldsymbol{\theta})$ and the process $Z(\mathbf{x})$
  - Final nickel content of the surrounding matrix [at. %].

5.3.1 Direct Model Calibration

For this case, the computer model is directly used on the calibration procedure, thus only the last two terms from Equation (5.13) need to be statistically defined. The discrepancy function is modeled as a GP, $\delta(\cdot) \sim \mathrm{GP}(\mu_\delta, C_\delta)$, following the definitions in Section 3.3.1, with mean function

$$\mu_\delta(\mathbf{x}) = H_\delta(\mathbf{x})\,\boldsymbol{\beta}_\delta \tag{5.14}$$

where $H_\delta(\mathbf{x}) = \left[1, \mathbf{x}^\top\right]$, and a non-stationary anisotropic Matern covariance function

$$C_\delta(\mathbf{x}_i, \mathbf{x}_j) = \sigma^2 \frac{2^{1-\nu}}{\Gamma(\nu)} \left(\sqrt{2\nu}Q\right)^\nu \mathcal{K}_\nu\left(\sqrt{2\nu}Q\right) \tag{5.15}$$

where σ^2 represents the variance of the real process (precipitation in this case), ν is the smoothness parameter of the covariance function and is selected to be fixed at $\nu = \frac{1}{2}$, $\mathcal{K}_\nu(\cdot)$ is the modified Bessel function of the second kind of order ν, $\Gamma(\cdot)$ is the gamma function, and

$$Q = \sqrt{\sum_{k=1}^{q} \left(\frac{x_{i,k} - x_{j,k}}{\omega_k}\right)^2}$$

is the similarity measure between $\mathbf{x}_i$ and $\mathbf{x}_j$ known as the Mahalanobis distance, with length-scale parameters ω_k which control the relative influence of each input dimension to the process.

The error term is modeled as i.i.d. normal random variables,

$$\epsilon(\mathbf{x}) \sim \mathrm{N}\left(0, \tau^2\right) \tag{5.16}$$

and thus the statistical model from Equation (5.13) is also a GP model fully characterized by the set of parameters

$$\boldsymbol{\Omega} = \left\{\boldsymbol{\theta}, \boldsymbol{\beta}_\delta, \sigma^2, \omega_1, \ldots, \omega_q, \tau^2\right\}$$

For the Direct Model calibration, the datasets collected as defined in Equation (3.3) will include

experimental observations:

$$\mathbb{X} = \begin{bmatrix} \mathbf{x}_1^\top \\ \mathbf{x}_2^\top \\ \vdots \\ \mathbf{x}_n^\top \end{bmatrix}, \ \mathbb{Z} = \begin{bmatrix} Z(\mathbf{x}_1) \\ Z(\mathbf{x}_2) \\ \vdots \\ Z(\mathbf{x}_n) \end{bmatrix}$$

and the computer model will execute and gather a simulation dataset every time it is called within the framework, which will be designated as

$$\mathbb{Y} = \begin{bmatrix} Y(\mathbf{x}_1, \boldsymbol{\theta}) \\ Y(\mathbf{x}_2, \boldsymbol{\theta}) \\ \vdots \\ Y(\mathbf{x}_n, \boldsymbol{\theta}) \end{bmatrix}$$

These datasets yield the next likelihood function based on definition of the model in Equation (5.13)

$$p(\mathbb{Z}|\mathbb{X}, \mathbb{Y}, \boldsymbol{\Omega}) \sim \mathrm{N}_n(\mathbb{Y} + \mathbf{H}_\delta \boldsymbol{\beta}_\delta, \boldsymbol{\Sigma}) \tag{5.17}$$

where $\boldsymbol{\Sigma} = \mathbf{C}_\delta + \tau^2 \mathbf{I}_n$, $\mathbf{C}_\delta$ is the matrix calculated the pair-wise evaluation of input dataset in the covariance function C_δ, $\mathbf{I}_n$ is the identity matrix of size $n \times n$, and matrix $\mathbf{H}_\delta = H_\delta(\mathbf{X})$.

The parameters are estimated under a Bayesian procedure, and thus, prior distributions for the hyperparameters are selected as:

$$\begin{aligned} p(\theta_1) &\sim \mathrm{U}(0, 0.1) \times \mathbf{1}_{\{Y(\mathbf{x},\boldsymbol{\theta}) \neq x_1\}}(\theta_1) \\ p(\theta_2) &\sim \mathrm{U}(0, 100) \times \mathbf{1}_{\{Y(\mathbf{x},\boldsymbol{\theta}) \neq x_1\}}(\theta_2) \\ p(\theta_3) &\sim \mathrm{U}(0, 1000) \times \mathbf{1}_{\{Y(\mathbf{x},\boldsymbol{\theta}) \neq x_1\}}(\theta_3) \\ p(\beta_j) &\sim \mathrm{U}(-\infty, \infty) \\ p\left(\sigma^2\right) &\sim \mathrm{IG}(2, 1) \end{aligned}$$

$$p(\omega_j) \sim \mathrm{U}(0, \infty)$$
$$p\left(\tau^2\right) \sim \mathrm{IG}(2, 0.2)$$

These priors follow the same reasoning as with previous sections by selecting non-informative and conjugate distributions. A special note worth mentioning is regarding the selection for calibration parameters $\boldsymbol{\theta}$, where an indicator function $\mathbf{1}_{\{A\}}(x)$ has been used. This function is equal to 1 if $x \in A$ and 0 otherwise, and it is used to reject values of $\theta_1, \theta_2, \theta_3$ for which the final (output) and initial (input) content of nickel are equal, which indicates that precipitation did not occur. This represents an anomaly that needs to be discarded.

The posterior distributions of hyperparameter set $\boldsymbol{\Omega}$ can be calculated via MCMC algorithms, and special importance is given to those posterior estimates for calibration parameters $\boldsymbol{\theta}$. Furthermore, the calibrated model can then be used in a prediction stage following the next equations, which generalize onto the calibration framework based on original Equations (3.29) and (3.30):

$$p(\mathbb{Z}_0|\mathbb{Z}, \mathbb{Y}, \mathbb{X}, \mathbb{X}_0, \boldsymbol{\Omega}) \sim \mathrm{N}_{n_0}(\boldsymbol{\mu}_0, \boldsymbol{\Sigma}_0)$$

where

$$\boldsymbol{\mu}_0 = Y(\mathbb{X}_0) + \mu(\mathbb{X}_0) + C_\delta(\mathbb{X}_0, \mathbb{X})\boldsymbol{\Sigma}^{-1}(\mathbb{Z} - \mathbb{Y} - \mathbf{H}_\delta\boldsymbol{\beta}_\delta) \tag{5.18}$$
$$\boldsymbol{\Sigma}_0 = C_\delta(\mathbb{X}_0, \mathbb{X}_0) - C_\delta(\mathbb{X}_0, \mathbb{X})\boldsymbol{\Sigma}^{-1}C_\delta(\mathbb{X}, \mathbb{X}_0) + \tau^2\mathbf{I}_{n_0} \tag{5.19}$$

for an unseen input dataset $\mathbb{X}_0$.

The experimental data represents the final nickel content of the matrix [%at. Ni] corresponding to a specific heat treatment regime (aging temperature and aging time) for a particular NiTi alloy with initial composition. During the experiments, the samples were individually sealed into quartz tubes under a high-purity argon atmosphere to avoid oxygen contamination. Heat treatments were performed in a muffle furnace followed by subsequent water quenching. A technique called differential scanning calorimetry (DSC) was first used to directly measure the resulting martensitic

transformation temperature of each heat treated alloy.

The martensitic transformation temperature is a property of NiTi alloys that is highly sensitive to the amount of nickel in the surrounding matrix. The formation of nickel-rich precipitates causes a change in the composition of the alloy, which in turn reflects into a change in the martensitic transformation temperatures. In other words, the martensitic transformation temperature determined through DSC can be used to indirectly measure the matrix composition.

The relationship between NiTi composition and the martensitic transformation temperatures has been extensively studied in literature, such as [148–150]. In the current work, the DSC measurements of the martensitic transformation temperatures were converted to nickel composition [%at. Ni] using curve fitting to data presented in Frenzel et al. [151], and yielded a dataset of 36 experimental observations used henceforth. From this set, 31 observations randomly selected will be used to calibrate (or train) the precipitation model (called *Training set*) and 5 will be used for testing and validation to assess the predictive performance of the calibrated model (called *Test set*).

Consequently, the Direct Model calibration framework was executed with the observed dataset to estimate the calibration parameters through MCMC using the training set with $n = 31$. Since the precipitation model is being used online within the statistical framework, the whole procedure was implemented over a 10-core computer node (with parallelization in some parts of the routine) and run for 15,000 iterations, with a 25% burn-in period and thinning every fifth iteration. Results of the posterior distributions of the calibration parameters are shown in the three panes of Figure 5.12, where each plot displays the histogram with 20 bins and their corresponding kernel density estimate.

From the plots in Figure 5.12, it is clear to see that θ_1 and θ_2 have defined informative and unimodal posterior distributions, with θ_1 having a unique peak while θ_2 being skewed to the right in addition to having a unique peak. Parameter θ_3 behaves in an opposed manner, with its posterior distribution showing some uniformity, which implies that all the values across its domain are equally likely to characterize the real process. Table 5.3 presents mean, mode (most frequent value), and standard deviation of the posterior distribution for the calibration parameters.

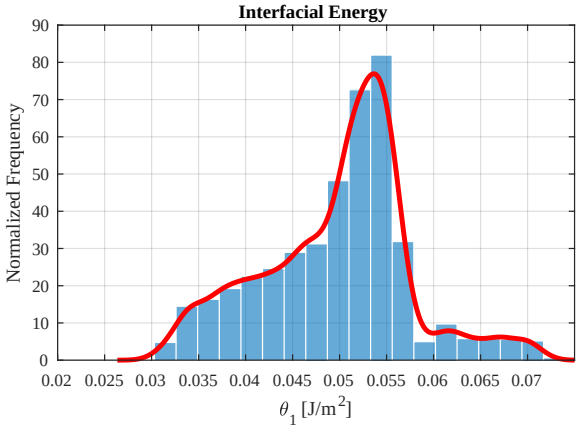

(a)

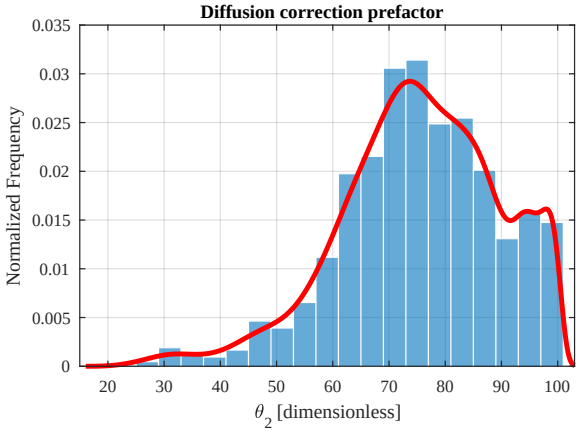

(b)

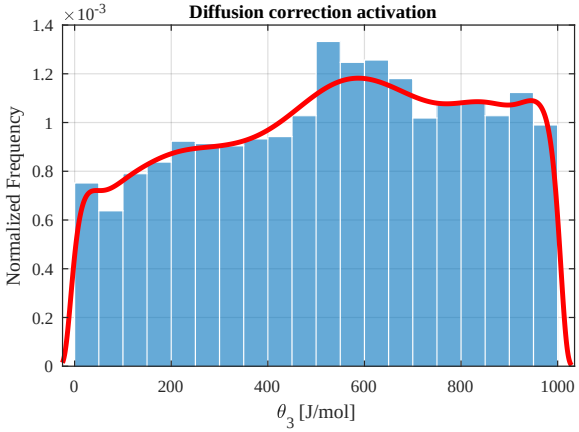

(c)

Figure 5.12: Histograms and kernel density estimates of the posterior distribution for calibration parameters in Direct Model calibration. **(a)** Intefacial energy. Reprinted with permission from [140]. **(b)** Diffusion correction prefactor. Reprinted with permission from [140]. **(c)** Diffusion correction activation. Reprinted with permission from [140].

Table 5.3: Estimates for calibration parameters via Direct Model calibration. Reprinted with permission from [140].

Parameter	Mean	Mode	St. Dev.
Interfacial energy θ_1	0.0498	0.0536	0.0079
Diffusion correction prefactor θ_2	75.4143	73.7015	13.9599
Diffusion correction activation θ_3	533.6609	587.1682	274.9424

The narrow nature of the distribution for θ_1 can be explained by its appearance in the governing equations for precipitate nucleation, since interfacial energy is so dominant in precipitation models due to the following fact: relatively small values imply almost no barrier to nucleation, leading to the precipitation of all the precipitates that can form in the material (ultimately limited by thermodynamics) right at the beginning of the precipitation process; on the other hand, slightly high values for this parameter may result in a barrier to nucleation that effectively results in no precipitation of secondary phases at all during reasonable heat treatment times. Thus, only a narrow range of interfacial energy values can yield physically meaningful precipitation predictions. In fact, the estimated mean and mode for θ_1 are well within the range of values reported in the literature and very close to the value calculated through parametric sweep-experimental data coupling.

Regarding the remaining calibration parameters, it is more difficult to ascertain their direct significance since they represent corrections to the diffusivity values taken from the precipitation computer model. These corrections are necessary as one does not really know the state of the microstructure before the precipitation starts. Of particular effect is the presence, for example, of grain boundaries, dislocations, and other defects that can catalyze (facilitate) the nucleation of the second phase precipitate particles. The ranges for each parameter were selected such that only physically realistic values would be calculated for these two parameters, and although they represent correction factors and as such have no direct physical significance themselves, it can be inferred that they are less influential (i.e., have broader distributions) for two main reasons: first, they are not a largely influential parameter within the governing equations, and second, they are

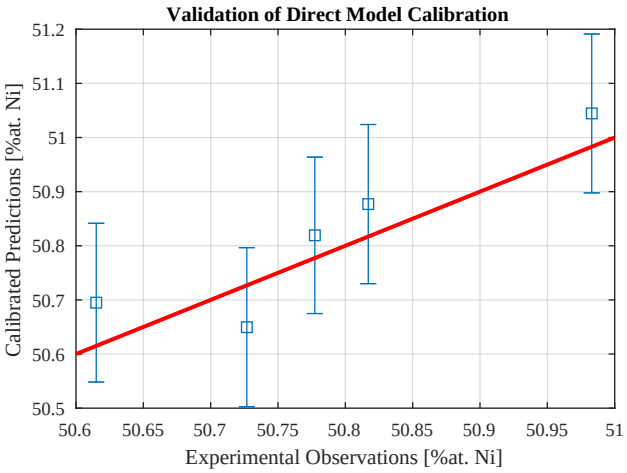

Figure 5.13: Performance of the calibrated model on the test set via Direct Model calibration. Reprinted with permission from [140].

implemented in a later stage of the precipitate evolution which reduces their influence with respect to θ_1.

To assess the performance of the calibrated model via Direct Model calibration, predictions on the test set were calculated and are presented in Figure 5.13. Numerically, the average deviation is $\mathrm{MAPE}_{\mathrm{dir}} = 0.0641\%\mathrm{at.\,Ni}$, which is an acceptable result given all the experimental uncertainties in these types of studies.

5.3.2 Surrogate Model Calibration

The Surrogate Model calibration approach is applied when executing large number of simulations from the computer model result infeasible due to the burden on computational resources. In this case, the computer model is replaced for a data-driven fast surrogate model which is modeled as a GP in a similar manner as with Section 5.2.1.

The same definition of the statistical model from Equation (5.13) will be used, however the computer model component is defined as a surrogate model η and the ith input tuple is denoted as $(\mathbf{x}, \boldsymbol{\theta})_i = [x_{i,1}, \ldots, x_{i,q}, \theta_{i,1}, \ldots, \theta_{i,t}]^\top$. Hence, the definition yields the next GP,

$$Y(\mathbf{x}, \boldsymbol{\theta}) \equiv \eta(\mathbf{x}, \boldsymbol{\theta}) \sim \mathrm{GP}(\mu_\eta, C_\eta)$$

with linear regression mean function

$$\mu_\eta = H_\eta(\mathbf{x}, \boldsymbol{\theta})\,\boldsymbol{\beta}_\eta \tag{5.20}$$

where $H_\eta(\mathbf{x}, \boldsymbol{\theta}) = \left[1, \mathbf{x}^\top\right]$, and anisotropic stationary squared exponential covariance function

$$C_\eta\left((\mathbf{x}, \boldsymbol{\theta})_i, (\mathbf{x}, \boldsymbol{\theta})_j\right) = \sigma_\eta^2 \exp\left(-Q_\eta\right) \tag{5.21}$$

where σ_η^2 is the variance parameter of the computer model and Q_η is the spatial similarity map $Q_\eta \colon \mathcal{X} \times \mathcal{T} \to \mathbb{R}_+$ parameterized as

$$Q_\eta = \sum_{k=1}^{q} \left(\frac{x_{i,k} - x_{j,k}}{\omega_{1,k}}\right)^2 + \sum_{l=1}^{t} \left(\frac{\theta_{i,l} - \theta_{j,l}}{\omega_{2,l}}\right)^2$$

with length-scale parameters $\boldsymbol{\omega}_1 = \{\omega_{1,1}, \ldots, \omega_{1,q}\}$ and $\boldsymbol{\omega}_2 = \{\omega_{2,1}, \ldots, \omega_{2,t}\}$.

In order to first build the surrogate model, a simulation dataset of size *N* will be collected in the form of

$$\mathbb{X}_\eta = \begin{bmatrix} (\mathbf{x}_1, \boldsymbol{\theta}) \\ (\mathbf{x}_2, \boldsymbol{\theta}) \\ \vdots \\ (\mathbf{x}_N, \boldsymbol{\theta}) \end{bmatrix}, \; \mathbb{Y} = \begin{bmatrix} Y(\mathbf{x}_1, \boldsymbol{\theta}) \\ Y(\mathbf{x}_2, \boldsymbol{\theta}) \\ \vdots \\ Y(\mathbf{x}_N, \boldsymbol{\theta}) \end{bmatrix}$$

The discrepancy function from Equation (5.13) is defined similarly as with the Direct Model case, $\delta(\cdot) \sim \mathrm{GP}(\mu_\delta, C_\delta)$, with

$$\mu_\delta(\mathbf{x}) = H_\delta(\mathbf{x})\,\boldsymbol{\beta}_\delta \tag{5.22}$$

where $H_\delta(\mathbf{x}) = \left[1, \mathbf{x}^\top\right]$, and C_δ is an anisotropic stationary squared exponential covariance function defined by

$$C_\delta(\mathbf{x}_i, \mathbf{x}_j) = \sigma_\delta^2 \exp\left(-Q_\delta\right) \tag{5.23}$$

where σ_δ^2 is the variance parameter of the process and Q_δ is the similarity metric

$$Q_\delta = \sum_{k=1}^{q} \left(\frac{x_{i,k} - x_{j,k}}{\omega_{3,k}} \right)^2$$

with length-scale parameters $\boldsymbol{\omega}_3 = \{\omega_{3,1}, \ldots, \omega_{3,q}\}$.

The error term is again i.i.d. $\epsilon(\mathbf{x}) \sim \mathrm{N}(0, \tau^2)$, and consequently, the complete model is fully defined by the set of hyperparameters

$$\boldsymbol{\Omega} = \left\{ \boldsymbol{\theta}, \boldsymbol{\beta}_\eta, \boldsymbol{\beta}_\delta, \sigma_\eta^2, \sigma_\delta^2, \boldsymbol{\omega}_1, \boldsymbol{\omega}_2, \boldsymbol{\omega}_3, \tau^2 \right\}$$

In order to fully define the statistical model, the experimental dataset of size *n* is defined (and collected) as

$$\mathbb{X} = \begin{bmatrix} \mathbf{x}_1^\top \\ \mathbf{x}_2^\top \\ \vdots \\ \mathbf{x}_n^\top \end{bmatrix}, \; \mathbb{Z} = \begin{bmatrix} Z(\mathbf{x}_1) \\ Z(\mathbf{x}_2) \\ \vdots \\ Z(\mathbf{x}_n) \end{bmatrix}$$

and the complete data is aggregated and arranged as

$$\mathbf{D} = \begin{bmatrix} \mathbb{Y} \\ \mathbb{Z} \end{bmatrix}$$

and yield the likelihood function in the next equation:

$$p(\mathbf{D}|\mathbb{X}_\eta, \mathbb{X}, \boldsymbol{\Omega}) \sim \mathrm{N}_{N+n}(\mathbf{H}\boldsymbol{\beta}, \boldsymbol{\Sigma}) \tag{5.24}$$

where

$$\boldsymbol{\beta} = \begin{bmatrix} \boldsymbol{\beta}_\eta^\top \\ \boldsymbol{\beta}_\delta^\top \end{bmatrix}$$

$$\mathbf{H} = \begin{bmatrix} H_\eta\left(\mathbb{X}_\eta\right) & 0 \\ H_\eta\left(\mathbb{X}, \boldsymbol{\theta}\right) & H_\delta\left(\mathbb{X}\right) \end{bmatrix}$$

$$\boldsymbol{\Sigma} = \begin{bmatrix} C_\eta\left(\mathbb{X}_\eta, \mathbb{X}_\eta\right) & C_\eta\left(\mathbb{X}_\eta, \left(\mathbb{X}, \boldsymbol{\theta}\right)\right) \\ C_\eta\left(\left(\mathbb{X}, \boldsymbol{\theta}\right), \mathbb{X}_\eta\right) & \tau^2\mathbf{I}_n + C_\eta\left(\left(\mathbb{X}, \boldsymbol{\theta}\right), \left(\mathbb{X}, \boldsymbol{\theta}\right)\right) + C_\delta\left(\mathbb{X}, \mathbb{X}\right) \end{bmatrix}$$

The parameters are estimated under a Bayesian procedure, and thus, prior distributions for the hyperparameters are selected as:

$$\begin{aligned} p\left(\theta_1\right) &\sim \mathrm{U}\left(0, 0.1\right) \\ p\left(\theta_2\right) &\sim \mathrm{U}\left(0, 100\right) \\ p\left(\theta_3\right) &\sim \mathrm{U}\left(0, 1000\right) \\ p\left(\beta_{\eta,j}\right) &\sim \mathrm{U}\left(-\infty, \infty\right) \\ p\left(\beta_{\delta,j}\right) &\sim \mathrm{U}\left(-\infty, \infty\right) \\ p\left(\sigma_\eta^2\right) &\sim \mathrm{IG}\left(2, 1\right) \\ p\left(\sigma_\delta^2\right) &\sim \mathrm{IG}\left(2, 1\right) \\ p\left(\omega_{i,j}\right) &\sim \mathrm{U}\left(0, \infty\right) \forall i \in \{1, 2, 3\} \\ p\left(\tau^2\right) &\sim \mathrm{IG}\left(2, 0.2\right) \end{aligned}$$

which follow same guidelines as with the previous case.

The posteriors distributions of hyperparameter set $\boldsymbol{\Omega}$ can be calculated via MCMC algorithms, and special importance is given to those posterior estimates for calibration parameters $\boldsymbol{\theta}$. Furthermore, the calibrated model can then be used in a prediction stage following the predictive posterior distribution:

$$p\left(\mathbb{Z}_0 | \mathbf{D}, \mathbb{X}_\eta, \mathbb{X}, \mathbb{X}_0, \boldsymbol{\Omega}\right) \sim \mathrm{N}_{n_0}\left(\boldsymbol{\mu}_0, \boldsymbol{\Sigma}_0\right)$$

where

$$\boldsymbol{\mu}_0 = \mathtt{h}\left(\mathbb{X}_0, \boldsymbol{\theta}\right)^\top \hat{\boldsymbol{\beta}} + \mathtt{c}_1\left(\mathbb{X}_0, \boldsymbol{\theta}\right)^\top \boldsymbol{\Sigma}^{-1}\left(\mathbf{D} - \mathbf{H}\hat{\boldsymbol{\beta}}\right) \tag{5.25}$$

$$\begin{aligned}\boldsymbol{\Sigma}_0 = {} & C_\eta\left(\left(\mathbb{X}_0, \boldsymbol{\theta}\right), \left(\mathbb{X}_0, \boldsymbol{\theta}\right)\right) + C_\delta\left(\mathbb{X}_0, \mathbb{X}_0\right) \\ & - \mathtt{c}_1\left(\mathbb{X}_0, \boldsymbol{\theta}\right)^\top \boldsymbol{\Sigma}^{-1}\mathtt{c}_1\left(\mathbb{X}_0, \boldsymbol{\theta}\right) + \mathtt{c}_2\left(\mathbb{X}_0, \boldsymbol{\theta}\right)^\top \mathbf{W}\mathtt{c}_2\left(\mathbb{X}_0, \boldsymbol{\theta}\right)\end{aligned} \tag{5.26}$$

for unseen input dataset $\mathbb{X}_0$ where

$$\begin{aligned}\mathtt{h}\left(\mathbb{X}_0, \boldsymbol{\theta}\right) &= \left[\begin{array}{cc} H_\eta\left(\mathbb{X}_0, \boldsymbol{\theta}\right) & H_\delta\left(\mathbb{X}_0\right) \end{array}\right]^\top \\ \mathtt{c}_1\left(\mathbb{X}_0, \boldsymbol{\theta}\right) &= \left[\begin{array}{cc} C_\eta\left(\left(\mathbb{X}_0, \boldsymbol{\theta}\right), \mathbb{X}_\eta\right) & C_\eta\left(\left(\mathbb{X}_0, \boldsymbol{\theta}\right), \left(\mathbb{X}, \boldsymbol{\theta}\right)\right) + C_{eta}\left(\mathbb{X}_0, \mathbb{X}\right) \end{array}\right]^\top \\ \mathtt{c}_2\left(\mathbb{X}_0, \boldsymbol{\theta}\right) &= \mathtt{h}\left(\mathbb{X}_0, \boldsymbol{\theta}\right) - \mathbf{H}^\top\boldsymbol{\Sigma}^{-1}\mathtt{c}_1\left(\mathbb{X}_0, \boldsymbol{\theta}\right) \\ \mathbf{W} &= \left(\mathbf{H}^\top\boldsymbol{\Sigma}^{-1}\mathbf{H}\right)^{-1} \\ \hat{\boldsymbol{\beta}} &= \mathbf{W}\mathbf{H}^\top\boldsymbol{\Sigma}^{-1}\mathbf{D}\end{aligned}$$

Before the estimation phase, the simulation dataset $\mathbb{Y}$ was collected and consisted of $N = 3025$ simulations was collected via a LHS design, while the experimental dataset was the same as in the Direct Model calibration ($n = 31$ data points for training and $n_0 = 5$ as test set).

MCMC was used for posterior distribution estimation and followed the same procedure as for the previous case: 15,000 iterations with 25% burn-in period and thinning set to every fifth iteration. The posterior distributions for the calibration parameters are shown in Figure 5.14 and their values are presented in Table 5.4. By inspecting the obtained posterior distributions, we see some differences from those obtained using Direct Model calibration. The distribution of θ_1 is an informative bimodal behavior with two distinctive peaks. The distribution of θ_2 is skewed to the left, in contrast to the direct calibration case, and the distribution of θ_3 shows similar uninformative behavior to the direct calibration case.

The bimodal nature of θ_1 is most likely a result of the inability of the surrogate model to directly

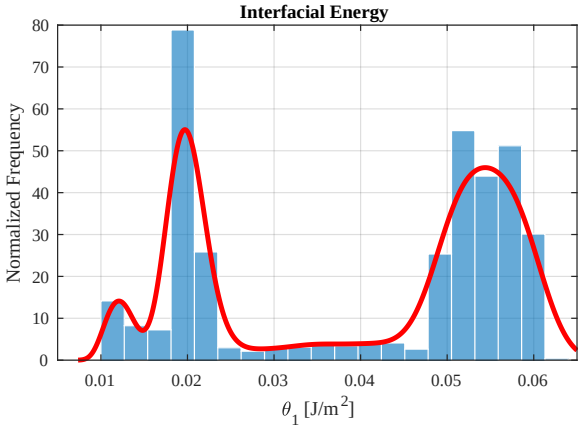

(a)

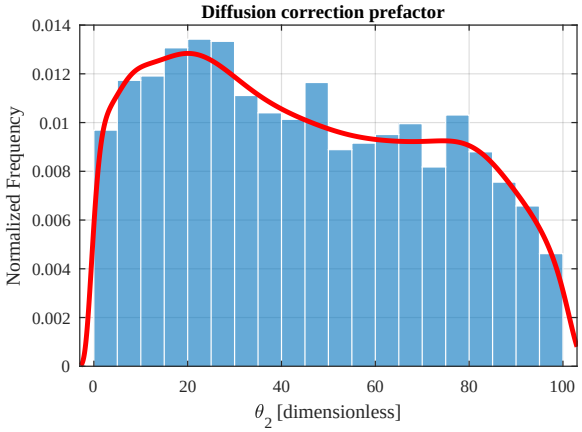

(b)

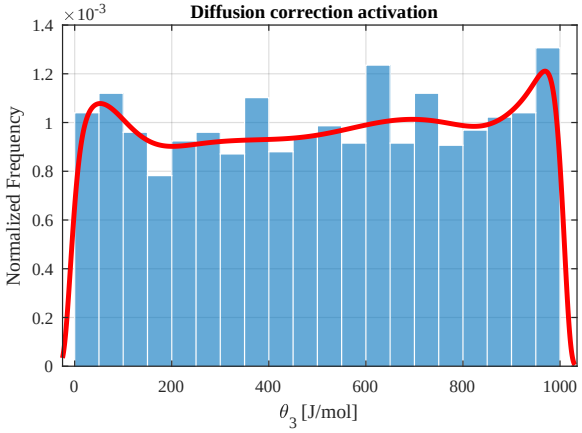

(c)

Figure 5.14: Histograms and kernel density estimates of the posterior distribution for calibration parameters in Surrogate Model calibration. **(a)** Intefacial energy. Reprinted with permission from [140]. **(b)** Diffusion correction prefactor. Reprinted with permission from [140]. **(c)** Diffusion correction activation. Reprinted with permission from [140].

Table 5.4: Estimates for calibration parameters via Surrogate Model calibration. Reprinted with permission from [140].

Parameter	Mean	Mode	St. Dev.
Interfacial energy θ_1	0.0401	0.0197 and 0.0544	0.0173
Diffusion correction prefactor θ_2	44.9248	20.0463	27.4283
Diffusion correction activation θ_3	512.0809	969.1429	294.1693

compare initial and final nickel content of the matrix, which is used as a sanity check in the direct model. To elaborate on this, note that while the surrogate model is to replace the computer model, it does not capture any physics, and thus does not recognize that cases where the initial and final nickel content are identical should be discarded.

The explanation of θ_2 and θ_3 distributions remains essentially the same for the Surrogate Model as it was for the Direct Model case. These two parameters are correction factors and as such have no direct physical connection. All that can be said is that the mean and mode values seen in Figure 5.14 will result in physically realistic diffusion coefficient and activation energy values. Again, these two distributions are broader because they influence later stages of the precipitate evolution which have less of an impact on overall precipitate morphology than early stage parameters like θ_1.

To analyze the performance of the Surrogate Model, we run a 10-fold CV procedure over the 3025 simulation datapoints and visually present in Figure 5.15a. It is easy to see that most blue circles are over the ideal line, with some scattered points off of the red line. The average deviation from the ideal line is $\mathrm{MAPE}_{\mathrm{10CV}} = 0.0661\%\mathrm{at.\,Ni}$, which further confirms the results that the surrogate model adequately captures the behavior of the computer model.

In regards to the calibrate model via Surrogate Model calibration, a performance analysis identical to the Direct Model case was also executed, where predictions on the test set were calculated and compared to the actual observed values. These results are presented in Figure 5.15b, and numerically, the average deviation is $\mathrm{MAPE}_{\mathrm{sur}} = 0.0456\%\mathrm{at.\,Ni}$, which is an acceptable result given all the experimental uncertainties in these types of studies.

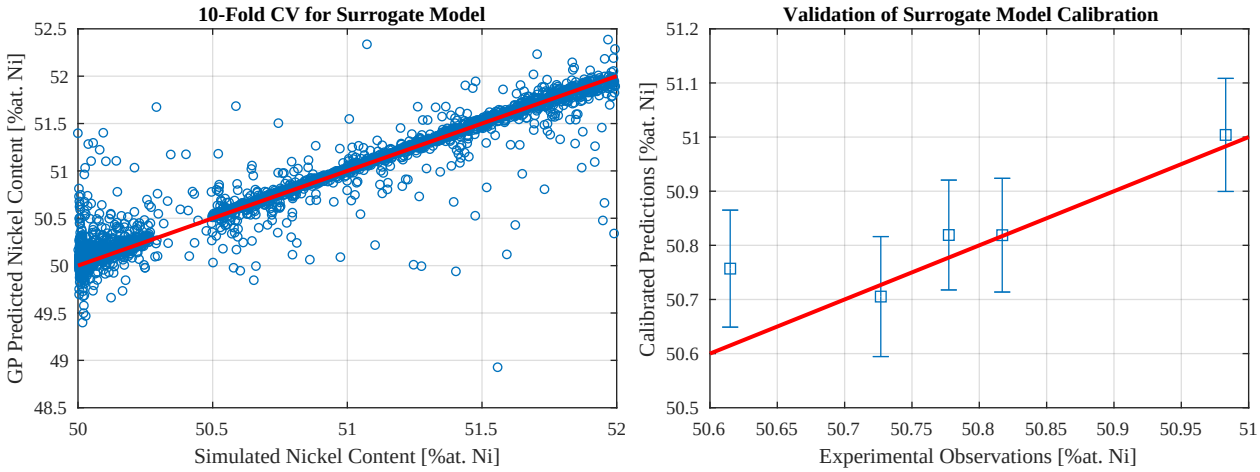

Figure 5.15: Performance of the calibrated model on the test set via Surrogate Model calibration. **(a)** 10-fold CV of the Surrogate Model. Reprinted with permission from [140]. **(b)** Validation of the calibrated model on test set. Reprinted with permission from [140].

The numerical results from both approaches are quite interesting given the fact that the Surrogate Model calibration outperforms the Direct Model calibration when MAPE is used as performance metric. If in turn, we use RMSPE (square root from Equation (A.9)), it results that $\mathrm{RMSPE}_{\mathrm{dir}} = 0.0656\%\mathrm{at.\,Ni}$ and $\mathrm{RMSPE}_{\mathrm{sur}} = 0.0675\%\mathrm{at.\,Ni}$, and in this case, the Direct Model calibration outperforms the Surrogate Model calibration. This is due to the fact that MSPE penalizes more to large errors (i.e., large deviations from the ideal line), and this means that on average, the Surrogate Model calculates predictions that are off the red line in a higher magnitude than those from the Direct Model. Nevertheless, both errors show an acceptable result confirming the validation of both calibration models.

In the next section, a generalization of this problem into a multivariate setting will be presented to calibrate a thermal model.

5.4 Multivariate Statistical Calibration of a Finite Element Thermal Model

In this section, the objective is to statistically calibrate a three-dimensional FEM-based L-PBF thermal model implemented to study melt pool characteristics, including geometry and thermal

profiles, during the fabrication of single tracks printed on a thin layer of powder on top of a solid substrate. In this model, the powder layer is assumed to be a continuum medium over thick substrate, and hence, it corresponds to a continuum-scale model as explained in Section 2.1.3. The model was developed in the Department of Materials Science and Engineering at Texas A&M University, and consequently, it will be referred as the *TAMU thermal model* henceforth.

Specifically, the present model accounts for several heat transfer mechanisms that take place during L-PBF like conduction, convection, radiation, phase transitions (namely, solid-to-liquid and liquid-to-gas transitions), latent heat of melting/evaporation, temperature dependent material properties, and the effective thermo-physical properties for the powder layer were considered. Furthermore, heat loss due to evaporation was incorporated by employing a simple approach based on the implementation of a heat sink on the powder surface. The laser beam was defined as a two-dimensional Gaussian distributed moving heat source, and natural convection, radiation and evaporation were employed as boundary conditions on the powder surface, while a symmetry boundary condition was applied along the scanning path to reduce the computational cost.

Since the TAMU thermal model takes different physical mechanisms into account, there are multiple materials parameters that influence the model results, and thus, the predictive capabilities of the model. After preliminary simulation experiments, the following parameters were identified as most significant on variability in model outputs: laser absorptivity, powder-bed porosity and thermal conductivity of the liquid.

It is known that the laser absorptivity is a function of temperature and has different values for powder, solid and liquid materials. There are several factors (e.g., beam intensity, wavelength, temperature, oxidation, powder size and distribution) affecting the absorptivity of the material. Therefore, it is difficult to experimentally measure it. Note that while low values of absorptivity result in insufficient energy input and incomplete melting of the powder particles, very high values lead to overheating of the particles, hence, over estimation of the melt pool size. Moreover, powder porosity is used as an input to predict the effective thermo-physical properties (thermal conductivity, density, heat capacity) of the powder layer. Therefore, it has a significant influence on the

predicted thermal distribution. Considering the aforementioned aspects, a need for the calibration of these three parameters was realized.

The definitions from last section are maintained for control inputs $\mathbf{x} \in \mathcal{X} \subseteq \mathbb{R}^q$ and calibration parameters $\boldsymbol{\theta} \in \mathcal{T} \subseteq \mathbb{R}^t$, however the calibration problem is now formulated to a multivariate setting, and thus its mathematical formulation is

$$\mathbf{Z}(\mathbf{x}) = \mathbf{Y}(\mathbf{x}, \boldsymbol{\theta}^\star) + \boldsymbol{\delta}(\mathbf{x}) + \boldsymbol{\epsilon}(\mathbf{x}) \tag{5.27}$$

where $\mathbf{Z}(\mathbf{x}) \in \mathcal{Z} \subseteq \mathbb{R}^d$ is an experimental observation producing d different QoIs at a given control input $\mathbf{x}$, $\mathbf{Y}(\mathbf{x}, \boldsymbol{\theta}) \in \mathcal{Y} \subseteq \mathbb{R}^d$ is a computer model simulation that returns d QoIs resulting from evaluation at control inputs $\mathbf{x}$ and calibration parameters $\boldsymbol{\theta}$, $\boldsymbol{\delta}(\cdot)$ is a discrepancy or model inadequacy function whose role is to account for the missing physics in the computer model, and $\boldsymbol{\epsilon}(\cdot)$ is the observation or measurement error.

In terms of the TAMU thermal model, the corresponding inputs and outputs under investigation are the following:

- Control Inputs $\mathbf{x}$:
  - Laser power [W].
  - Scanning speed [$^{\mathrm{mm}}/_{\mathrm{s}}$].
- Calibration parameters $\boldsymbol{\theta}$:
  - Powder-bed porosity [$\%$].
  - Laser absorptivity [$\%$].
  - Coefficient of thermal conductivity for liquid [$^{\mathrm{W}}/_{\mathrm{m \cdot K}}$].
- Outputs of the computer model $\mathbf{Y}(\mathbf{x}, \boldsymbol{\theta})$ and the process $\mathbf{Z}(\mathbf{x})$
  - Melt pool depth [$\mu\mathrm{m}$].
  - Melt pool width [$\mu\mathrm{m}$].

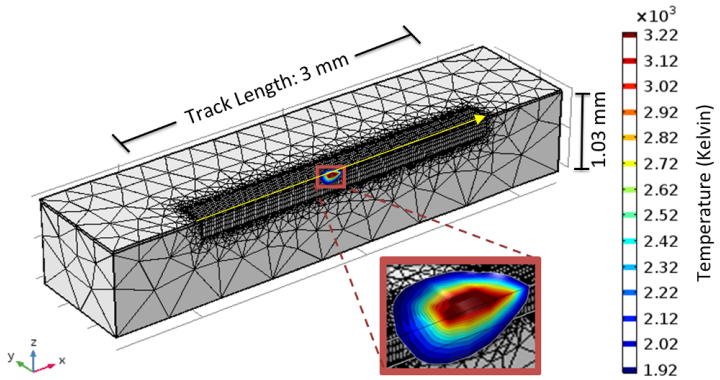

Figure 5.16: Simulation sample from the TAMU thermal model showing melt pool temperature profiles.

– Melt pool peak temperature [°C].

Furthermore, the model simulates the fabrication of $3\,\mathrm{mm}$ single tracks, with powder layer simulated as a $30\,\mu\mathrm{m}$ continuum medium over a $1\,\mathrm{mm}$ thick substrate both made of Ti-6Al-4V alloy. To ensure accurate analysis, a fine mesh element was used for the laser-powder interaction zones, while a coarser element was employed for the rest of the simulation domain. Second-order quadrilateral Lagrange elements were used for the entire domain, while the $30\,\mu\mathrm{m}$ fine elements were found suitable for the powder-bed based on the mesh convergence analysis. Figure 5.16 shows a sample output of the model with melt pool temperature profiles.

Since the TAMU thermal model is computationally expensive, the multivariate statistical calibration framework will only be presented for the Surrogate Model case. Furthermore, the framework will be split into two subsections: first the construction of the multivariate surrogate model will be explained, and then the calibration procedure will be presented.

5.4.1 Surrogate Model

Similar to Sections 5.2 and 5.3, the construction of the surrogate model will be based on GP modeling techniques (generalized to a multivariate space in this case) presented on Section 3.3.1. The modeling methodologies in this section are based on the work of Conti and O'Hagan [152]. Therefore, the computer model is replaced by a multivariate GP-based surrogate model in Equa-

tion (5.27), using a separable model formulation:

$$\mathbf{Y}(\mathbf{x}, \boldsymbol{\theta}) \equiv \boldsymbol{\eta}(\mathbf{x}, \boldsymbol{\theta}) \sim \mathrm{GP}_d(\mu_\eta, r_\eta \boldsymbol{\Lambda}_\eta)$$

with $\boldsymbol{\Lambda}_\eta \in \mathbb{R}_+^{d,d}$.

For the formulation of the GP functions, the *i*th tuple is denoted as $(\mathbf{x}, \boldsymbol{\theta})_i = [x_{i,1}, \ldots, x_{i,q}, \theta_{i,1}, \ldots, \theta_{i,t}]^\top$ and the mean function is assumed as linear regression

$$\mu_\eta = \mathbf{B}_\eta^\top H_\eta(\mathbf{x}, \boldsymbol{\theta}) \tag{5.28}$$

where $H_\eta \colon \mathcal{X} \times \mathcal{T} \to \mathbb{R}^m$ is a function that maps the input spaces to *m* basis functions, and is chosen to be $H_\eta(\mathbf{x}, \boldsymbol{\theta}) = \left[1, \mathbf{x}^\top, \boldsymbol{\theta}^\top\right]$. The matrix of coefficients is $\mathbf{B}_\eta = \left[\boldsymbol{\beta}_1, \ldots, \boldsymbol{\beta}_q\right] \in \mathbb{R}^{m,d}$.

The correlation function is an anisotropic stationary squared exponential correlation function

$$r_\eta\left((\mathbf{x}, \boldsymbol{\theta})_i, (\mathbf{x}, \boldsymbol{\theta})_j\right) = \exp\left[-\left((\mathbf{x}, \boldsymbol{\theta})_i - (\mathbf{x}, \boldsymbol{\theta})_j\right)^\top \boldsymbol{\Psi}_\eta \left((\mathbf{x}, \boldsymbol{\theta})_i - (\mathbf{x}, \boldsymbol{\theta})_j\right)\right] \tag{5.29}$$

where $\boldsymbol{\Psi}_\eta = \mathrm{diag}\left(\boldsymbol{\psi}_\eta\right)$ is a diagonal matrix of positive roughness parameters with $\boldsymbol{\psi}_\eta = [\psi_1, \ldots, \psi_q, \psi_{q+1}, \ldots, \psi_{q+t}] \in \mathbb{R}_+^{q+t}$. These roughness parameters are the inverse of length-scale parameters used in Sections 5.2 and 5.3 and explain the smoothness of the GP model. Therefore, the complete surrogate model is fully defined by the set of hyperparameters

$$\boldsymbol{\Omega}_\eta = \{\mathbf{B}_\eta, \boldsymbol{\Lambda}_\eta, \boldsymbol{\Psi}_\eta\}$$

In order to build the surrogate model, a simulation dataset of size *N* will be collected in the form of

$$\mathbb{X}_\eta = \begin{bmatrix} (\mathbf{x}_1, \boldsymbol{\theta}) \\ (\mathbf{x}_2, \boldsymbol{\theta}) \\ \vdots \\ (\mathbf{x}_N, \boldsymbol{\theta}) \end{bmatrix}, \ \mathbb{Y} = \begin{bmatrix} \mathbf{Y}(\mathbf{x}_1, \boldsymbol{\theta}) \\ \mathbf{Y}(\mathbf{x}_2, \boldsymbol{\theta}) \\ \vdots \\ \mathbf{Y}(\mathbf{x}_N, \boldsymbol{\theta}) \end{bmatrix}$$

and will yield the following likelihood function for the surrogate model:

$$p\left(\mathbb{Y}|\mathbb{X}_\eta, \boldsymbol{\Omega}_\eta\right) \sim \mathrm{N}_{N,d}\left(\mathbf{M}_\eta, \mathbf{R} \otimes \boldsymbol{\Lambda}_\eta\right) \tag{5.30}$$

where

$$\begin{aligned}\mathbf{M}_\eta &= \mu_\eta\left(\mathbb{X}_\eta\right)\\ \mathbf{R} &= r_\eta\left(\mathbb{X}_\eta, \mathbb{X}_\eta\right)\end{aligned}$$

The hyperparameter set $\boldsymbol{\Omega}$ can be then estimated through a Bayesian approach and MCMC algorithms, however Conti and O'Hagan [152] showed that after integrating out hyperparameters $\mathbf{B}_\eta$ and $\boldsymbol{\Lambda}_\eta$ from Equation (5.30), the conditional predictive posterior distribution of surrogate model follows a $N_0 \times d$ dimensional matrix-variate T distribution for some unseen dataset $\mathbb{X}_{\eta,0}$ with N_0 datapoints::

$$p\left(\mathbb{Y}_0|\mathbb{Y}, \mathbb{X}_\eta, \mathbb{X}_{\eta,0}, \boldsymbol{\Psi}_\eta\right) \sim \mathrm{T}_{N_0,d}\left(\mathbf{M}_\eta^\star, \mathbf{R}_\eta^\star \otimes \hat{\boldsymbol{\Lambda}}_\eta, N-m\right) \tag{5.31}$$

with $N - m$ degrees of freedom (denotes as *dof* henceforth), and

$$\mathbf{M}_\eta^\star = \mu_\eta^\star\left(\mathbb{X}_{\eta,0}\right) \tag{5.32}$$

$$\mathbf{R}_\eta^\star = r_\eta^\star\left(\mathbb{X}_{\eta,0}, \mathbb{X}_{\eta,0}\right) \tag{5.33}$$

$$\begin{aligned}\mathbf{H}_\eta &= H_\eta\left(\mathbb{X}_\eta\right)\\ \hat{\mathbf{B}}_\eta &= \left(\mathbf{H}_\eta^\top \mathbf{R}^{-1} \mathbf{H}_\eta\right)^{-1} \mathbf{H}_\eta^\top \mathbf{R}^{-1} \mathbb{Y}\\ \hat{\boldsymbol{\Lambda}}_\eta &= (N-m)^{-1}\left(\mathbb{Y} - \mathbf{H}_\eta \hat{\mathbf{B}}_\eta\right)^\top \mathbf{R}^{-1}\left(\mathbb{Y} - \mathbf{H}_\eta \hat{\mathbf{B}}_\eta\right)\end{aligned}$$

where

$$\mu_\eta^\star\left(\mathbf{x}, \boldsymbol{\theta}\right) = \hat{\mathbf{B}}_\eta^\top H_\eta\left(\mathbf{x}, \boldsymbol{\theta}\right) + \left(\mathbb{Y} - \mathbf{H}_\eta \hat{\mathbf{B}}_\eta\right)^\top \mathbf{R}^{-1} r_\eta\left(\mathbb{X}_\eta, \left(\mathbf{x}, \boldsymbol{\theta}\right)\right) \tag{5.34}$$

$$r_\eta^\star\left((\mathbf{x},\boldsymbol{\theta})_i,(\mathbf{x},\boldsymbol{\theta})_j\right)=r_\eta\left((\mathbf{x},\boldsymbol{\theta})_i,(\mathbf{x},\boldsymbol{\theta})_j\right)-r_\eta\left((\mathbf{x},\boldsymbol{\theta})_i,\mathbb{X}_\eta\right)\mathbf{R}^{-1}r_\eta\left(\mathbb{X}_\eta,(\mathbf{x},\boldsymbol{\theta})_j\right)$$
$$+\left[S\left(\mathbf{x},\boldsymbol{\theta}\right)_i\right]^\top\left(\mathbf{H}_\eta^\top\mathbf{R}^{-1}\mathbf{H}_\eta\right)^{-1}\left[S\left(\mathbf{x},\boldsymbol{\theta}\right)_j\right] \tag{5.35}$$

$$S\left(\mathbf{x},\boldsymbol{\theta}\right)=H_\eta\left(\mathbf{x},\boldsymbol{\theta}\right)-\mathbf{H}_\eta^\top\mathbf{R}^{-1}r_\eta\left(\mathbb{X}_\eta,(\mathbf{x},\boldsymbol{\theta})\right) \tag{5.36}$$

Lastly, it only remains to estimate roughness parameters $\boldsymbol{\psi}_\eta$ in order to have a complete defined T distribution from Equations (5.31) to (5.33) which can then be used as a fast multivariate surrogate model for the TAMU thermal model. The estimation of these parameters is achieved by Bayesian means, whose conditional posterior distribution after proper integration is given by [152]:

$$p\left(\boldsymbol{\psi}_\eta\middle|\mathbb{Y},\mathbb{X}_\eta\right)\propto\left|\mathbf{R}\right|^{-\frac{d}{2}}\left|\mathbf{H}_\eta^\top\mathbf{R}^{-1}\mathbf{H}_\eta\right|^{-\frac{d}{2}}\left|\mathbb{Y}^\top\mathbf{G}\mathbb{Y}\right|^{-\frac{N-m}{2}}p\left(\boldsymbol{\psi}_\eta\right) \tag{5.37}$$

with

$$\mathbf{G}=\mathbf{R}^{-1}-\mathbf{R}^{-1}\mathbf{H}_\eta\left(\mathbf{H}_\eta^\top\mathbf{R}^{-1}\mathbf{H}_\eta\right)^{-1}\mathbf{H}_\eta^\top\mathbf{R}^{-1}$$

and i.i.d. ψ_i parameters with log-logistic prior distribution

$$p\left(\psi_i\right)\sim\text{Log Logistic}\left(1,1\right)\forall i\in\{1,\ldots,q+t\}$$

To build the surrogate model, a training dataset from the original TAMU thermal model is sampled using a LHS strategy to uniformly select design points from the control input and calibration parameters space. The lower and upper bounds for the control input space $\mathcal{X}$ was chosen as $\mathcal{X}_{\min}=\{30\,\text{W},80\,{}^{\text{mm}}/_{\text{s}}\}$, and $\mathcal{X}_{\max}=\{500\,\text{W},400\,{}^{\text{mm}}/_{\text{s}}\}$. These bounds were determined based on prior knowledge of the commercial metal L-PBF system specifications presented in Section 3.4. The lower and upper bounds for the calibration parameter space were chosen as $\mathcal{T}_{\min}=\{20\,\%,40\,\%,1\,{}^{\text{W}}/_{\text{m}\cdot\text{K}}\}$ and $\mathcal{T}_{\max}=\{70\,\%,90\,\%,25\,{}^{\text{W}}/_{\text{m}\cdot\text{K}}\}$. These bounds were specified by the AM researchers based on previous values reported in the literature to construct an initial region within which the true values of $\boldsymbol{\theta}$ are believed to lie.

A simulation data set of size $N=130$ was acquired with simulations ranging from 30 minutes

Table 5.5: Numerical results for validation of the multivariate Surrogate Model via 10-fold CV.

Melt pool QoI	Simulation Range	MAPE	MAPE-Sim. Range ratio
Depth	$51.3\,\mu\text{m}$	$2.01\,\mu\text{m}$	$4\,\%$
Width	$147.8\,\mu\text{m}$	$8.05\,\mu\text{m}$	$5\,\%$
Peak Temperature	$1284\,\text{K}$	$56.5\,\text{K}$	$4\,\%$

to 5 hours, and thus code parallelization was conducted on a 843-node high-performance supercomputer. Next, a MCMC Bayesian approach was used to estimate the roughness parameters $\boldsymbol{\psi}_\eta$ on Equation (5.37) with 50,000 MCMC iterations, 25% burn-in period and thinning every fifth sample. Figure 5.17 shows the histograms and kernel density estimates of the posterior distributions for these hyperparameters. Since resulting posterior distributions are very informative, their modes were used as the estimates for the roughness parameters on the surrogate model from Equations (5.31) to (5.33).

Finally, 10-fold CV was performed to validate and assess the performance of the surrogate model and the results are displayed in Figures 5.18a to 5.18c corresponding to the three model outputs: melt pool depth, width, and peak temperature, respectively. In the plots, the horizontal axes represent the outputs of the computer simulation model, while the vertical axes show the predicted outputs using the surrogate model with the bars representing confidence intervals for these predictions. In other words, the red line represents the ideal case with surrogate model predictions being in full agreement with computer model simulations.

It can be visually seen that the predictive performance of the surrogate model is satisfactory. For a quantitative assessment, the computed MAPE values for the three outputs are reported in Table 5.5, also indicating satisfactory performance. Next, the validated surrogate model is employed into the calibration framework from Equation (5.27).

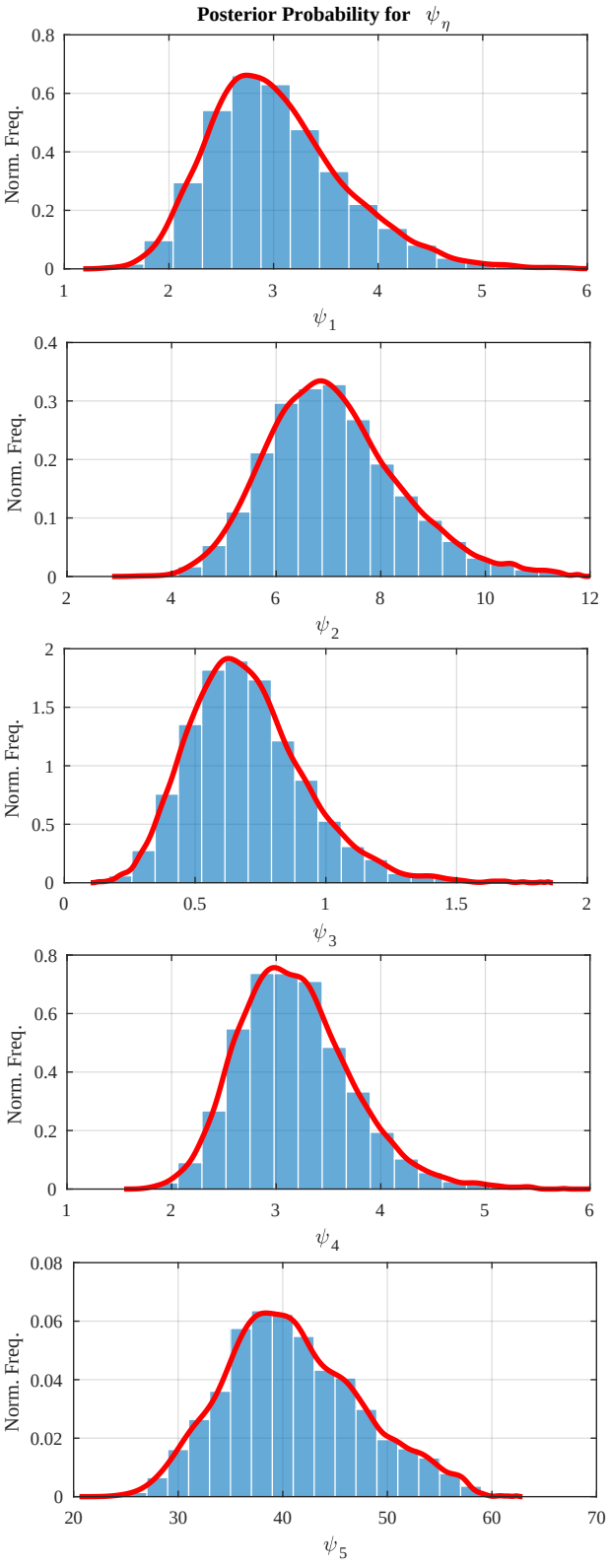

Figure 5.17: Histograms and kernel density estimates of the posterior distributions for roughness parameters of Surrogate Model.

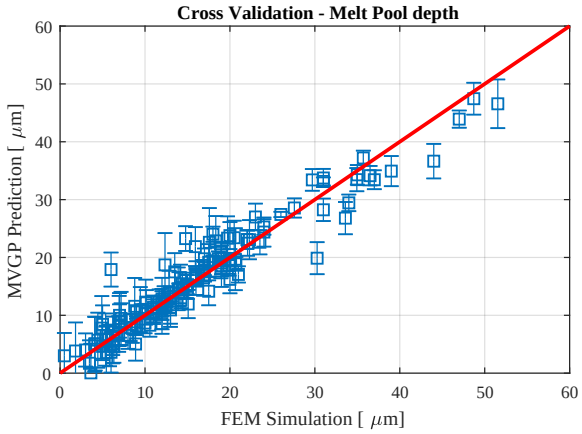

(a)

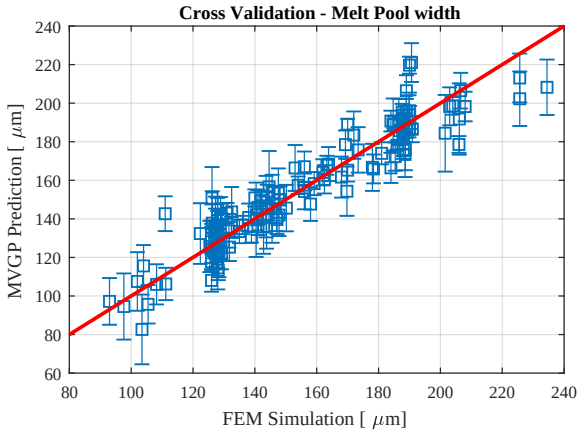

(b)

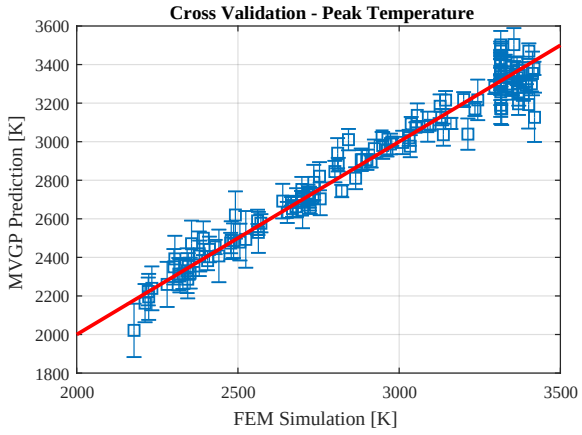

(c)

Figure 5.18: Validation of the multivariate Surrogate Model trained with simulations from the TAMU thermal model via 10-fold CV. **(a)** Validation of melt pool depth. **(b)** Validation of melt pool width. **(c)** Validation of melt pool peak temperature.

5.4.2 Calibration Model

Once the surrogate model has been adequately constructed, it can now be used in lieu of the the original computer model in Equation (5.27) to generate sufficiently large number of simulations needed to conduct calibration of parameters $\boldsymbol{\theta}$. Some of the steps in developing the following calibration procedure follow the work of Bhat et al. [153].

The definitions for discrepancy function $\boldsymbol{\delta}$ and error term $\boldsymbol{\epsilon}$ will take similar approaches as with their counterparts from last section generalized onto a multivariate stage. The discrepancy function is a d-dimensional GP, $\boldsymbol{\delta}(\cdot) \sim \mathrm{GP}_d(\mu_\delta, r_\delta \boldsymbol{\Lambda}_\delta)$ with a constant mean function equal to

$$\mu_\delta(\mathbf{x}) = \mathbf{0} \tag{5.38}$$

(note it returns a vector of d zeros) and anisotropic stationary squared exponential correlation function

$$r_\delta(\mathbf{x}_i, \mathbf{x}_j) = \exp\left[-(\mathbf{x}_i - \mathbf{x}_j)^\top \boldsymbol{\Phi}_\delta(\mathbf{x}_i - \mathbf{x}_j)\right] \tag{5.39}$$

where $\boldsymbol{\Phi}_\delta = \mathrm{diag}(\boldsymbol{\phi}_\delta)$ is a diagonal matrix of positive roughness parameters with $\boldsymbol{\phi}_\delta = [\phi_1, \ldots, \phi_q] \in \mathbb{R}_+^q$, and $\boldsymbol{\Lambda}_\delta = \mathrm{diag}(\boldsymbol{\sigma}_\delta)$ is a diagonal matrix with positive variances $\boldsymbol{\sigma}_\delta = [\sigma_1, \ldots, \sigma_d] \in \mathbb{R}_+^d$ denoting the correlation between model outputs.

The measurement error term is also modeled as a multivariate d-dimensional GP, $\boldsymbol{\epsilon}(\cdot) \sim \mathrm{GP}_d(\mu_\epsilon, r_\epsilon \boldsymbol{\Lambda}_\epsilon)$, with mean function equal to

$$\mu_\epsilon(\mathbf{x}) = \mathbf{0} \tag{5.40}$$

and correlation function given by the Kronecker delta function

$$r_\epsilon(\mathbf{x}_i, \mathbf{x}_j) = \begin{cases} 1 & \text{if } \mathbf{x}_i = \mathbf{x}_j \\ 0 & \text{if } \mathbf{x}_i \neq \mathbf{x}_j \end{cases} \tag{5.41}$$

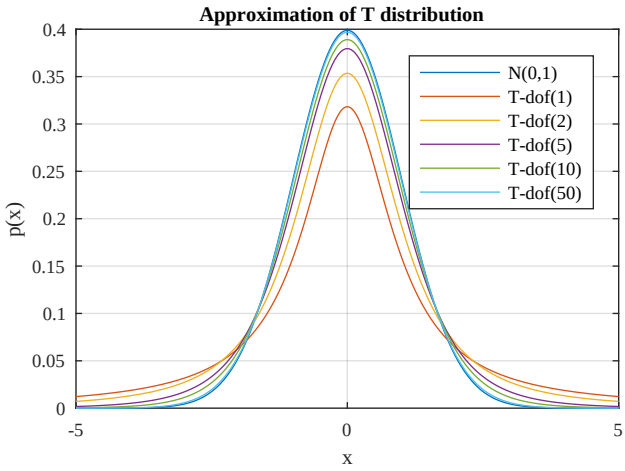

Figure 5.19: Approximation of T probability distributions to a normal distribution by variation of their degrees of freedom.

and noise matrix $\mathbf{\Lambda}_\epsilon = \text{diag}\,(\boldsymbol{\tau}_\epsilon)$ with positive noise variances $\boldsymbol{\tau}_\epsilon = [\tau_1, \ldots, \tau_d] \in \mathbb{R}^d_+$.

Notice that up to this point, the definitions of the components in Equation (5.27) involve that the model results from the summation of three multivariate random processes: a T Process from the Surrogate Model, and two GPs from the discrepancy and the error functions. Thus, the multivariate T process is approximated to a GP, so that this mentioned summation in the RHS of Equation (5.27) becomes another GP thanks to the property of addition of statistically independent Gaussian random variables [154]. This approximation can be justified by using an analogous case in a univariate setting as shown in Figure 5.19. The plot presents several univariate T distributions with different dof, in addition to a standard Normal distribution, and it can be seen that as the value of dof increases (values larger than 10), the T distributions approximate perfectly to the standard Normal distribution. Therefore, if a T distribution is defined with dof equal to $N - m$ with $N > m$ for some $N, m \in \mathbb{N}$, then it can be approximated to a Normal distribution as long as the value $N - m$ is relatively large. This is the case specially in the current context where the size of the training dataset for surrogate model *N* is relative larger than the dimension *m* from the mean function linear regression from Equation (5.28). Therefore, with this approximation, the calibration model is fully defined by the set of hyperparameters $\boldsymbol{\Omega} = \{\boldsymbol{\theta}, \boldsymbol{\phi}_\delta, \boldsymbol{\sigma}_\delta, \boldsymbol{\tau}_\epsilon\}$

In order to build the calibration model, the experimental dataset of size *n* will be collected and denoted as

$$\mathbb{X} = \begin{bmatrix} \mathbf{x}_1^\top \\ \mathbf{x}_2^\top \\ \vdots \\ \mathbf{x}_n^\top \end{bmatrix}, \ \mathbb{Z} = \begin{bmatrix} \mathbf{Z}(\mathbf{x}_1) \\ \mathbf{Z}(\mathbf{x}_2) \\ \vdots \\ \mathbf{Z}(\mathbf{x}_n) \end{bmatrix}$$

However for implementation purposes, the datasets will be rearranged by stacking each vector $\mathbf{Z}(\mathbf{x}_i)$ and forming a single column vector with length $n \cdot d$, which result in the following likelihood function given the definitions (and approximation) for the components in Equation (5.27):

$$p(\mathbb{Z}|\mathbb{Y}, \mathbb{X}_\eta, \mathbb{X}, \boldsymbol{\Omega}) \sim \mathrm{N}_{n \cdot d}(\mathbf{M}, \boldsymbol{\Sigma}) \tag{5.42}$$

where

$$\begin{aligned}
\mathbb{Z} &= [Z_{1,1}, \ldots, Z_{1,d}, Z_{2,1}, \ldots, Z_{2,d}, \ldots, Z_{n,1}, \ldots, Z_{n,d}]^\top \in \mathbb{R}^{n \cdot d} \\
\mathbf{M} &= \left[\mu_\eta^\star(\mathbb{X}, \boldsymbol{\theta})\right]^\top \in \mathbb{R}^{n \cdot d} \\
\boldsymbol{\Sigma} &= \mathbf{R}_\eta \otimes \hat{\boldsymbol{\Lambda}}_\eta + \mathbf{R}_\delta \otimes \boldsymbol{\Lambda}_\delta + \mathbf{R}_\epsilon \otimes \boldsymbol{\Lambda}_\epsilon \in \mathbb{R}_+^{n \cdot d, n \cdot d} \\
\mathbf{R}_\eta &= r_\eta^\star((\mathbb{X}, \boldsymbol{\theta}), (\mathbb{X}, \boldsymbol{\theta})) \in \mathbb{R}_+^{n,n} \\
\mathbf{R}_\delta &= r_\delta(\mathbb{X}, \mathbb{X}) \in \mathbb{R}_+^{n,n} \\
\mathbf{R}_\epsilon &= r_\epsilon(\mathbb{X}, \mathbb{X}) \in \mathbb{R}_+^{n,n}
\end{aligned}$$

The parameters are estimated under a Bayesian procedure, and thus, prior distributions for the hyperparameters are selected as:

$$\begin{aligned}
p(\theta_i) &\sim \mathrm{U}(\mathcal{T}_{\min,i}, \mathcal{T}_{\max,i}) \, \forall i \in \{1, \ldots, t\} \\
p(\phi_i) &\sim \mathrm{Log\,Logistic}(1, 1) \, \forall i \in \{1, \ldots, q\}
\end{aligned}$$

$$p(\sigma_i) \sim \mathrm{IG}(2,1) \, \forall i \in \{1,\ldots,d\}$$
$$p(\tau_i) \sim \mathrm{IG}(2,1) \, \forall i \in \{1,\ldots,d\}$$

which follow same guidelines as with the previous case. Priors for the calibration parameters θ_i are all uniform and hence non-informative to avoid bias in estimation, and since no information beyond the suggested lower and upper bounds were available. For the roughness parameters ϕ_i, log-logistic priors were used as recommended by [152]. For the variance parameters σ_i and τ_i, inverse gamma priors are selected because they represent conjugate priors for the multivariate normal likelihood function in Equation (5.42).

The posteriors distributions of hyperparameter set $\boldsymbol{\Omega}$ can be calculated via MCMC algorithms, and special importance is given to those posterior estimates for calibration parameters $\boldsymbol{\theta}$. Furthermore, the calibrated model can then be used in a prediction stage following the predictive posterior distribution for unseen input dataset $\mathbb{X}_0$:

$$p(\mathbb{Z}_0|\mathbb{Z},\mathbb{Y},\mathbb{X}_\eta,\mathbb{X},\mathbb{X}_0,\boldsymbol{\Omega}_\eta,\boldsymbol{\Omega}) \sim \mathrm{N}_{n_0}(\boldsymbol{\mu}_0,\boldsymbol{\Sigma}_0) \tag{5.43}$$

where the mean vector is given by

$$\boldsymbol{\mu}_0 = \mathbf{M}_0 + \boldsymbol{\Sigma}_{\mathrm{pred}}\boldsymbol{\Sigma}^{-1}(\mathbb{Z}-\mathbf{M}) \tag{5.44}$$

with

$$\mathbf{M}_0 = \left[\mu_\eta^\star(\mathbb{X}_0,\theta)\right]^\top \in \mathbb{R}^{n_0\cdot d}$$
$$\boldsymbol{\Sigma}_{\mathrm{pred}} = \mathbf{R}_{\eta,0} \otimes \hat{\boldsymbol{\Lambda}}_\eta + \mathbf{R}_{\delta,0} \otimes \boldsymbol{\Lambda}_\delta \in \mathbb{R}^{n_0\cdot d, n\cdot d}$$
$$\mathbf{R}_{\eta,0} = \left[r_\eta^\star((\mathbb{X}_0,\boldsymbol{\theta}),(\mathbb{X},\boldsymbol{\theta}))\right] \in \mathbb{R}^{n_0,n}$$
$$\mathbf{R}_{\delta,0} = \left[r_\delta(\mathbb{X}_0,\mathbb{X})\right] \in \mathbb{R}^{n_0,n}$$

and cross-covariance matrix

$$\boldsymbol{\Sigma}_0 = \boldsymbol{\Sigma}_{\text{cal}} - \boldsymbol{\Sigma}_{\text{pred}} \boldsymbol{\Sigma}^{-1} \boldsymbol{\Sigma}_{\text{pred}}^{\top} \tag{5.45}$$

where

$$\begin{aligned}
\boldsymbol{\Sigma}_{\text{cal}} &= \mathbf{R}_{\eta,1} \otimes \hat{\boldsymbol{\Lambda}}_{\eta} + \mathbf{R}_{\delta,1} \otimes \boldsymbol{\Lambda}_{\delta} + \mathbf{R}_{\epsilon,1} \otimes \boldsymbol{\Lambda}_{\epsilon} \in \mathbb{R}^{n_0 \cdot d, n_0 \cdot d} \\
\mathbf{R}_{\eta,1} &= \left[r_{\eta}^{\star} \left((\mathbb{X}_0, \boldsymbol{\theta}), (\mathbb{X}_0, \boldsymbol{\theta}) \right) \right] \in \mathbb{R}^{n_0, n_0} \\
\mathbf{R}_{\delta,1} &= \left[r_{\delta} \left(\mathbb{X}_0, \mathbb{X}_0 \right) \right] \in \mathbb{R}^{n_0, n_0} \\
\mathbf{R}_{\epsilon,1} &= \left[r_{\epsilon} \left(\mathbb{X}_0, \mathbb{X}_0 \right) \right] \in \mathbb{R}^{n_0, n_0}
\end{aligned}$$

The final stage prior to fit the calibration model is the collection of the experimental dataset. A total of $n = 24$ different configurations of $\mathbf{x}$ were determined following a LHS design. Single tracks of length $20\,\text{mm}$ were fabricated on a $30\,\mu\text{m}$ powder-bed using the L-PBF system explained in Section 3.4. The raw Ti-6Al-4V powder was produced by LPW Technology and the single tracks were printed on a substrate made of Ti-6Al-4V as well. The single tracks were subsequently cut at 4 different points along their length with a Buehler precision saw and mounted for cross-section analysis. Metallographic grinding was performed with silicon carbide papers (320 to 600 grit size) followed by manual polishing with $1\,\mu\text{m}$ diamond suspension and final precision polishing with colloidal silica suspension. To make melt pool boundary lines more visible, chemical etching was performed using a 3:1 volume mixture of HCl and HNO_3 solution.

Melt pool depth and width were then measured using optical microscopy (Nikon Optiphot - POL) and verified with scanning electron microscopy (FEG-SEM/FIB TESCAN LYRA3). A sample SEM image used for measuring the melt pool depth and width is shown in Figure 5.20. Micrographs were taken at all 4 cross sections for each single track, and their average is used in dataset $\mathbb{Z}$ in order to fit the statistical calibration model.

Regarding peak temperature, experimental measurements for this QoI were taken using the pyrometer that was customized and installed into the L-PBF system. Section 3.4 presents more details about the pyrometer's specifications, field of view, and data samples.

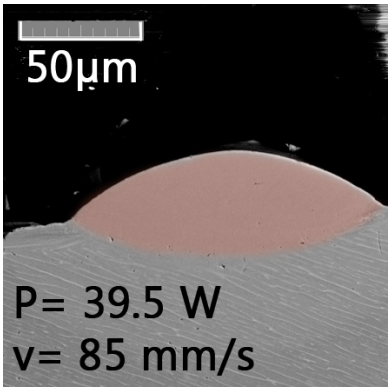

Figure 5.20: SEM image of a L-PBF single-track cross section used to measure melt pool depth and width.

Table 5.6: Estimates of the calibration parameters for the TAMU thermal model.

Calibration Parameter	Mean	Mode	Std. Dev.
Powder-bed porosity, θ_1	0.423	0.400	0.112
Laser absorptivity, θ_2	0.782	0.782	0.066
Coefficient of thermal conductivity of the liquid, θ_3	6.727	6.709	0.922

Similar to the Surrogate Model, a Bayesian procedure through MCMC was used to compute the posterior distributions for the hyperparameter set $\mathbf{\Omega}$. Figure 5.21 shows the histograms and kernel density estimates for these parameters after 100,000 MCMC iterations with 25% burn-in period and thinning every fifth sample. In the plots, unimodal and well-informative posteriors are observed for all of the calibration parameters with θ_1 and θ_3 showing symmetric density functions and θ_2 showing a density function skewed to the right. Table 5.6 reports the posterior mean, mode, and standard deviation for the posterior distributions of the calibration parameters.

Porosity, θ_1, is used to calculate the effective thermo-physical properties of the powder-bed (i.e., thermal conductivity and density). It was observed during simulations that by changing the porosity from 0.3 to 0.5 the thermal conductivity of the powder changes up to $2\,{}^{\mathrm{W}}/_{\mathrm{m}\cdot\mathrm{K}}$, which leads to an insignificant change in the thermal history and only a few microns change in the melt pool size. Thus, by considering the variability in experimental measurements for melt pool dimensions,

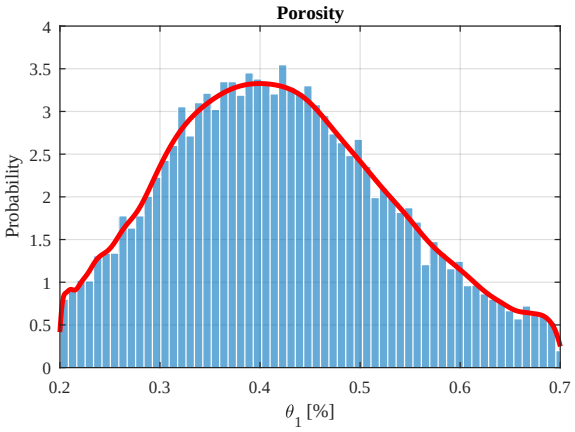

(a)

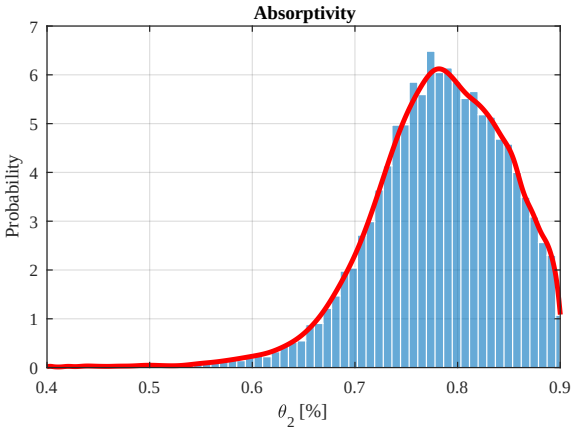

(b)

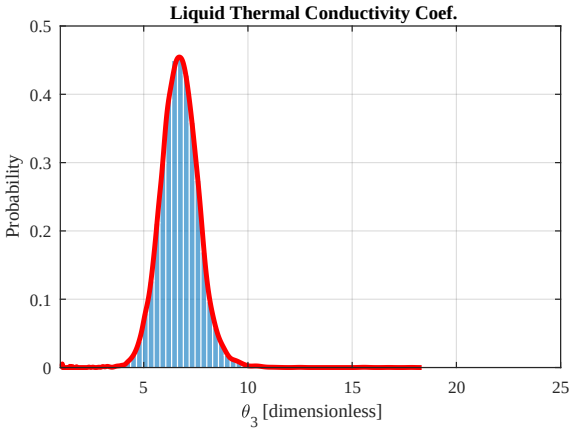

(c)

Figure 5.21: Histograms and kernel density estimates of the posterior distribution for calibration parameters for the TAMU thermal model. **(a)** Powder-bed porosity. **(b)** Laser absorptivity. **(c)** Thermal conductivity of the liquid.

this change becomes negligible, and the wide nature of the posterior distribution for θ_1 is physically consistent. Furthermore, a posterior mean of 0.423% is reasonable since it agrees with the reported range of porosity for similar powder sizes and layer thicknesses, see [139, 155].

The posterior distribution of absorptivity (θ_2) shows a more informative posterior distribution with mean of 0.782. This value demonstrates reasonable agreement with reported experimental results in the literature [156, 157]. However, considering the difficulties associated with experimentally measuring absorptivity due to its dependence on multiple parameters (i.e., wavelength, temperature, oxidation, powder size, powder distribution, powder porosity), these experimental results might involve high uncertainty. Therefore, the estimated distribution for absorptivity is confidently consistent with the underlying physical phenomena controlling the interactions between the laser and the powder bed.

The narrow range of the posterior distribution of θ_3 can be attributed to its significant effect on the thermal profile and the melt pool size. A unit increase in the liquid thermal conductivity coefficient might lead to a change on the order of $100\,\mathrm{K}$ in the thermal history and in a change between $5\,\mu\mathrm{m}$ to $10\,\mu\mathrm{m}$ in the melt pool size. Additionally, if extremely high values are used for this parameter, the applied energy would be rapidly transferred to the surroundings and the energy input will reduce, thus the melt pool peak temperature would decrease in an unrealistic manner. Therefore, only a small region of this parameter results in physically meaningful simulations, explaining the narrow posterior distribution.

Next, we use the predictive distribution from Equations (5.43) to (5.45) to assess the performance of the calibrated model via a 6-fold cross validation. Figure 5.22 displays the results of the 6-fold cross validation for each of the three QoIs. In the plots, the horizontal axes represent experimental measurements, while the vertical axes are the predicted outputs using the calibrated model with the bars representing the confidence intervals for the predictions. In other words, each point on the plots compares the experiment versus the calibrated model prediction, and the red straight line is a reference line representing ideal predictions.

Upon visual inspection, the plots qualitatively show acceptable predictive performance for melt

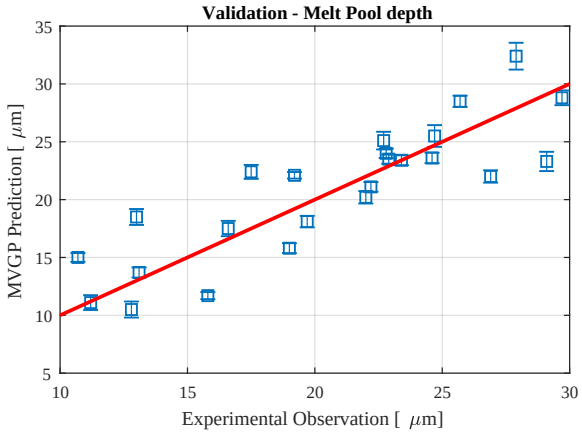

(a)

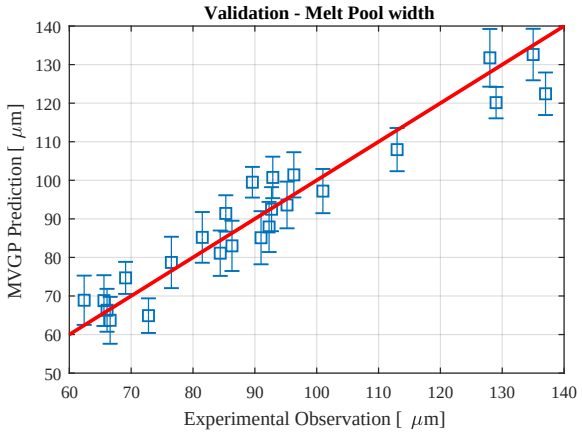

(b)

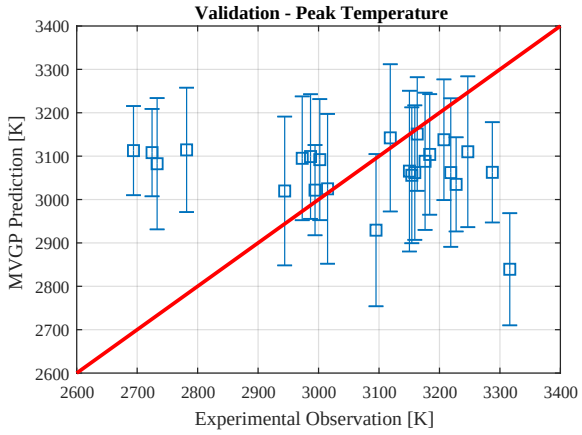

(c)

Figure 5.22: Validation of the calibration framework for the TAMU thermal model simulations via 6-fold CV. **(a)** Validation of melt pool depth. **(b)** Validation of melt pool width. **(c)** Validation of melt pool peak temperature.

Table 5.7: Numerical results for validation of the calibrated TAMU thermal model via 6-fold CV.

Melt pool QoI	MAPE	MAPE-Sim. Range ratio
Depth	$2.42\,\mu\mathrm{m}$	$5\,\%$
Width	$4.93\,\mu\mathrm{m}$	$3\,\%$
Peak Temperature	$159.5\,\mathrm{K}$	$12\,\%$

pool depth and melt pool width, but less accurate for predictions of peak temperature, particularly in the case with too low and too high values. Quantitatively, the error metric MAPE for each output are reported in Table 5.7. Note that MAPE for melt pool depth and width are relatively low compared to the full range of simulations: 5% and 3%, respectively. Hence, these results show that the calibration model is effectively correcting the simulation model output when using Equation (5.43). However, the predictions for melt pool peak temperature show a higher value of MAPE (12% of the simulation range) compared to the predictions for melt pool depth and width. This might be due to the inherent high uncertainty associated with experimental temperature measurements using contactless temperature measurement through pyrometry [158]. The uncertainty in the temperature data can be measured by computing its standard deviation, which is equal to $3.03\,\mu\mathrm{m}$, $8.14\,\mu\mathrm{m}$, and $306.3\,^{\circ}\mathrm{C}$, respectively for melt pool depth, width and peak temperature. Therefore, the relative high value for standard deviation for the data of peak temperature could likely be the explanation for the high MAPE value associated with the predictions.

This concludes the main body of the dissertation which dealt with presenting different settings where application of UQ methodologies into L-PBF problems improved the understanding, applicability, usability, and qualifications of the process. In the last chapter, a summary of implications, conclusions and future work remarks will be presented since UQ research in L-PBF processes is of paramount importance for the technology to mature into a competitive stage.

6. SUMMARY

6.1 Contributions of the Dissertation

At the culmination of this dissertation, new insights about the L-PBF process have been learned through the application of formal UQ methodologies which help on the further development of this manufacturing technology. In particular, the following contributions resulted as consequence of the dissertation:

- Increase in the understanding about presence of porosity within printed parts as a function of processing parameters. This will provide guidance and direction on how to avoid certain processing parameters or design parts that are required to have a certain level of porosity within their structure.

- Ability to implement and build surrogate models in order to replace computational resource-intensive L-PBF simulation models. This will provide practical capabilities for accomplishing high-level optimization of the L-PBF process while still make use of simulations and insights that computational models provide.

- Increase in the understanding of L-PBF thermal behavior by identification of processing windows for conduction mode and keyhole melting controlled regimes as functions of processing parameters. These windows will provide guidance and direction on how to avoid specific regimes during design and fabrication of parts as well as ensure better part quality.

- Enable utilization of ICME platforms by formal statistical calibration and validation of different L-PBF computer models. This will increase the applicability of these models as resources for researchers and practitioners to be used during part design and fabrication.

- Quantification of the uncertainty initiated from different processing parameters and propagated into several L-PBF QoIs. The characterization of this uncertain behavior will con-

tribute to the researchers and practitioners towards understanding issues about repeatability in L-PBF.

- Identification and quantification of the influence of different processing parameters in melt pool characteristics. This will provide insights on how and what parameter (or combination of parameters) to focus on at the design phase of the manufacturing process.

- The generalization of different UQ methodologies into multivariate cases will expand the applicability of these types of methodologies to a more broad range of fields, even outside of L-PBF or AM, since multivariate approaches increase the robustness of the analysis in any application due to the inclusion of different statistical correlations between model outputs as well as between model inputs.

6.2 Conclusions of the Dissertation

Despite the current poor understanding of different physical phenomena occurring during the L-PBF AM processes and the low repeatability achieved by this technologies, researchers and scientists have not directed their focus towards the existing research gap involving formal analysis of uncertainty in these processes.

In this dissertation, a systematic application of UQ methodologies is proposed and successfully implemented to different QoIs in order to improve understanding of the L-PBF manufacturing process, assess and quantify uncertainty from different sources, and reduce them by taking educated decisions based on the results from the application of these UQ tools.

A variety of methodologies and procedures are employed throughout this dissertation, which derive from scientific fields comprising applied Mathematics, Statistics, Probability, Data Science and Machine Learning. Specifically, popular statistical models are used to conduct several studies on different L-PBF QoIs, these include Gaussian Processes, generalized Polynomial Chaos Expansions and Global Sensitivity Analysis, which have a history of proven success in previous applications to several other fields of study.

Furthermore, applicability and usability of UQ approaches are clearly defined for both lines of

research in L-PBF: computer models or experimental work. These UQ frameworks are formally and successfully validated, and hence, the reader and the L-PBF community in general are recommended to make use of these available tools for their respective research and work. In turn, this will help L-PBF AM technologies to be seen more appealing and competitive when compared to traditional methods and eventually be regarded as the main manufacturing solution for industry, governments and academia.

6.3 Directions for Future Research

There are several opportunities and directions for future work involving L-PBF processes. These new directions involve both application of UQ methodologies as well as new paths towards increasing understanding and control of the process. One of the primary focus of future research is a complete multi-model ICME platform of L-PBF by coupling different physics-based models. In layman's terms, it is desired to understand the behavior across L-PBF, where the output from one model represents the input to another model throughout the AM process chain. These series of models will account different scales within the process, and the objective is to be able to go from manufacturing processing parameters to microstructure evolution and mechanical performance predictions while quantifying uncertainty in parallel. This type of analysis about uncertainty through coupled physics-based models is a crucial topic towards accelerating qualification and certification of AM-fabricated parts.

Furthermore, application of UQ methodologies for L-PBF will benefit from spatial-temporal analysis in a multivariate framework since the L-PBF process is dynamic and constantly changing due to the very rapid physics within its operating principle. Therefore, methodologies that include time series analysis along different scales of the process are attractive research paths for the community. Additionally, adaptive sampling techniques to accelerate and improve the predictive performance of the statistical models will also be beneficial in order to optimize the amount of data (from expensive experiments or costly simulation runs) required to fit and validate these statistical models.

Finally, since experimental measurements will always be necessary to formally validate the-

ories and hypotheses, development on measurement instruments centered towards L-PBF applications are required to improve research techniques and capabilities, accuracy in validations and predictions, or for smarter process control, automation, monitoring and quality control.

REFERENCES

[1] *Additive manufacturing – General principles – Terminology*, ISO/ASTM Std. 52 900 (ASTM F2792), December 2015. [Online]. Available: https://www.iso.org/standard/69669.html

[2] W. J. Sames, F. List, S. Pannala, R. R. Dehoff, and S. S. Babu, "The metallurgy and processing science of metal additive manufacturing," *International Materials Reviews*, vol. 61, no. 5, pp. 315–360, 2016.

[3] T. Wohlers, W. Associates, R. Campbell, and T. Caffrey, *Wohlers Report 2016: 3D Printing and Additive Manufacturing State of the Industry : Annual Worldwide Progress Report*., Wohlers Associates, 2016.

[4] G. Tapia and A. Elwany, "A review on process monitoring and control in metal-based additive manufacturing," *Journal of Manufacturing Science and Engineering*, vol. 136, no. 6, p. 060801, 2014.

[5] T. Kellner. (2017, Jul.) Mind meld: How GE and a 3D-printing visionary joined forces. General Electric. Last accessed: April 16, 2018. [Online]. Available: https://www.ge.com/reports/mind-meld-ge-3d-printing-visionary-joined-forces/

[6] 3D Systems, Inc. Topology optimization and direct metal 3D printing (DMP) in GE aircraft engine bracket challenge. Last accessed: April 16, 2018. [Online]. Available: https://www.3dsystems.com/learning-center/case-studies/topology-optimization-and-dmp-combine-meet-ge-aircraft-engine-bracket

[7] Frustum Inc. Frustum GE bracket challenge case study. Last accessed: April 16, 2018. [Online]. Available: https://www.frustum.com/frustum-ge-bracket-challenge-case-study

[8] S. A. Goehrke. (2017, Mar.) Topology optimization eases additive manufacturing design

– a few questions for: Frustum. 3DR Holdings. Last accessed: April 16, 2018. [Online]. Available: https://3dprint.com/169436/a-few-questions-for-frustum/

[9] Stryker Corporation. Knee – Implants. Last accessed: April 16, 2018. [Online]. Available: https://www.stryker.com/us/en/portfolios/orthopaedics/joint-replacement/knee.html

[10] D. Gu, W. Meiners, K. Wissenbach, and R. Poprawe, "Laser additive manufacturing of metallic components: materials, processes and mechanisms," *International materials reviews*, vol. 57, no. 3, pp. 133–164, 2012.

[11] I. Gibson, D. W. Rosen, and B. Stucker, *Additive manufacturing technologies: 3D Printing, rapid prototyping, and direct digital manufacturing*, 2nd ed., New York, NY: Springer, 2015.

[12] Wikipedia contributors. (2018, Jan.) Selective laser sintering. Wikimedia Foundation Inc. Last accessed: April 16, 2018. [Online]. Available: https://en.wikipedia.org/wiki/Selective_laser_sintering

[13] K. K. Ma. (2014, Jun.) Researchers develop efficient approach to manufacture 3D metal parts. Lawrence Livermore National Laboratory. Last accessed: April 16, 2018. [Online]. Available: https://www.llnl.gov/news/researchers-develop-efficient-approach-manufacture-3d-metal-parts

[14] S. J. Wolff, S. Lin, E. J. Faierson, W. K. Liu, G. J. Wagner, and J. Cao, "A framework to link localized cooling and properties of directed energy deposition (DED)-processed Ti-6Al-4V," *Acta Materialia*, vol. 132, pp. 106–117, 2017.

[15] S. Sun, L. Zheng, Y. Liu, J. Liu, and H. Zhang, "Selective laser melting of Al-Fe-V-Si heat-resistant aluminum alloy powder: modeling and experiments," *The International Journal of Advanced Manufacturing Technology*, vol. 80, no. 9-12, pp. 1787–1797, 2015.

[16] D. L. Bourell, M. C. Leu, and D. W. Rosen, "Roadmap for additive manufacturing: identifying the future of freeform processing," The University of Texas at Austin, Austin, TX,

Tech. Rep., 2009. [Online]. Available: https://wohlersassociates.com/roadmap2009A.pdf

[17] Energetics Incorporated, "Measurement science roadmap for metal-based additive manufacturing," National Institute of Standards and Technology, Columbia, MD, Workshop Summary Rep., May 2013. [Online]. Available: https://www.nist.gov/sites/default/files/documents/el/isd/NISTAdd_Mfg_Report_FINAL-2.pdf

[18] National Research Council, *Integrated Computational Materials Engineering: A Transformational Discipline for Improved Competitiveness and National Security*., Washington, DC: The National Academies Press, 2008.

[19] G. Tapia, S. Khairallah, M. Matthews, W. E. King, and A. Elwany, "Gaussian process-based surrogate modeling framework for process planning in laser powder-bed fusion additive manufacturing of 316L stainless steel," *The International Journal of Advanced Manufacturing Technology*, vol. 94, no. 9, pp. 3591–3603, 2018.

[20] M. Agarwala, D. Bourell, J. Beaman, H. Marcus, and J. Barlow, "Direct selective laser sintering of metals," *Rapid Prototyping Journal*, vol. 1, no. 1, pp. 26–36, 1995.

[21] M. Van Elsen, "Complexity of selective laser melting: a new optimisation approach," Ph.D. dissertation, Katholieke Universiteit Leuven, Leuven, Belgium, Jan. 2007.

[22] *Lasers and laser-related equipment – Test methods for laser beam widths, divergence angles and beam propagation ratios – Part 1: Stigmatic and simple astigmatic beams*, ISO Std. 11 146, Rev. 1, 2005. [Online]. Available: https://www.iso.org/standard/33625.html

[23] K. Grebici, Y. Goh, and C. McMahon, "Uncertainty and risk reduction in engineering design embodiment processes," in *Proc. 10th International Design Conference*, Dubrovnik, Croatia, May 2008.

[24] D. E. Berlyne, "A theory of human curiosity," *British Journal of Psychology*, vol. 45, no. 3, pp. 180–191, 1954.

[25] A. Abdulle and G. Wanner, "200 years of least squares method," *Elemente der Mathematik*, vol. 57, no. 2, pp. 45–60, 2002.

[26] R. C. Smith, *Uncertainty quantification: theory, implementation, and applications*., SIAM, 2013.

[27] J. M. Murphy, D. M. Sexton, D. N. Barnett, G. S. Jones, M. J. Webb, M. Collins, and D. A. Stainforth, "Quantification of modelling uncertainties in a large ensemble of climate change simulations," *Nature*, vol. 430, no. 7001, pp. 768–772, 2004.

[28] R. Furnstahl, D. Phillips, and S. Wesolowski, "A recipe for EFT uncertainty quantification in nuclear physics," *Journal of Physics G: Nuclear and Particle Physics*, vol. 42, no. 3, p. 034028, 2015.

[29] G. Lin, D. W. Engel, and P. W. Eslinger, "Survey and evaluate uncertainty quantification methodologies," Pacific Northwest National Laboratory, Richland, WA, Tech. Rep. PNNL-20914, Feb. 2012.

[30] A. Hawkins-Daarud, S. Prudhomme, K. G. van der Zee, and J. T. Oden, "Bayesian calibration, validation, and uncertainty quantification of diffuse interface models of tumor growth," *Journal of Mathematical Biology*, vol. 67, no. 6-7, pp. 1457–1485, 2013.

[31] L. Kilian and T. Zha, "Quantifying the uncertainty about the half-life of deviations from PPP," *Journal of Applied Econometrics*, vol. 17, no. 2, pp. 107–125, 2002.

[32] W. E. King, A. Arsenlis, C. Tong, and W. L. Oberkampf, "Uncertainties in predictions of material performance using experimental data that is only distantly related to the system of interest," in *Uncertainty Quantification in Scientific Computing*, 10th IFIP WG 2.5 Working Conference., Boulder, CO: Springer, Aug. 2011, pp. 294–311.

[33] A. Chernatynskiy, S. R. Phillpot, and R. LeSar, "Uncertainty quantification in multiscale simulation of materials: A prospective," *Annual Review of Materials Research*, vol. 43, pp.

157–182, 2013.

[34] J. H. Panchal, S. R. Kalidindi, and D. L. McDowell, "Key computational modeling issues in integrated computational materials engineering," *Computer-Aided Design*, vol. 45, no. 1, pp. 4–25, 2013.

[35] Z. Hu and S. Mahadevan, "Uncertainty quantification in prediction of material properties during additive manufacturing," *Scripta Materialia*, vol. 135, pp. 135–140, 2017.

[36] W. E. King, H. D. Barth, V. M. Castillo, G. F. Gallegos, J. W. Gibbs, D. E. Hahn, C. Kamath, and A. M. Rubenchik, "Observation of keyhole-mode laser melting in laser powder-bed fusion additive manufacturing," *Journal of Materials Processing Technology*, vol. 214, no. 12, pp. 2915–2925, 2014.

[37] H. Gu, H. Gong, D. Pal, K. Rafi, T. Starr, and B. Stucker, "Influences of energy density on porosity and microstructure of selective laser melted 17-4PH stainless steel," in *Proc. 2013 Solid Freeform Fabrication Symposium*, Austin, TX, 2013, pp. 474–489.

[38] B. Zhang, Y. Li, and Q. Bai, "Defect formation mechanisms in selective laser melting: A review," *Chinese Journal of Mechanical Engineering*, vol. 30, no. 3, pp. 515–527, 2017.

[39] C. Weingarten, D. Buchbinder, N. Pirch, W. Meiners, K. Wissenbach, and R. Poprawe, "Formation and reduction of hydrogen porosity during selective laser melting of AlSi10Mg," *Journal of Materials Processing Technology*, vol. 221, pp. 112–120, 2015.

[40] S. Tammas-Williams, P. J. Withers, I. Todd, and P. B. Prangnell, "The effectiveness of hot isostatic pressing for closing porosity in titanium parts manufactured by selective electron beam melting," *Metallurgical and Materials Transactions A*, vol. 47, no. 5, pp. 1939–1946, 2016.

[41] N. T. Aboulkhair, N. M. Everitt, I. Ashcroft, and C. Tuck, "Reducing porosity in AlSi10Mg parts processed by selective laser melting," *Additive Manufacturing*, vol. 1, pp. 77–86, 2014.

[42] G. Tapia, A. Elwany, and H. Sang, "Prediction of porosity in metal-based additive manufacturing using spatial gaussian process models," *Additive Manufacturing*, vol. 12, pp. 282–290, 2016.

[43] G. Kasperovich, J. Haubrich, J. Gussone, and G. Requena, "Correlation between porosity and processing parameters in TiAl6V4 produced by selective laser melting," *Materials & Design*, vol. 105, pp. 160–170, 2016.

[44] C. Teng, H. Gong, A. Szabo, J. Dilip, K. Ashby, S. Zhang, N. Patil, D. Pal, and B. Stucker, "Simulating melt pool shape and lack of fusion porosity for selective laser melting of cobalt chromium components," *Journal of Manufacturing Science and Engineering*, vol. 139, no. 1, p. 011009, 2017.

[45] R. Li, J. Liu, Y. Shi, L. Wang, and W. Jiang, "Balling behavior of stainless steel and nickel powder during selective laser melting process," *The International Journal of Advanced Manufacturing Technology*, vol. 59, no. 9-12, pp. 1025–1035, 2012.

[46] N. K. Tolochko, S. E. Mozzharov, I. A. Yadroitsev, T. Laoui, L. Froyen, V. I. Titov, and M. B. Ignatiev, "Balling processes during selective laser treatment of powders," *Rapid Prototyping Journal*, vol. 10, no. 2, pp. 78–87, 2004.

[47] D. Gu and Y. Shen, "Balling phenomena in direct laser sintering of stainless steel powder: Metallurgical mechanisms and control methods," *Materials & Design*, vol. 30, no. 8, pp. 2903–2910, 2009.

[48] P. Oyar, "Laser sintering technology and balling phenomenon," *Photomedicine and laser surgery*, 2017.

[49] R. Li, Y. Shi, Z. Wang, L. Wang, J. Liu, and W. Jiang, "Densification behavior of gas and water atomized 316L stainless steel powder during selective laser melting," *Applied Surface Science*, vol. 256, no. 13, pp. 4350–4356, 2010.

[50] H. Atkinson and S. Davies, "Fundamental aspects of hot isostatic pressing: An overview," *Metallurgical and Materials Transactions A*, vol. 31, no. 12, pp. 2981–3000, 2000.

[51] K. Kempen, L. Thijs, B. Vrancken, S. Buls, J. Van Humbeeck, and J. Kruth, "Producing crack-free, high density M2 HSS parts by selective laser melting: pre-heating the baseplate," in *Proc. 2013 Solid Freeform Fabrication Symposium*, Austin, TX, 2013, pp. 131–139.

[52] K. Darvish, Z. Chen, and T. Pasang, "Reducing lack of fusion during selective laser melting of CoCrMo alloy: Effect of laser power on geometrical features of tracks," *Materials & Design*, vol. 112, pp. 357–366, 2016.

[53] L. Michalski, K. Eckersdorf, J. Kucharski, and J. McGhee, *Temperature measurement*, 2nd ed., Chichester, UK: John Wiley & Sons, 2001.

[54] P. R. Childs, *Practical temperature measurement*, 1st ed., Woburn, MA: Butterworth-Heinemann, 2001.

[55] S. Berumen, F. Bechmann, and T. Craeghs, "Quality control system for the coating process in laser-and powder bed-based additive manufacturing technologies," in *Proc. Direct Digital Manufacturing Conference*, Mar. 2012.

[56] S. Kleszczynski, J. Zur Jacobsmühlen, J. Sehrt, and G. Witt, "Error detection in laser beam melting systems by high resolution imaging," in *Proc. 2012 Solid Freeform Fabrication Symposium*, Austin, TX, 2012, pp. 975–987.

[57] J.-P. Kruth, P. Mercelis, J. Van Vaerenbergh, and T. Craeghs, "Feedback control of selective laser melting," in *Proc. 3rd International conference on advanced research in virtual and rapid prototyping*, 2007, pp. 521–527.

[58] J.-P. Kruth, J. Duflou, P. Mercelis, J. Van Vaerenbergh, T. Craeghs, and J. De Keuster, "On-line monitoring and process control in selective laser melting and laser cutting," in *Proc. 5th Laser Assisted Net Shape Engineering Conference*, vol. 1, 2007, pp. 23–37.

[59] P. Lott, H. Schleifenbaum, W. Meiners, K. Wissenbach, C. Hinke, and J. Bültmann, "Design of an optical system for the in situ process monitoring of selective laser melting (SLM)," *Physics Procedia*, vol. 12, pp. 683–690, 2011.

[60] Y. Chivel and I. Smurov, "SLS process monitoring and adaptive control," in *Proc. 4th International WLT-Conference on Lasers in Manufacturing*, Munchen, DE, Jun. 2007, pp. 553–556.

[61] Y. Chivel and I. Smurov, "On-line temperature monitoring in selective laser sintering/melting," *Physics Procedia*, vol. 5, pp. 515–521, 2010.

[62] Y. Chivel and I. Smurov, "Temperature monitoring in selective laser sintering/melting," in *Proc. Fundamentals of Laser Assisted Micro- and Nanotechnologies*, vol. 7996., St. Petersburg, Russian Federation: SPIE, Feb. 2011, p. 79960A.

[63] J. S. Kaizer, A. K. Heller, and W. L. Oberkampf, "Scientific computer simulation review," *Reliability Engineering & System Safety*, vol. 138, pp. 210–218, 2015.

[64] E. Madenci and I. Guven, *The finite element method and applications in engineering using ANSYS®*, 2nd ed., Boston, MA: Springer, 2015.

[65] P. Michaleris, "Modeling metal deposition in heat transfer analyses of additive manufacturing processes," *Finite Elements in Analysis and Design*, vol. 86, pp. 51–60, 2014.

[66] J. Schilp, C. Seidel, H. Krauss, and J. Weirather, "Investigations on temperature fields during laser beam melting by means of process monitoring and multiscale process modelling," *Advances in Mechanical Engineering*, vol. 6, p. 217584, 2014.

[67] D. Pal, N. Patil, K. Zeng, and B. Stucker, "An integrated approach to additive manufacturing simulations using physics based, coupled multiscale process modeling," *Journal of Manufacturing Science and Engineering*, vol. 136, no. 6, p. 061022, 2014.

[68] A. Foroozmehr, M. Badrossamay, E. Foroozmehr, and S. Golabi, "Finite element simulation of selective laser melting process considering optical penetration depth of laser in powder bed," *Materials & Design*, vol. 89, pp. 255–263, 2016.

[69] E. R. Denlinger, J. Irwin, and P. Michaleris, "Thermomechanical modeling of additive manufacturing large parts," *Journal of Manufacturing Science and Engineering*, vol. 136, no. 6, p. 061007, 2014.

[70] S. H. Nikam and N. K. Jain, "Three-dimensional thermal analysis of multi-layer metallic deposition by micro-plasma transferred arc process using finite element simulation," *Journal of Materials Processing Technology*, vol. 249, pp. 264–273, 2017.

[71] S. A. Khairallah and A. Anderson, "Mesoscopic simulation model of selective laser melting of stainless steel powder," *Journal of Materials Processing Technology*, vol. 214, no. 11, pp. 2627–2636, 2014.

[72] S. A. Khairallah, A. T. Anderson, A. Rubenchik, and W. E. King, "Laser powder-bed fusion additive manufacturing: Physics of complex melt flow and formation mechanisms of pores, spatter, and denudation zones," *Acta Materialia*, vol. 108, pp. 36–45, 2016.

[73] C. Panwisawas, C. Qiu, M. J. Anderson, Y. Sovani, R. P. Turner, M. M. Attallah, J. W. Brooks, and H. C. Basoalto, "Mesoscale modelling of selective laser melting: Thermal fluid dynamics and microstructural evolution," *Computational Materials Science*, vol. 126, pp. 479–490, 2017.

[74] M. Markl and C. Korner, "Multi-scale modeling of powder-bed-based additive manufacturing," *Annual Review of Materials Research*, vol. 46, pp. 1–34, 2016.

[75] K.-H. Leitz, P. Singer, A. Plankensteiner, B. Tabernig, H. Kestler, and L. Sigl, "Multi-physical simulation of selective laser melting," *Metal Powder Report*, vol. 72, no. 5, pp. 331–338, 2017.

[76] C. Qiu, C. Panwisawas, M. Ward, H. C. Basoalto, J. W. Brooks, and M. M. Attallah, "On the role of melt flow into the surface structure and porosity development during selective laser melting," *Acta Materialia*, vol. 96, pp. 72–79, 2015.

[77] W. E. King, A. T. Anderson, R. M. Ferencz, N. E. Hodge, C. Kamath, S. A. Khairallah, and A. M. Rubenchik, "Laser powder bed fusion additive manufacturing of metals; physics, computational, and materials challenges," *Applied Physics Reviews*, vol. 2, no. 4, p. 041304, 2015.

[78] L. Thijs, F. Verhaeghe, T. Craeghs, J. Van Humbeeck, and J.-P. Kruth, "A study of the microstructural evolution during selective laser melting of Ti–6Al–4V," *Acta Materialia*, vol. 58, no. 9, pp. 3303–3312, 2010.

[79] K. A. Mumtaz, P. Erasenthiran, and N. Hopkinson, "High density selective laser melting of Waspaloy®," *Journal of Materials Processing Technology*, vol. 195, no. 1, pp. 77–87, 2008.

[80] H. Niu and I. Chang, "Instability of scan tracks of selective laser sintering of high speed steel powder," *Scripta Materialia*, vol. 41, no. 11, pp. 1229–1234, 1999.

[81] J.-P. Kruth, L. Froyen, J. Van Vaerenbergh, P. Mercelis, M. Rombouts, and B. Lauwers, "Selective laser melting of iron-based powder," *Journal of Materials Processing Technology*, vol. 149, no. 1, pp. 616–622, 2004.

[82] M. F. Zaeh and G. Branner, "Investigations on residual stresses and deformations in selective laser melting," *Production Engineering*, vol. 4, no. 1, pp. 35–45, 2010.

[83] M. Mahmoudi, A. Elwany, A. Yadollahi, S. M. Thompson, L. Bian, and N. Shamsaei, "Mechanical properties and microstructural characterization of selective laser melted 17-4 PH stainless steel," *Rapid Prototyping Journal*, vol. 23, no. 2, pp. 280–294, 2017.

[84] A. Bauereiss, T. Scharowsky, and C. Korner, "Defect generation and propagation mechanism during additive manufacturing by selective beam melting," *Journal of Materials Pro-*

cessing Technology, vol. 214, no. 11, pp. 2522–2528, 2014.

[85] M. Averyanova, P. Bertrand, and B. Verquin, "Studying the influence of initial powder characteristics on the properties of final parts manufactured by the selective laser melting technology," *Virtual and Physical Prototyping*, vol. 6, no. 4, pp. 215–223, 2011.

[86] M. Averyanova, E. Cicala, P. Bertrand, and D. Grevey, "Experimental design approach to optimize selective laser melting of martensitic 17-4 PH powder: Part I–single laser tracks and first layer," *Rapid Prototyping Journal*, vol. 18, no. 1, pp. 28–37, 2012.

[87] A. Spierings, G. Levy, and K. Wegener, "Designing material properties locally with additive manufacturing technology SLM," in *Proc. 2012 Solid Freeform Fabrication Symposium*, Austin, TX, 2012, pp. 447–455.

[88] B. Franco, J. Ma, B. Loveall, G. Tapia, K. Karayagiz, J. Liu, A. Elwany, R. Arroyave, and I. Karaman, "A sensory material approach for reducing variability in additively manufactured metal parts," *Scientific Reports*, vol. 7, 2017.

[89] A. M. Aboutaleb, L. Bian, A. Elwany, N. Shamsaei, S. M. Thompson, and G. Tapia, "Accelerated process optimization for laser-based additive manufacturing by leveraging similar prior studies," *IISE Transactions*, vol. 49, no. 1, pp. 31–44, 2017.

[90] J. Ma, B. Franco, G. Tapia, K. Karayagiz, L. Johnson, J. Liu, R. Arroyave, I. Karaman, and A. Elwany, "Spatial control of functional response in 4D-printed active metallic structures," *Scientific Reports*, vol. 7, 2017.

[91] T. J. Sullivan, *Introduction to uncertainty quantification*., Springer, 2015.

[92] M. C. Kennedy and A. O'Hagan, "Bayesian calibration of computer models," *Journal of the Royal Statistical Society: Series B (Statistical Methodology)*, pp. 425–464, 2001.

[93] S. H. Lee and W. Chen, "A comparative study of uncertainty propagation methods for black-

box-type problems," *Structural and Multidisciplinary Optimization*, vol. 37, no. 3, pp. 239–253, 2009.

[94] M. M. Putko, A. C. Taylor, P. A. Newman, and L. L. Green, "Approach for input uncertainty propagation and robust design in CFD using sensitivity derivatives," *Journal of Fluids Engineering*, vol. 124, no. 1, pp. 60–69, 2002.

[95] L. Mathelin, M. Y. Hussaini, T. A. Zang, and F. Bataille, "Uncertainty propagation for a turbulent, compressible nozzle flow using stochastic methods," *AIAA journal*, vol. 42, no. 8, pp. 1669–1676, 2004.

[96] K. Dalbey, A. Patra, E. Pitman, M. Bursik, and M. Sheridan, "Input uncertainty propagation methods and hazard mapping of geophysical mass flows," *Journal of Geophysical Research: Solid Earth*, vol. 113, no. B5, 2008.

[97] J. Lei and W. Schilling, "Parameter uncertainty propagation analysis for urban rainfall runoff modelling," *Water Science and Technology*, vol. 29, no. 1-2, pp. 145–154, 1994.

[98] G. Evensen, "Sequential data assimilation with a nonlinear quasi-geostrophic model using Monte Carlo methods to forecast error statistics," *Journal of Geophysical Research: Oceans*, vol. 99, no. C5, pp. 10 143–10 162, 1994.

[99] G. Anderson, "Error propagation by the Monte Carlo method in geochemical calculations," *Geochimica et Cosmochimica Acta*, vol. 40, no. 12, pp. 1533–1538, 1976.

[100] F. O. Hoffman and J. S. Hammonds, "Propagation of uncertainty in risk assessments: the need to distinguish between uncertainty due to lack of knowledge and uncertainty due to variability," *Risk Analysis*, vol. 14, no. 5, pp. 707–712, 1994.

[101] P. D. Arendt, D. W. Apley, W. Chen, D. Lamb, and D. Gorsich, "Improving identifiability in model calibration using multiple responses," *Journal of Mechanical Design*, vol. 134, no. 10, p. 100909, 2012.

[102] D. Higdon, J. Gattiker, B. Williams, and M. Rightley, "Computer model calibration using high-dimensional output," *Journal of the American Statistical Association*, vol. 103, no. 482, pp. 570–583, 2008.

[103] A. E. Gelfand, P. Diggle, M. Fuentes, and P. Guttorp, *Handbook of Spatial Statistics*, 1st ed., Boca Raton, FL: CRC Press, 2010.

[104] M. M. Fischer and A. Getis, Eds., *Handbook of applied spatial analysis: software tools, methods and applications*, 1st ed., Berlin: Springer, 2010.

[105] S. Banerjee, B. P. Carlin, and A. E. Gelfand, *Hierarchical modeling and analysis for spatial data*, 2nd ed., Boca Raton, FL: CRC Press, 2014.

[106] J. Oakley and A. O'hagan, "Bayesian inference for the uncertainty distribution of computer model outputs," *Biometrika*, vol. 89, no. 4, pp. 769–784, 2002.

[107] E. B. Sudderth and M. I. Jordan, "Shared segmentation of natural scenes using dependent Pitman-Yor processes," in *Proc. Advances in Neural Information Processing Systems*, 2008, pp. 1585–1592.

[108] C. E. Rasmussen and C. K. I. Williams, *Gaussian Processes for Machine Learning*., Cambridge, MA: The MIT Press, 2006.

[109] S.-C. Hsu and C.-F. Chien, "Hybrid data mining approach for pattern extraction from wafer bin map to improve yield in semiconductor manufacturing," *International Journal of Production Economics*, vol. 107, no. 1, pp. 88–103, 2007.

[110] S. Pegel, P. Pötschke, T. Villmow, D. Stoyan, and G. Heinrich, "Spatial statistics of carbon nanotube polymer composites," *Polymer*, vol. 50, no. 9, pp. 2123–2132, 2009.

[111] T.-H. Yang and J. Jackman, "Form error estimation using spatial statistics," *Journal of Manufacturing Science and Engineering*, vol. 122, no. 1, pp. 262–272, 1999.

[112] G. Cai and S. Mahadevan, "Uncertainty quantification in ICMSE: Application to metal alloys," in *Proc. 56th AIAA/ASCE/AHS/ASC Structures, Structural Dynamics, and Materials Conference*, Kissimmee, FL, Jan. 2015.

[113] G. Blatman and B. Sudret, "An adaptive algorithm to build up sparse polynomial chaos expansions for stochastic finite element analysis," *Probabilistic Engineering Mechanics*, vol. 25, no. 2, pp. 183–197, 2010.

[114] N. Wiener, "The homogeneous chaos," *American Journal of Mathematics*, vol. 60, no. 4, pp. 897–936, 1938.

[115] D. Xiu and G. E. Karniadakis, "The Wiener–Askey polynomial chaos for stochastic differential equations," *SIAM Journal on Scientific Computing*, vol. 24, no. 2, pp. 619–644, 2002.

[116] A. Prabhakar, J. Fisher, and R. Bhattacharya, "Polynomial chaos-based analysis of probabilistic uncertainty in hypersonic flight dynamics," *Journal of Guidance, Control, and Dynamics*, vol. 33, no. 1, p. 222, 2010.

[117] G. Sansone, *Orthogonal functions*., Courier Corporation, 1959.

[118] A. O'Hagan, "Polynomial chaos: A tutorial and critique from a statistician's perspective," University of Sheffield, Tech. Rep., 2013. [Online]. Available: http://tonyohagan.co.uk/academic/pdf/Polynomial-chaos.pdf

[119] H. Zou and T. Hastie, "Regularization and variable selection via the elastic net," *Journal of the Royal Statistical Society: Series B (Statistical Methodology)*, vol. 67, no. 2, pp. 301–320, 2005.

[120] J. Friedman, T. Hastie, and R. Tibshirani, "Regularization paths for generalized linear models via coordinate descent," *Journal of Statistical Software*, vol. 33, no. 1, p. 1, 2010.

[121] T. Hastie and J. Qian, *Glmnet Vignette*, Sep., last accessed: April 16, 2018. [Online]. Available: http://www.web.stanford.edu/~hastie/Papers/Glmnet_Vignette.pdf

[122] J. Friedman, T. Hastie, and R. Tibshirani, "A note on the group lasso and a sparse group lasso," *ArXiv e-prints*, no. 1001.0736, Jan. 2010.

[123] A. B. Owen, "Variance components and generalized sobol'indices," *SIAM/ASA Journal on Uncertainty Quantification*, vol. 1, no. 1, pp. 19–41, 2013.

[124] B. Sudret, "Global sensitivity analysis using polynomial chaos expansions," *Reliability Engineering & System Safety*, vol. 93, no. 7, pp. 964–979, 2008.

[125] C. Kamath, "Data mining and statistical inference in selective laser melting," *The International Journal of Advanced Manufacturing Technology*, pp. 1–19, 2016.

[126] N. A. C. Cressie, *Statistics for Spatial Data*, revised ed., New York, NY: John Wiley & Sons, 1993.

[127] B. Peterson, *Understanding exposure: how to shoot great photographs with any camera.*, AmPhoto books, 2016.

[128] T. Eagar and N. Tsai, "Temperature fields produced by traveling distributed heat sources," *Welding Journal*, vol. 62, no. 12, pp. 346–355, 1983.

[129] W. E. King, A. T. Anderson, R. M. Ferencz, N. E. Hodge, C. Kamath, and S. A. Khairallah, "Overview of modelling and simulation of metal powder bed fusion process at Lawrence Livermore National Laboratory," *Materials Science and Technology*, vol. 31, no. 8, pp. 957–968, 2015.

[130] C. Kamath, B. El-dasher, G. F. Gallegos, W. E. King, and A. Sisto, "Density of additively-manufactured, 316L SS parts using laser powder-bed fusion at powers up to 400 W," *The International Journal of Advanced Manufacturing Technology*, vol. 74, no. 1-4, pp. 65–78, 2014.

[131] J. Ion, "Laser transformation hardening," *Surface Engineering*, vol. 18, no. 1, pp. 14–31, 2002.

[132] E. A. Bonifaz, "Finite element analysis of heat flow in single-pass arc welds," *Welding Journal*, vol. 79, no. 5, pp. 121–125, 2000.

[133] ASM Aerospace Specification Metals Inc. AISI type 430 stainless steel annealed sheet. Last accessed: April 16, 2018. [Online]. Available: http://asm.matweb.com/search/SpecificMaterial.asp?bassnum=mq430an

[134] P. Bratley and B. L. Fox, "Algorithm 659: Implementing sobol's quasirandom sequence generator," *ACM Transactions on Mathematical Software (TOMS)*, vol. 14, no. 1, pp. 88–100, 1988.

[135] W. Chen, L. Baghdasaryan, T. Buranathiti, and J. Cao, "Model validation via uncertainty propagation and data transformations," *AIAA Journal*, vol. 42, no. 7, pp. 1406–1415, 2004.

[136] R. G. Hills and T. G. Trucano, "Statistical validation of engineering and scientific models: Background," Sandia National Laboratories, Albuquerque, NM, Tech. Rep. SAND99-1256, May 1999.

[137] R. Andreotta, L. Ladani, and W. Brindley, "Finite element simulation of laser additive melting and solidification of Inconel 718 with experimentally tested thermal properties," *Finite Elements in Analysis and Design*, vol. 135, pp. 36–43, 2017.

[138] A. Masmoudi, R. Bolot, and C. Coddet, "Investigation of the laser–powder–atmosphere interaction zone during the selective laser melting process," *Journal of Materials Processing Technology*, vol. 225, pp. 122–132, 2015.

[139] J. Romano, L. Ladani, and M. Sadowski, "Laser additive melting and solidification of Inconel 718: Finite element simulation and experiment," *The Journal of The Minerals, Metals & Materials Society*, vol. 68, no. 3, pp. 967–977, 2016.

[140] G. Tapia, L. Johnson, B. Franco, K. Karayagiz, J. Ma, R. Arroyave, I. Karaman, and A. Elwany, "Bayesian calibration and uncertainty quantification for a physics-based precipitation model of nickel–titanium shape-memory alloys," *Journal of Manufacturing Science and Engineering*, vol. 139, no. 7, p. 071002, 2017.

[141] *Standard Test Methods for Density of Compacted or Sintered Powder Metallurgy (PM) Products Using Archimedes' Principle*, ASTM Std. B962, Rev. 17, 2017. [Online]. Available: https://www.astm.org/Standards/B962.htm

[142] The Minerals Metals & Materials Society (TMS), *Modeling Across Scales: A Roadmapping Study for Connecting Materials Models and Simulations Across Length and Time Scales*., Warrendale, PA: TMS, 2015. [Online]. Available: www.tms.org/multiscalestudy

[143] D. Higdon, M. Kennedy, J. C. Cavendish, J. A. Cafeo, and R. D. Ryne, "Combining field data and computer simulations for calibration and prediction," *SIAM Journal on Scientific Computing*, vol. 26, no. 2, pp. 448–466, 2004.

[144] M. C. Kennedy and A. O'Hagan, "Supplementary details on bayesian calibration of computer models," University of Sheffield, Tech. Rep., 2001. [Online]. Available: https://www2.stat.duke.edu/courses/Spring14/sta961.01/ref/KennOHag2000b.pdf

[145] G. B. Olson, "Computational design of hierarchically structured materials," *Science*, vol. 277, no. 5330, pp. 1237–1242, 1997.

[146] C. Kuehmann and G. Olson, "Computational materials design and engineering," *Materials Science and Technology*, vol. 25, no. 4, pp. 472–478, 2009.

[147] L. Johnson and R. Arróyave, "An inverse design framework for prescribing precipitation heat treatments from a target microstructure," *Materials & Design*, vol. 107, pp. 7–17, 2016.

[148] J. Kim, Y. Liu, and S. Miyazaki, "Ageing-induced two-stage R-phase transformation in Ti–50.9 at.% Ni," *Acta Materialia*, vol. 52, no. 2, pp. 487–499, 2004.

[149] E. Y. Panchenko, Y. I. Chumlyakov, I. Kireeva, A. Ovsyannikov, H. Sehitoglu, I. Karaman, and Y. Maier, "Effect of disperse Ti3N4 particles on the martensitic transformations in titanium nickelide single crystals," *The Physics of Metals and Metallography*, vol. 106, no. 6, pp. 577–589, 2008.

[150] Y. Zheng, F. Jiang, L. Li, H. Yang, and Y. Liu, "Effect of ageing treatment on the transformation behaviour of Ti–50.9 at.% Ni alloy," *Acta Materialia*, vol. 56, no. 4, pp. 736–745, 2008.

[151] J. Frenzel, E. P. George, A. Dlouhy, C. Somsen, M.-X. Wagner, and G. Eggeler, "Influence of Ni on martensitic phase transformations in NiTi shape memory alloys," *Acta Materialia*, vol. 58, no. 9, pp. 3444–3458, 2010.

[152] S. Conti and A. O'Hagan, "Bayesian emulation of complex multi-output and dynamic computer models," *Journal of Statistical Planning and Inference*, vol. 140, no. 3, pp. 640–651, 2010.

[153] K. S. Bhat, M. Haran, M. Goes, and M. Chen, "Computer model calibration with multivariate spatial output: A case study," *Frontiers of Statistical Decision Making and Bayesian Analysis*, pp. 168–184, 2010.

[154] G. Casella and R. L. Berger, *Statistical inference*, 2nd ed., Pacific Grove, CA: Duxbury, 2002.

[155] B. Cheng, S. Price, J. Lydon, K. Cooper, and K. Chou, "On process temperature in powder-bed electron beam additive manufacturing: model development and validation," *Journal of Manufacturing Science and Engineering*, vol. 136, no. 6, p. 061018, 2014.

[156] C. Boley, S. Khairallah, and A. Rubenchik, "Calculation of laser absorption by metal powders in additive manufacturing," *Applied Optics*, vol. 54, no. 9, pp. 2477–2482, 2015.

[157] A. Rubenchik, S. Wu, S. Mitchell, I. Golosker, M. LeBlanc, and N. Peterson, "Direct mea-

surements of temperature-dependent laser absorptivity of metal powders," *Applied Optics*, vol. 54, no. 24, pp. 7230–7233, 2015.

[158] M. Grasso and B. M. Colosimo, "Process defects and in situ monitoring methods in metal powder bed fusion: a review," *Measurement Science and Technology*, vol. 28, no. 4, p. 044005, 2017.

[159] P. D. Hoff, *A first course in Bayesian statistical methods*, 1st ed., New York, NY: Springer, 2009.

[160] G. Fishman, *Monte Carlo: concepts, algorithms, and applications*, 1st ed., New York, NY: Springer, 1996.

[161] C. Andrieu, N. De Freitas, A. Doucet, and M. I. Jordan, "An introduction to MCMC for machine learning," *Machine Learning*, vol. 50, no. 1, pp. 5–43, 2003.

APPENDIX A

STATISTICAL CONCEPTS

A.1 Probability Distributions Functions

This section presents the probability distributions of different random variables that were employed along this work to avoid subjectivities due to re-parameterizations frequently used by other authors.

- Continuous Uniform distribution
  - Notation: $\mathrm{U}(a, b)$, where *a* is the lower bound and *b* is the upper bound.
  - Formula:

$$p(x) = \begin{cases} \frac{1}{b-a} & \text{for } x \in [a, b] \\ 0 & \text{otherwise} \end{cases} \tag{A.1}$$

    where $x \in [a, b]$, $a \in \mathbb{R}$, $b \in \mathbb{R}$, $a < b$.

- Univariate Normal distribution
  - Notation: $\mathrm{N}(\mu, \sigma^2)$, where μ is the mean and σ^2 is the variance.
  - Formula:

$$p(x) = \frac{1}{\sqrt{2\pi\sigma^2}} \exp\left[-\frac{1}{2\sigma^2}(x-\mu)^2\right] \tag{A.2}$$

    where $x \in \mathbb{R}$, $\mu \in \mathbb{R}$, $\sigma^2 > 0$.

- Multivariate Normal distribution
  - Notation: $\mathrm{N}_q(\boldsymbol{\mu}, \boldsymbol{\Sigma})$, where $\boldsymbol{\mu}$ is the mean vector, $\boldsymbol{\Sigma}$ is the covariance matrix and *q* is the dimensionality of the distribution.
  - Formula:

$$p(\mathbf{x}) = |2\pi\boldsymbol{\Sigma}|^{-\frac{1}{2}} \exp\left[-\frac{1}{2}(\mathbf{x}-\boldsymbol{\mu})^\top \boldsymbol{\Sigma}^{-1}(\mathbf{x}-\boldsymbol{\mu})\right] \tag{A.3}$$

where $\mathbf{x} \in \mathbb{R}^q$, $\boldsymbol{\mu} \in \mathbb{R}^q$, $\boldsymbol{\Sigma} \in \mathbb{R}_+^{q,q}$.

- Gamma distribution
  - Notation: $\mathrm{Gamma}\,(\alpha, \beta)$, where α is the shape parameter and β is the rate parameter.
  - Formula:

$$p\,(x) = \frac{\beta^{\alpha}}{\Gamma\,(\alpha)} x^{\alpha-1} \exp\,(-\beta x) \tag{A.4}$$

    where $x \in (0, \infty)$, $\alpha > 0$, $\beta > 0$.

- Inverse Gamma distribution
  - Notation: $\mathrm{IG}\,(\alpha, \beta)$, where α is the shape parameter and β is the scale parameter.
  - Formula:

$$p\,(x) = \frac{\beta^{\alpha}}{\Gamma\,(\alpha)} x^{-\alpha-1} \exp\left(-\frac{\beta}{x}\right) \tag{A.5}$$

    where $x \in (0, \infty)$, $\alpha > 0$, $\beta > 0$.

- Beta distribution
  - Notation: $\mathrm{Beta}\,(\alpha, \beta)$, where α and β are shape parameters.
  - Formula:

$$p\,(x) = \frac{\Gamma\,(\alpha+\beta)}{\Gamma\,(\alpha)\,\Gamma\,(\beta)} x^{\alpha-1}\,(1-x)^{\beta-1} \tag{A.6}$$

    where $x \in [0, 1]$, $\alpha > 0$, $\beta > 0$.

- Log Logistic distribution
  - Notation: $\mathrm{Log\,Logistic}\,(\alpha, \beta)$, where α is the scale parameter and β is the shape parameter.
  - Formula:

$$p\,(x) = \frac{\left(\frac{\beta}{\alpha}\right)\left(\frac{x}{\alpha}\right)^{\beta-1}}{\left(1+\left(\frac{x}{\alpha}\right)^{\beta}\right)^2} \tag{A.7}$$

    where $x \in [0, \infty)$, $\alpha > 0$, $\beta > 0$.

A.2 Bayesian Statistics

The present dissertation relies heavily in a variety of frameworks and tools developed in academic disciplines like math, statistics, machine learning and data science/analytics. One of the key fields employed throughout this dissertation is based on Bayesian methods, since these are tools that provide the following [159]:

- Parameter estimates with good statistical properties
- Parsimonious descriptions of observed data
- Predictions for missing data and forecasts of future data
- Computational framework for model estimation, selection and validation

Bayesian inference is set around *Bayes' rule*,

$$\begin{aligned} p\left(A|B\right) &= \frac{p\left(A,B\right)}{p\left(B\right)} \\ &= \frac{p\left(B|A\right)p\left(A\right)}{\int_{\mathcal{A}} p\left(B|A\right)p\left(A\right)dA} \\ &\propto p\left(B|A\right)p\left(A\right) \end{aligned} \tag{A.8}$$

which measures the degree of belief of event *A* before and after accounting for evidence from event *B*.

Under these settings, $p\left(A\right)$, called the *prior*, is the initial belief or knowledge of event *A* prior to any new evidence or observations. Next, $p\left(B|A\right)$ is the *likelihood* function which represents the probability of observing event *B* given that *A* is true. Finally, the *posterior* probability $p\left(A|B\right)$ is the degree of belief of event *A* after having accounted for evidence from *B*.

In our general problem context, we are interested on estimation or inference of general characteristics of a population (*parameters*) based on a subset of members of that population (parameters inferred from *data*) [159]. In this case, domain $\mathcal{Y}$ is the set of all possible datasets, from which

a single dataset $\mathbb{Y}$ will result, and the parameter space $\boldsymbol{\Theta}$ is the set of possible parameter values, from which we want to identify the value $\boldsymbol{\theta}$ that best represents the population [159].

Therefore, based on Equation (A.8), we want to update our beliefs about parameter $\boldsymbol{\theta}$ after having observed dataset $\mathbb{Y}$ in addition with some prior knowledge about them. Then, the posterior distribution is

$$\begin{aligned} p\left(\boldsymbol{\theta}|\mathbb{Y}\right) &= \frac{p\left(\mathbb{Y}|\boldsymbol{\theta}\right) p\left(\boldsymbol{\theta}\right)}{\int_{\boldsymbol{\Theta}} p\left(\mathbb{Y}\middle|\tilde{\boldsymbol{\theta}}\right) p\left(\tilde{\boldsymbol{\theta}}\right) d\tilde{\boldsymbol{\theta}}} \\ &\propto p\left(\mathbb{Y}|\boldsymbol{\theta}\right) p\left(\boldsymbol{\theta}\right) \end{aligned}$$

which can be calculated in closed form if the integral in the denominator can be evaluated, or numerically using MCMC algorithms (see Appendix B).

A.3 Cross Validation Procedures

Performance and predictive capabilities of a statistical (or machine learning) model may be numerically assessed by different metrics along with a *Cross Validation* (CV) procedure. In this procedure, datapoints used to estimate the parameters of the statistical model are denoted as *training* dataset. A frequent approach is to keep out of training a portion of the observed dataset, denote this portion as *test* dataset, and use it to test the prediction accuracy of the statistical model by comparing its predictions to the actual observed values.

The most common technique for cross validation is called *k-fold* cross validation, which is an iterative procedure whereby the entire dataset is randomly partitioned into k disjoint subsets of approximately the same size. The statistical model is then trained with all but one subset, which is kept out as the test dataset. This process is then repeated until all k subsets have been left out once, and then the resulting prediction errors are evaluated. A special case is when $k = n$, called *Leave-One-Out* (LOO) CV, where the model is trained with all but one data point at each iteration.

Two metrics are popular measures of performance among the statistics/data analytics fields: *mean squared predictive error* (MSPE) and *mean absolute predictive error* (MAPE):

$$\mathrm{MSPE} = \frac{1}{n}\sum_{i=1}^{n}\left(Y_i^{(\mathrm{obs})} - Y_i^{(\mathrm{pred})}\right)^2 \tag{A.9}$$

$$\mathrm{MAPE} = \frac{1}{n}\sum_{i=1}^{n}\left|Y_i^{(\mathrm{obs})} - Y_i^{(\mathrm{pred})}\right| \tag{A.10}$$

where $Y_i^{(\mathrm{obs})}$ is the *i*th observation and $Y_i^{(\mathrm{pred})}$ is the corresponding *i*th prediction from the model at the same set of inputs $\mathbf{x}_i$, and since they are usually applied along with CV, this calculations are done when the *i*th datapoint was not included within the training set.

This approach is taken in order to fine tune hyperparameters or other design components that are included within the statistical model formulation, in order to arrive a those settings that make the statistical model perform the best in presence of the observed data.

If the problem setting is multivariate ($\mathbf{Y} \in \mathcal{Y} \subseteq \mathbb{R}^d$ with $d > 1$), validation metrics from Equations (A.9) and (A.10) have to be generalized to account all different outputs. Two solutions can be expanded from these equations, which will be presented for MAPE but can be translated as well to MSPE:

- *Single mean absolute predictive error* (MAPE_k) that measures the average prediction error for each QoI,

$$\mathrm{MAPE}_k = \frac{1}{n}\sum_{i=1}^{n}\left|Y_{i,k}^{(\mathrm{obs})} - Y_{i,k}^{(\mathrm{pred})}\right| \quad \forall k \in \{1,\ldots,d\} \tag{A.11}$$

  where $Y_{i,k}$ is the *k*th QoI from the *i*th observation.

- *Aggregated mean absolute predictive error* ($\mathrm{MAPE}_{\mathcal{L}_1}$) that measures the average prediction error among all QoIs,

$$\mathrm{MAPE}_{\mathcal{L}_1} = \frac{1}{n}\sum_{i=1}^{n}\left\|\mathbf{Y}_i^{(\mathrm{obs})} - \mathbf{Y}_i^{(\mathrm{pred})}\right\|_{\mathcal{L}_1} \tag{A.12}$$

  where the $\mathcal{L}_1$-norm for some *d*-dimensional vector $\mathbf{Y}$ is defined as $\sum_{k=1}^{d}|Y_k|$.

It has to be noted that when using $\mathrm{MAPE}_{\mathcal{L}_1}$, the observation vectors $\mathbf{Y}$ should be standardized to

mean 0 and variance 1 in order to have all QoIs at the same numeric scale such that aggregations between QoIs are relevant.

APPENDIX B

MARKOV CHAIN MONTE CARLO ALGORITHMS

Monte Carlo methods are a broad class of computational algorithms that rely on repeated random sampling to provide approximate solutions to a variety of problems (physical or mathematical with or without any probabilistic structure) [160]. Several different algorithms have been developed to solve different problems, however in this dissertation we will only focus on those that are needed for general numerical estimation and Bayesian statistical inference.

B.1 Monte Carlo Principle

The *Monte Carlo* (MC) principle is one of the most popular methods to numerically approximate probability distributions as well as integrals. The idea is based on the random drawing of N independent and identically distributed (i.i.d.) samples from a target distribution $p(\mathbf{x})$ defined on a q-dimensional space $\mathcal{X} \in \mathbb{R}^q$. The empirical distribution of $\left\{\mathbf{x}^{(1)}, \ldots, \mathbf{x}^{(N)}\right\}$ is known as a Monte Carlo approximation to $p(\mathbf{x})$, with

$$p_{\mathrm{MC}}(\mathbf{x}) = \frac{1}{N} \sum_{i=1}^{N} 1_{\left\{\mathbf{x}=\mathbf{x}^{(i)}\right\}}\left(\mathbf{x}^{(i)}\right) \tag{B.1}$$

where $1_{\left\{\mathbf{x}=\mathbf{x}^{(i)}\right\}}\left(\mathbf{x}^{(i)}\right)$ is the indicator function that equals to 1 if $\mathbf{x} = \mathbf{x}^{(i)}$ and 0 otherwise [159, 161].

Additionally, MC can be used to approximate expectations (or integrals) with N i.i.d. random samples, since the Law of Large Numbers describe that for (almost) any function $g(\mathbf{x})$, we have that

$$\frac{1}{N} \sum_{i=1}^{N} g\left(\mathbf{x}^{(i)}\right) \overset{N\to\infty}{\longrightarrow} \mathbb{E}\left[g(\mathbf{x})\right] \overset{N\to\infty}{\longrightarrow} \int_{\mathcal{X}} g(\mathbf{x})\, p(\mathbf{x})\, d\mathbf{x}$$

Algorithm B.1 Gibbs Sampler

$N \leftarrow$ number MCMC iterations
$B \leftarrow$ Burn-in period
$T \leftarrow$ Thinning
Start with arbitrary point $\mathbf{x}^{(0)} = \left\{x_1^{(0)}, \ldots, x_q^{(0)}\right\}$
for $i \leftarrow 1$ **to** *N* **do** ▷Number of MCMC iterations
  for all $x^{(i)} \in \mathbf{x}^{(i)}$ **do** ▷Iterate over elements of vector **x**
    Draw

$$x_j^{(i)} \sim p\left(x_j \middle| x_1^{(i)}, x_2^{(i)}, \ldots, x_{j-1}^{(i)}, x_{j+1}^{(i-1)}, \ldots, x_{q-1}^{(i-1)}, x_q^{(i-1)}\right)$$

  end for
  Concatenate sample $\mathbf{x}^{(i)} \leftarrow \left\{x_1^{(i)}, \ldots, x_q^{(i)}\right\}$
end for
return $\left\{\mathbf{x}^{(1)}, \ldots, \mathbf{x}^{(N)}\right\}$
Do inference of $p(\mathbf{x})$ with empirical distribution $\left\{\mathbf{x}^{(B)}, \mathbf{x}^{(B+T)}, \mathbf{x}^{(B+2T)}, \ldots, \mathbf{x}^{(N-T)}, \mathbf{x}^{(N)}\right\}$

since $\mathbb{E}[g(\mathbf{x})] = \int_{\mathcal{X}} g(\mathbf{x})\, p(\mathbf{x})\, d\mathbf{x}$, with $p(\mathbf{x})$ known or estimated from Equation (B.1) [159, 161].

B.2 Gibbs Sampler

In this widely used algorithm, the objective is to approximate multivariate probability distributions from which only the full conditional distributions for each element are known. In other words, for a random vector $\mathbf{x} = \{x_1, \ldots, x_q\}$, the interest is to approximate its joint probability distribution, $p(\mathbf{x}) = p(x_1, \ldots, x_q)$, with only knowledge and ability to sample from full conditional distributions of the form $p(x_k | x_1, \ldots, x_{k-1}, x_{k+1}, \ldots, x_q)\ \forall k \in \{1, \ldots, q\}$ [159].

The pseudo-code is presented in Algorithm B.1 for a sequence of *N* iterations, and it is shown that for the *i*th sample within the sequence, $\mathbf{x}^{(i)}$ depends on $\left\{\mathbf{x}^{(0)}, \ldots, \mathbf{x}^{(i-1)}\right\}$ only through $\mathbf{x}^{(i-1)}$. This relationship is called *Markov property* and that is the reason why these sequences (and hence the algorithms) are called *Markov Chain*s MC (MCMC) [159].

B.3 Metropolis-Hastings Algorithm

The *Metropolis-Hastings* (MH) algorithm is the most popular MCMC method [161]. The objective of this algorithm is to approximate a joint probability distribution $p(\mathbf{x}) = p(x_1, \ldots, x_q)$ by indirect random samples when direct sampling is not feasible (which is usually the case for

Bayesian posterior distributions). The main idea is to propose samples from a another distribution and then accept or reject them one element at a time.

Consequently, a proposal distribution needs to be defined for every component of the random vector **x**. These proposal distributions can be symmetric distributions, full conditional distributions, or something else entirely. The interested reader can refer to [159, 161] for more detailed explanations about this algorithm and the requirements that proposal distributions need to follow in order to ensure sequence with Markov Chain properties.

Here, the proposal distribution for the *j*th element of vector **x** and at the *i*th MH iteration is denoted as $J_j\left(x_j \middle| x_1^{(i)}, \ldots, x_{j-1}^{(i)}, x_j^{(i-1)}, x_{j+1}^{(i-1)}, \ldots, x_q^{(i-1)}\right)$. The pseudo-code is presented in Algorithm B.2.

Algorithm B.2 Metropolis-Hastings Algorithm

$N \leftarrow$ number MCMC iterations
$B \leftarrow$ Burn-in period
$T \leftarrow$ Thinning
Start with arbitrary point $\mathbf{x}^{(0)} = \left\{x_1^{(0)}, \ldots, x_q^{(0)}\right\}$
for $i \leftarrow 1$ **to** N **do** ▷Number of MCMC iterations
  for all $x^{(i)} \in \mathbf{x}^{(i)}$ **do** ▷Iterate over elements of vector $\mathbf{x}$
    Draw

$$x_j^{\star} \sim J_j\left(x_j \middle| x_1^{(i)}, \ldots, x_{j-1}^{(i)}, x_j^{(i-1)}, x_{j+1}^{(i-1)}, \ldots, x_q^{(i-1)}\right)$$

    Compute the acceptance ratio

$$r = \frac{p\left(x_1^{(i)}, \ldots, x_{j-1}^{(i)}, x_j^{\star}, x_{j+1}^{(i-1)}, \ldots, x_q^{(i-1)}\right)}{p\left(x_1^{(i)}, \ldots, x_{j-1}^{(i)}, x_j^{(i-1)}, x_{j+1}^{(i-1)}, \ldots, x_q^{(i-1)}\right)} \times \frac{J_j\left(x_j^{(i-1)} \middle| x_1^{(i)}, \ldots, x_{j-1}^{(i)}, x_j^{\star}, x_{j+1}^{(i-1)}, \ldots, x_q^{(i-1)}\right)}{J_j\left(x_j^{\star} \middle| x_1^{(i)}, \ldots, x_{j-1}^{(i)}, x_j^{(i-1)}, x_{j+1}^{(i-1)}, \ldots, x_q^{(i-1)}\right)}$$

    Draw $u \sim \text{Uniform}\,(0, 1)$
    if $u < r$ **then**
      $x_j^{(i)} \leftarrow x_j^{\star}$
    else
      $x_j^{(i)} \leftarrow x_j^{(i-1)}$
    end if
  end for
  Concatenate sample $\mathbf{x}^{(i)} \leftarrow \left\{x_1^{(i)}, \ldots, x_q^{(i)}\right\}$
end for
return $\left\{\mathbf{x}^{(1)}, \ldots, \mathbf{x}^{(N)}\right\}$
Do inference of $p\,(\mathbf{x})$ with empirical distribution $\left\{\mathbf{x}^{(B)}, \mathbf{x}^{(B+T)}, \mathbf{x}^{(B+2T)}, \ldots, \mathbf{x}^{(N-T)}, \mathbf{x}^{(N)}\right\}$